Nanoscale Fluid Transport: From Molecular Signatures to Applications

Tuan Anh Ho

A dissertation submitted in partial fulfillment of the requirements for the degree of

Doctor of Philosophy

of the

University College London

Department of Chemical Engineering

UCL

Primary Advisor: Prof. Alberto Striolo

March 2015

1

Declaration

I, Tuan Anh Ho confirm that the work presented in this thesis is my own. Where information has been derived from other sources, I confirm that this has been indicated in the thesis.

Abstract

Motivated by the fact that many novel fluid transport phenomena have been discovered at nano length scales, in this thesis I use molecular dynamics simulations to investigate how a solid surface affects the fluid properties and fluid transport in nanochannels. My ultimate goal is to search for the molecular signatures of the macroscopic observations. From the understanding of the mutual relation between molecular properties and macroscopic observations, I learn how to tailor the fluid-solid interaction to improve the performance of practical applications including nano-fluidic devices, water desalination, energy storage, and shale gas exploration. For example, in Chapter 3 I find out that liquid water can slip on hydrophilic surfaces, which contradicts conventional knowledge. The responsible molecular signature appears to be the dynamical properties of interfacial water molecules, governed by the strength of water-surface interactions and surface morphology. When water molecules can migrate from one preferential adsorption site to the next without requiring hopping events, hydrodynamic liquid slip occurs. In Chapter 4 I illustrate that the structural and dynamical properties of the electric double layer formed near graphene electrodes are crucial to the performance of supercapacitors and capacitive desalination devices. By tailoring the electrode, thin and mobile electric double layer can be obtained that can tremendously enhance the capacitance of supercapacitors and the manner that capacitive desalination devices is operated. Finally, in the study of two-phase (water and methane) flow through muscovite nanopore reported in Chapter 5 I demonstrate that the flow pattern change not only affects the movement of methane with respect to that of water but also affects the pore structure, in particular its width. As muscovite has similar structure to illite, a clay often found in shale rocks, these results advance my understanding regarding the mechanism of water and gas transport in tight shale gas formations.

Contents

Acknowledgements

I would like to express my deepest gratitude to my advisor Professor Alberto Striolo for his guidance, encouragement, motivation, and support throughout my PhD study. I appreciate his time and efforts spending to help me improve my personal skills and build my career. I enjoy my time working in his fantastic group and I am very proud of what we have achieved together.

I would like to thank Professor Haroun Mahgerefteh for serving as my secondary advisor. Special thanks to Professor Dimitrios Papavassiliou for the collaborations and advice during early years of my PhD study. I am also grateful to my undergraduate advisor, Dr. L. H. Nguyen for encouraging me to enter postgraduate school and for all the interesting discussions we had every time I visit. Thank you my officemates, colleagues, and friends for all the fun and joy we shared during my PhD study.

This thesis is dedicated to my wonderful parents and my lovely sisters, who always believe and encourage me. Words cannot express my gratitude for everything they have done to make me into who I am. I hope I have made them proud. This thesis is also dedicated to my other half Ngoc Nguyen. I am thankful to my wife for love and care and for sharing with me every moment of this incredible journey. I am looking forward to our new one. Finally thank you my unborn baby Tony for encouraging me to leave doctoral school for a new job. I cannot wait to have him in this world.

<div align="right">

Tuan A. Ho
University College London
February 2015

</div>

Publications during PhD study

Google Scholar page: http://scholar.google.com/citations?user=SkMturMAAAAJ&hl=en

1. T.A. Ho and A. Striolo**,** *Water and Methane in Shale Rocks: Flow Pattern Effects on Fluid Transport and Pore Structure.* **(2015).** Submitted.

2. T.A. Ho and A. Striolo, *Promising Performance Indicators for Water Desalination and Aqueous Capacitors Obtained by Engineering the Electric Double Layer in Nano-Structured Carbon Electrodes*, **J. Phys. Chem. C** 119 **(2015)** 3331-3337.

3. T.A. Ho and A. Striolo**,** *Molecular Dynamics Simulation of Graphene-Water Interface: Comparing Water Models***, Molecular Simulation** 40 **(2014)** 1190-1200.

4. T.A. Ho and A. Striolo, *Capacitive enhancement via electrode patterning*, **J. Chem. Phys.** 139 **(2013)** 204708.

5. D. Konatham, J. Yu, T.A. Ho, and A. Striolo, *Simulation insights for graphene-based water desalination membranes,* **Langmuir** 29 **(2013)** 11884-11897. **This article was featured in the journal cover.**

6. R.K. Kalluri, T.A. Ho, J. Biener, M.M. Biener, and A. Striolo, *Partition and Structure of Aqueous NaCl and CaCl$_2$ Electrolytes in Carbon-Slit Electrodes***, J. Phys. Chem. C** 117 **(2013)** 13609-13619**.**

7. T.A. Ho and A. Striolo, Polarizability Effects in Molecular Dynamics Simulations of the Graphene-Water Interface, **J. Chem. Phys.** 138 **(2013)** 054117.

8. A. Phan, T.A. Ho, D.R. Cole, and A. Striolo, *Molecular Structure and Dynamics in Thin Water Films at Metal Oxide Surfaces: Magnesium, Aluminum, and Silicon*

Oxide Surfaces, **J. Phys. Chem. C** 116 **(2012)** 15962-15973. **This article was featured in the journal cover.**

9. T.A. Ho, D. Argyris, D.R. Cole, and A. Striolo, Aqueous NaCl and CsCl Solutions Confined in Crystalline Slit-Shaped Silica Nanopores of Varying Degree of Hydroxylation, **Langmuir** 28 **(2012)** 1256–1266.

10. T.A. Ho, D.V. Papavassiliou, L.L. Lee, A. Striolo, *Water Can Slip on a Hydrophilic Surface*, **Proceedings of the National Academy of Sciences of the United States of America** 108 (**2011**) 16170-16175.

11. T.A. Ho, D. Argyris, D.V. Papavassiliou, A. Striolo, L.L. Lee, and D.R. Cole, *Interfacial Water on Crystalline Silica: A Comparative Molecular Dynamics Simulation Study*, **Molecular Simulation** 37 (**2011**) 172-195.

12. D. Argyris, T.A. Ho, D.R. Cole, and A. Striolo, *Molecular Dynamics Studies of Interfacial Water at the Alumina Surface*, **J. Phys. Chem. C** 115 (**2011**) 2038-2046.

Conference presentations during PhD study

1. T.A. Ho and A. Striolo, Aqueous Electrolyte Solutions Near Carbon Surfaces: How Atomistic Simulation Studies Led to the Design of a Continuous Desalination Cell with High Performance Predicted for Brackish Water, **AIChE Annual Meeting**, Atlanta, GA, November 16th-21th, **2014**.

2. T.A. Ho and A. Striolo, The Role of Mobile and Thin Helmholtz Electric Double Layer in Energy Storage and Water Purification, **3rd TYC Energy Materials Workshop: Materials for Electrochemical Energy Storage,** UCL, London, UK, Sept. 10th-12th, **2014**.

3. T.A. Ho and A. Striolo, Fluid Flows in Nanopores: Insight from Molecular Dynamics Simulation, **ChemEngDayUK 2014**, The University of Manchester, Manchester, UK, April 7th-8th, **2014**.

4. T.A. Ho, R.K. Kalluri, D.V. Papavassiliou, and A. Striolo, Microscopic and Macroscopic Properties of Interfacial Water, **AIChE Annual Meeting**, Pittsburgh, PA, October 28th-November 2nd, **2012**.

5. T.A. Ho, D.V. Papavassiliou, and A. Striolo, Water Hydrodynamic Slip: Molecular and Macroscopic Signatures, **ACS National Meeting**, San Diego, CA, March 24th-29th, **2012**.

6. T.A. Ho, D.V. Papavassiliou, L.L. Lee, and A. Striolo, Water on Surfaces: How the Molecular Structure Determines Hydrodynamics Slip, **AIChE Annual Meeting**, Minneapolis, MN, October 16th-21th, **2011**.

7. T.A. Ho, D. Argyris, and A. Striolo, Properties of Aqueous Electrolytes within Narrow Slit-Shaped Silica Pores, **APS March Meeting**, Dallas, TX, 21st-25th, **2011**.

8. T.A. Ho, D. Argyris, D.V. Papavassiliou, A. Striolo, L.L. Lee, and D.R. Cole, Interfacial Water Structure on Silica Surface: Force Field Effects, **AIChE Annual Meeting**, Salt Lake City, UT, November 7th-12th, **2010**.

9. D. Argyris, N.R. Tummala, T.A. Ho, A. Striolo, and D.R. Cole, Equilibrium Properties of Aqueous Electrolytes within Narrow Slit-Shaped Silica Pores: Molecular Dynamics Simulation Results to Design Separation Strategies, **AIChE Annual Meeting**, Salt Lake City, UT, November 7th-12th, **2010**.

10. D. Argyris, T.A. Ho, N.R. Tummala, A. Striolo, Aqueous Electrolyte Solutions on Silica Surfaces: Structure and Dynamics from Simulations, **Gordon Res. Conf.: Water and Aqueous Solutions**, Holderness School, Holderness, NH, August 8th-13th, **2010**.

Chapter 1   Introduction

Nanoscale fluid transport is usually referred to the fluid flow through a channel with the size along one or more directions below 100nm [1, 2]. At this small length scale, due to high surface area to volume ratio, the fluid-solid interaction at solid/fluid interface is one of the dominant factors that governs fluid behaviour [3]. Because of this unique feature many interesting transport phenomena particularly occur on this length scale including hydrodynamic slip boundary condition [4], diffusion limited reaction [5], overlap electric double layer and surface-charge-governed ion transport [6, 7], and single-file molecular transport [8]. These novel transport phenomena are discovered in many disciplines in science and engineering [9] and have initiated a wide range of innovative applications such as separation, water desalination, solvent and solute transport, energy conversion, and biosensing [1, 9-11]. In the remainder of this chapter I briefly introduce some related literature and state my research topic.

Perhaps, one of the most novel fluid transport phenomena that has been intensively studied in the past few decades is the hydrodynamic slip boundary condition. I could mention here an endless list of publications on this interesting topic over years [4, 12-20]. These publications reminisce the assumption that when a fluid flows inside a macrochannel the fluid near the surface travels at the same speed as the surface does. In other words, the fluid in contact with the surface is stationary with regard to the surface (i.e., no slip boundary condition) [21]. This no slip boundary condition is successfully applied to model various macroscopic experiments. However, the assumption of no slip boundary condition is violated when fluids flow inside nanochannels. Many experimental and simulation results strongly suggest that interfacial fluids can slip on nanochannel surfaces [4]. For example, Craig et al. [22]

used an atomic force microscope (AFM) to measure the hydrodynamic drainage force and revealed clearly that hydrodynamic slip boundary condition occurs. Zhu et al. [20] used surface force apparatus (SFA) to measure the drainage force between two approaching surfaces and concluded that the drainage force becomes up to two to four orders of magnitude less than expected by assuming the no-slip boundary condition, which is caused by the slip boundary condition at interface. Barrat and Bocquet [23] simulated the flow of Lennard-Jones fluid on a solid substrate. They concluded that when the contact angle of a liquid droplet sitting on a solid surface is large enough the boundary condition of the liquid flow on that surface remarkably differs from the no-slip boundary condition.

In the context of the hydrodynamic slip boundary condition, carbon nanotube (CNT) and graphene are the exceptional materials that offer a large degree of liquid slip. The flow enhancement, which is the ratio between the flow rate measured in experiment and that estimated using continuum hydrodynamic theory, is described as $\varepsilon = {Q_{slip}}/{Q_{no-slip}} = \left(1 + {8L_s}/{D}\right)$, where L_s and D are the slip length and diameter of CNT, respectively [24, 25]. The slip length reported for water flow in CNT and graphene varies from a few nm to a few mm[24]. For example, Majumder et al. [26] experimentally studied the water flow in 7nm CNT and reported very large slip length from 39×10^3nm to 68×10^3nm. As a result the flow rate inside 7nm [26] was found to be four to five orders of magnitude higher than that predicted from continuum hydrodynamic theory. Holt et al. [27] investigated water flow in sub-2nm CNTs and found the slip length from 140 to 1400nm. Thomas et al. [28] applied MD simulation to study pressure-driven water flow through 1.66-4.99nm CNT and reported the slip length varies from 30 to 110nm. Koumoutsakos et al. [29]

13

conducted non-equilibrium simulations to study water flow in graphite nanopore and estimated the slip length of 64nm. Maali et al. [17] indirectly measured the slip length of water on graphite surface using AFM and found the slip length of 8nm.

When the CNT diameter is small enough (0.81nm) the water flow through CNT exhibits another unique feature as reported by Hummer et al. [31]. In their molecular dynamics simulation study, they observed the simultaneous and continuous filling of CNT with a one-dimensionally ordered chain of water molecules (i.e., the single-file water transport mechanism). This special water configuration was also reported later by Suk and Aluru [32] in a molecular modelling study of the water transport through ultrathin graphene.

Rapid water transport when coupling with ion rejection can advance tremendously water purification applications. Working toward this goal, Fornasiero et al. [33] experimentally study ion rejection in sub-2nm CNT with the negatively charged group attached to the tube entrance. Their results indicate that a 98% of ion rejection can be achieved and that the electrostatic interactions dominate over steric and hydrodynamic effects in governing ion rejection. Corry [34] in a molecular dynamics simulation study mentioned that salt rejection of the 0.66, 0.81, 0.93, and 1.09nm CNTs under the hydrostatic pressure of 208MPa is 100%, 100%, 95%, and 58%, respectively. The narrow CNT not only extremely well rejects the ion but also conducts the water at several orders faster than the existing membranes do. Cohen-Tanugi and Grossman [35] studied water desalination across nanoporous graphene. They reported that the desalination performance of graphene membrane depends on pore size, chemical functionalization, and applied pressure. Hydroxyl groups attached to the edge of the graphene pore can roughly double the water flux due to

14

the ability of hydroxyl functional groups to substitute for water molecules in the hydration shell of the ion.

Ion transport through nanochannels is another important research topic because it is involved in various electrokinetic phenomena including electro-osmosis [36]. Because of the strong electrostatic interaction between ions and surface charges and because of confinement effects, the behaviour of ions inside nanochannels is expected to differ from bulk behaviour. For example, Stein et al. [6] experimentally studied the ion transport in 70nm silica nanochannel. They concluded that at low concentration, the conductance of nanochannel strongly deviates from the bulk behaviours. When the channel size is small, the electric double layer (EDL) near the top surface overlaps with the EDL near the bottom surface. Inside the overlap EDL most of ions are counterions and the number of counterions inside this EDL depends only on the surface charge. Because the channel conductance depends only on the number of the counterions it is independent of bulk electrolyte solution [7].

From the above discussions, one can easily recognize that insight into nanoscale fluid transport phenomena can be studied using molecular simulation and modelling [37-41]. Molecular dynamics (MD) simulation packages [42, 43] solve Newton's second law of motion for each atom $\sum_j \boldsymbol{F_{ij}} = m_i \frac{d^2 r_i}{dt^2}$, where m_i, $\mathbf{r_i}$, t, and $\mathbf{F_{ij}}$ are atomic mass, position of atom i, time, and force between atoms i and j, respectively. The force $\boldsymbol{F_{ij}} = -\nabla_i V_{ij}$, where V_{ij} is the interaction potential. The equation of motion is usually integrated within the cut-off distance, with the random initial configurations and initial velocities calculated from Boltzmann distribution [42]. To study the transport of fluid two types of flow are usually implemented. The first kind is the Couette flow, in which the atoms belonging to the surfaces are driven at a

15

constant velocity. The second type is the Poiseuille flow, in which a body force is applied on each fluid atom [21]. The trajectory of each atom and thermodynamic properties are obtained from the simulation. By analysing these outputs, the physical properties of the system can be achieved enclosing density profile, velocity profile, radial distribution function, orientation distribution, diffusion coefficient, etc. These results help to understand the behaviours of fluid at solid/fluid interfaces and fluid transport in nanochannel.

Inspired by the fact that many novel fluid transport phenomena are discovered and play important roles in numerous applications and that molecular simulation and modelling can be used to study nanoscale fluid transport, in this thesis I implement MD simulations to study fluid transport through nanochannels. In particular, I employ equilibrium and non-equilibrium atomistic molecular dynamics simulations using LAMMPS and GROMACS to investigate how fluids behave at interfaces (solid/liquid and liquid/gas interfaces) and how the interfacial fluid properties affect fluid transport. The solid substrates I consider are metal oxide surfaces, clay minerals, and graphene. The fluids are water, aqueous electrolyte solutions, and methane. My ultimate research goal is to search for the molecular signatures of the macroscopic observations. From the understanding of the mutual relation between molecular signatures and macroscopic observations, I learn how to tailor the fluid-solid interaction to improve the performance of practical applications as diverse as nano-fluidic devices, water desalination, energy storage, and shale gas exploration.

The thesis is organized as follow. In Chapter 2 I provide the basic background of molecular dynamics simulations. In Chapter 3 I report the results on the correlation between the molecular properties of interfacial water and the hydrodynamic

boundary condition, which is described in terms of slip vs. no-slip boundary conditions. Briefly, it is well known that hydrophobic surfaces tend to cause water slip whereas hydrophilic ones do not. My molecular dynamics simulation results, however, suggest that this dichotomy might be purely coincidental. Indeed, liquid water can slip on hydrophilic surfaces and the microscopic properties of interfacial water at solid/liquid interfaces are responsible for this observation. My finding could lead to the advancement of a variety of applications, including the design of hydrophilic nano-porous membranes with high permeation and self-cleaning hydrophilic surfaces.

In Chapter 4 I provide details of the study on the role of thin and mobile electric double layers in capacitive desalination and energy storage. Shortly, the structural and dynamical properties of the ions accumulating near the electrodes are the main factors that affect the performance of the supercapacitors and capacitive desalination devices. Using MD simulations I proposed a composite electrodes that favour the formation of compact and mobile EDL. These allow us to both effectively and efficiently store energy and purify water.

In Chapter 5 I present my molecular dynamics simulation results for the study of the water and methane migration in muscovite nanopore. The effects of flow patterns on the fluid transport and on the pore structure are investigated. The results indicate the movement of methane with respect to that of water changes when the flow pattern is altered. My results also illustrate the importance of the capillary force, due to the formation of water bridges across the clay pores, not only on the fluid flow, but also on the pore structure, in particular its width. When the water bridges are broken, perhaps because of fast fluid flow, the capillary force vanishes leading to significant

pore expansion. Because muscovite has similar structure to illite, a clay often found in shale rocks, these results advance my understanding regarding the mechanism of water and gas transport in tight shale gas formations.

Finally, in Chapter 6 I provide a comprehensive conclusion about the work presented in this thesis and the outlook. Note that in Appendix A, B, and C, I provide the supplemental information to support the work presented in Chapter 4. In particular, in Appendix A I present the work on comparing the properties of different water models simulated on graphene. In Appendix B, I provide the research on the polarizability effects in molecular dynamics simulations of the graphene/water interface. Finally, in Appendix C I report the additional details for the numerical integration of the Poisson equation.

Chapter 2   Methodology

2.1   Basic background of molecular dynamics simulation

Molecular dynamics simulation solves Newton's second law of motion for each atom

$\sum_j \boldsymbol{F_{ij}} = m_i \frac{d^2 r_i}{dt^2}$, where m_i, $\boldsymbol{r_i}$, t, and $\boldsymbol{F_{ij}}$ are atomic mass, position of atom i, time,

and force between atoms i and j, respectively. The equation of motion is usually

integrated with the random initial configurations and initial velocities calculated

from Boltzmann distribution [42]. Solving the equation of motion requires the input

of atomic mass, time step, and force. While it is straightforward to provide atomic

mass and time step (e.g., 1fs) the determination of the force between atom i and j

requires special care because MD simulation results strongly depend on the applied

force field. The force $\boldsymbol{F}$ is calculated from the interaction potential V_{ij} as $\boldsymbol{F_{ij}} =$

$-\nabla_i V_{ij}$.

2.1.1   Force field

In my simulations, non-bonded potential energy is described as:

$$V_{ij} = 4\varepsilon_{ij} \left[\left(\frac{\delta_{ij}}{r_{ij}} \right)^{12} - \left(\frac{\delta_{ij}}{r_{ij}} \right)^6 \right] + f \frac{q_i q_j}{\varepsilon_r r_{ij}} \tag{2.1}$$

The first terms in the right-hand side of equation (2.1) describe Lennard-Jones (LJ)

interaction. The last terms in the right-hand side of equation (2.1) describe

electrostatic potentials. The cross LJ interaction between unlike species is given by

the Lorentz-Berthelot mixing rules: $\sigma_{ij} = \frac{\sigma_{ii} + \sigma_{jj}}{2}$ and $\varepsilon_{ij} = \sqrt{\varepsilon_{ii}\varepsilon_{jj}}$. The calculation

of the non-bonded interactions is the most time consuming step in molecular

dynamics simulation. To speed up the computation, the interactions between two

atoms separated by a distance greater than the cutoff distance are ignored. While this approach works well for the Lennard-Jones interaction it is not suitable to implement for the system where charged atoms are present because of the significance of the long-range electrostatic interaction. The most popular method to approximate the electrostatic interaction is to partition it into a long-range component and a short-range component. The short-range component is calculated following equation (2.1) in real space and the long-range one is estimated in Fourier space using different approaches including Ewald, particle-mesh Ewald (PME), and Particle-Particle Particle-Mesh methods [42]. These methods require less computer time compared to the direct summation using equation (2.1). In my simulations I usually implement PME algorithm to calculate the long-range electrostatic interaction.

To simulate water molecule there is a lot of models available in literature including SPC [44], SPC/E [45], TIP4P/2005 [46], TIP3P [47], TIP5P [48], TIP4P/2005f [49], and SWM4_NDP [50] water models. SPC and SPC/E are the three sites rigid water models. Partial charges are assigned to oxygen and hydrogen atoms, while the center of LJ interactions is the oxygen atom. When the rigid SPC/E model is implemented, the two O-H bonds and the fictitious H-H bond lengths were constrained using the SHAKE algorithm [51]. TIP4P/2005 is a four sites rigid model. The oxygen atom carries no charge and is the center of LJ interaction. Partial charges are assigned to each hydrogen atom and to a dummy atom M located along the bisector of the HOH angle. TIP5P is a rigid five-sites water model. A partial charge is placed on each hydrogen atom, and partial charges of equal magnitude and opposite sign are placed on two lone-pair interaction sites. The oxygen atom has no charge and it functions as the center of LJ interactions. TIP3P is a three-sites rigid water model. It was developed to improve the energy and density for liquid water [47]. TIP4P/2005f is

the flexible version TIP4P/2005 water model [49]. The O-H bond and HOH angle are allowed to vibrate in this water models. SWM4_DP is a polarizable water model with four sites and Drude polarizability. The oxygen atom is the center of LJ interactions. The charge distribution is represented by three point charges: two hydrogen sites and one additional site positioned along the HOH bisector. Electronic induction is described by introducing a classical charged Drude particle attached to the oxygen by a harmonic spring. The oxygen atom carries a partial charge equal and opposite that of the Drude particle.

In my thesis, because I study the structural and dynamical properties of water molecules near solid surfaces the selected water model is expected to reproduce well, at least the properties of bulk water. Mark and Nilsson [52], in a study of the structure and dynamics of the TIP3P, SPC, SPC/E water models at 297K compared the radial distribution function g_{OO}, g_{OH}, and g_{HH} (a common property used to study structure of liquid water) and self-diffusion coefficients with experimental data. They reported that SPC/E model give the best bulk water dynamics and structure and SPC and TIP3P water models predict less water structure and faster diffusion when compared with experimental data for liquid water. Pusztai et. al [53] compared the radial distribution function of some water models including SPC/E, TIP4P, TIP4P-2005 with the neutron diffraction data and reported that the structure of liquid water predicted using these water models are reasonable when compared with experimental data. For SWM4-NDP water model, while the radial distribution function g_{OO} is consistent with experimental data the g_{OH} and g_{HH} are slightly different from experimental results [50]. In the Table 2.1 I compare the self-diffusion coefficients reported for some popular water models. For comparison the self-diffusion coefficient obtained from experiment is 2.3×10^{-5} cm^2/s [54].

Table 2.1 Self-diffusion coefficients reported for some popular water models

Water	SPC	SPC/E	TIP3P	TIP5P	TIP4P/2005	TIP4P/2005f	SWM4-NDP
D (10^{-5} cm^2/s)	3.85[55]	2.49[55]	5.13[55]	2.62[55]	2.08[46]	1.93[49]	2.33[50]

Among the popular water models mentioned SWM4-NDP reproduces the best experimental data of self-diffusion coefficient. While SPC, TIP3P, and TIP5P models overestimate TIP4P/2005 and TIP4P/2005f models underestimate the self-diffusion coefficient of water. Self-diffusion coefficient predicted using SPC/E model is slightly higher than experimental result.

A good water model is the model that reproduces all the properties of water molecules (e.g., dipole moment, dielectric constant, density, self-diffusion coefficient, radial distribution function, heat capacity, and phase diagram…). No water model in literature can reproduce all of these properties [56]. Because SPC/E is a simple (3 rigid sites) water model that reproduces well the experimental structure (i.e., radial distribution function g_{OO}, g_{OH}, and g_{HH} [52]), and self-diffusion coefficient of water [55] at ambient conditions it is the model of choice in my simulation.

Molecular dynamics simulation results strongly depend on the force field describing the interactions among various constituents in the simulated system. For example, in one of my publications [57] I compare the water properties predicted on the crystalline silica substrate. I implement four different force fields to describe the silica surface. These force fields yield different orientation and flexibility of surface hydrogen atoms, and also different interaction potentials with water molecules. My

results indicate the dependence of both structural and dynamical properties on the force field implemented. Comparison with experimental data is therefore necessary to discriminate the accuracy of implemented force fields. In this thesis, where this comparison is possible I will provide in details.

2.1.2   Algorithm

Solving the equation of motion requires the calculation of the pair-wise potential energy for all the atoms in the system. Due to the complicated nature of this calculation, there is no analytical solution to the equations of motion. Therefore, a numerical method is applied. Numerous numerical algorithms have been developed to integrate the equations of motion including Verlet and leap-frog [42].

In my simulations I usually apply leap-frog algorithm to solve Newton's equations of motion. According to this algorithm, the position and velocity are described as follow:

$$r(t + \delta t) = r(t) + v(t + \tfrac{1}{2}\delta t)\delta t \tag{2.2}$$

$$v\left(t + \tfrac{1}{2}\delta t\right) = v\left(t - \tfrac{1}{2}\delta t\right) + \frac{F(t)}{m}\delta t \tag{2.3}$$

In equation (2.3) the velocities are calculated at time $t + \tfrac{1}{2}\delta t$. These are then used to to calculate the positions r at time $t + \delta t$. In this way, the velocities leap over the positions, then the positions leap over the velocities. The velocities at time t can be approximated by equation (2.4):

$$v(t) = \tfrac{1}{2}\left[v\left(t + \tfrac{1}{2}\delta t\right) + v\left(t - \tfrac{1}{2}\delta t\right)\right] \tag{2.4}$$

2.1.3 Themostat

By simply solving the Newtonian equation of motion for all atoms in the system the NVE ensemble (i.e., microcanonical ensemble in which the number of atom, volume, energy are constant) is generated. Because molecular dynamics simulation results are expected to be compared with the experimental data, which are usually obtained at constant temperature, the NVT ensemble (i.e., canonical ensemble in which the number of atom, volume, temperature are constant) must be generated. Another reason I need to control the temperature, although it is not from the thermodynamic standpoint, is because of the numerical errors from MD simulation algorithm. Using thermostat can avoid steady energy drift from equilibrium state. Several thermostat methods are available in the literature including Andersen, Berendsen, Nose-Hoover [42]. For example, in Andersen thermostat the velocities of particles at each time step are reassigned the new values chosen from Maxwell-Boltzmann distribution [42, 58]. While this method requires no direct modification of the integration of equation of motion [58] it disturbs the velocity time correlations and slow down the kinetics of the system [42, 58]. Therefore, it should not be used to study dynamical properties. In Berendsen thermostat the deviation of the system temperature from target temperature T_0 is corrected slowly as $\frac{dT}{dt} = \frac{T_0 - T(t)}{\tau}$, where τ is the time constant. This approach does not yield a true canonical ensemble. However, when the system is large enough most of the ensemble averages is not remarkably affected, except the kinetic energy distribution [42]. In the widely used Nose-Hoover thermostat the equation of motion is modified as: $\frac{d^2 r_i}{dt^2} = \frac{F_i}{m_i} - \frac{p\zeta}{Q} \frac{dr_i}{dt}$. The friction parameter ζ is a dynamic quantity and its equation of motion is described as: $\frac{dp\zeta}{dt} = (T - T_0)$. In my

simulation I apply Noose-Hover thermostat because it allows one to rigorously generate a correct canonical ensemble [42].

Most of the equilibrium MD simulation results are quantified after equilibrium is established. To verify if the simulated system is equilibrated, temperature, structural and dynamical properties are monitored as a function of time. Equilibrium state is considered to be obtained when these properties do not change with simulation time.

2.1.4 Periodic boundary condition

Periodic boundary conditions enable a large (infinite) system to be simulated using a small simulation box containing the atoms of interest. MD simulation algorithm is developed in a way that the central box is surrounded by its images in all directions. Atom in the central box interacts not only with the atoms in the same box but also with the atoms in the image box. In this way, the atoms in simulated box experience the forces as they are in large system. In my simulation I use cubic box and apply periodic boundary condition in all directions.

2.2 Non-equilibrium simulation

In Figure 2.1 I present two types of flow geometry implemented in this thesis to study the transport of fluids inside nanochannels. The first type is the Couette flow (top panel) [59], in which the atoms belonging to the top surface are driven at a constant velocity and the atoms belonging to the bottom surface are kept stationary. The typical velocity profile for this flow is shown in the top right panel. The second type is the Poiseuille flow (bottom panel), in which accelerations are applied to fluid atoms to force them to move in a specific direction [21]. The surfaces in Poiseuille flow geometry are kept stationary. The characteristic velocity profile of the

Poiseuille flow is provided in bottom right panel. The non-equilibrium simulations are conducted until the velocity profile does not change with time (steady state flow).
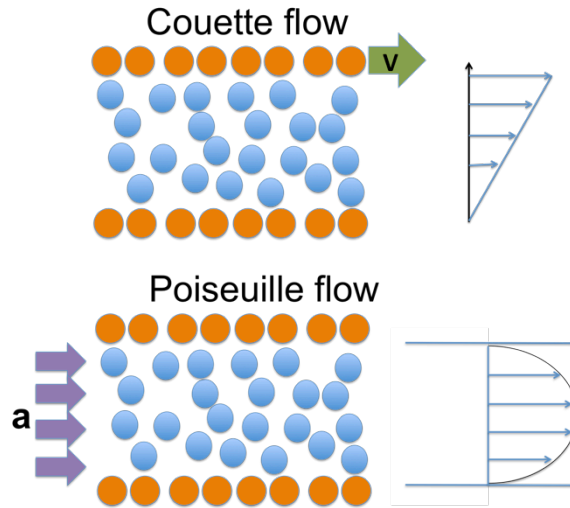

Figure 2.1 Schematic drawing showing the Couette (top) and Poiseuille (bottom) flow geometries used in my non-equilibrium simulations.

In non-equilibrium MD simulations, the applied velocity in Couette geometry and the applied acceleration in Poiseuille flow are very large compared to those encountered in experiments. This is due to computing power limitations [13, 21]. However, because it has been reported that the time scale for fluid flow scales linearly with the applied acceleration [27, 35], and because many non-equilibrium MD simulation results are consistent with the experimental data [27, 60], I expect that reliable data can be obtained using non-equilibrium MD simulation.

Two approaches are usually used to control the temperature in non-equilibrium simulation: thermostat is coupled to all atoms in the system and thermostat is coupled only to the surfaces. In the later case, confined fluids exchange heat with the wall during the course of the simulation [61]. In my simulation I apply the former case. When implementing this algorithm it is essential to subtract the nonzero streaming velocity in the direction of the flow when calculating the kinetic energy.

However, because the streaming velocity is un-known, only the velocity component perpendicular to the flow direction is usually thermostatted [62]. Since my streaming velocity is very small compared to the thermal velocity I include the streaming velocity in my temperature calculations. This will not result in significant error because small streaming velocity contributes only a tiny fraction of the total kinetic energy [63, 64]. Also, as demonstrated by Khare et al. [65], the differences in the temperature profiles expected at the shear rate considered in the this thesis are minimal and only present at the centre of the channel, the structure of interfacial water will not depend on the thermostat, and the conclusions in this thesis will hold independently on the algorithm considered.

The most common results presented in this thesis are the density and velocity profiles. In the left panel of Figure 2.2 I show the schematic drawing presenting my algorithm to compute the velocity/density profiles as a functions of position in between two substrates. I divide the volume into bins that spans entire length of simulation box in X and Y directions, and 1Å along the Z direction (dashed line). I then average the properties of the atoms in each bin over time. The averaged properties are plotted as a function of position z as shown in the middle panel. In the right panel of Figure 2.2 I report the schematic drawing presenting my algorithm to calculate the planar density distribution, for example the distribution of water in the first hydration layer on the plane parallel to the surface. In this calculation, only the water in the layer of interest is taken into account. I divide the volume into small box of $1x1Å^2$ in XY plane and average the density inside each box over time. The density is then plotted in a 3D contour plot. For other properties reported in this thesis where the algorithm is applied I will provide in details.
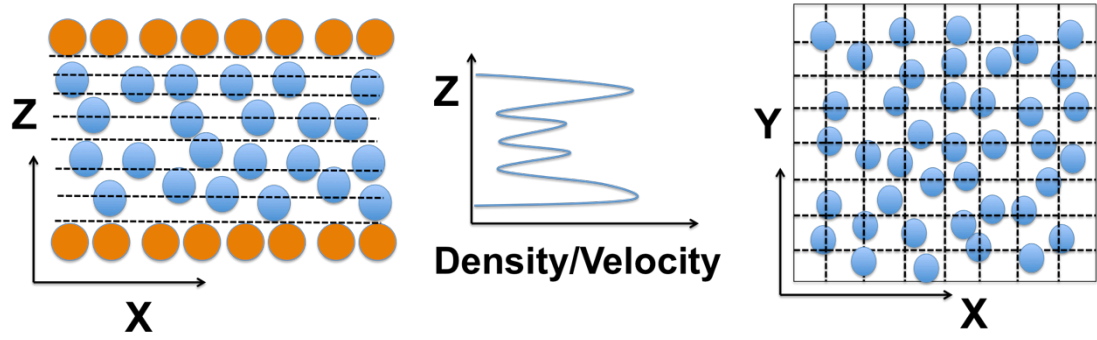
27

Figure 2.2 Schematic drawing showing the algorithm to calculate the profiles.

Chapter 3 Correlation between Interfacial Water Properties and Hydrodynamic Boundary Conditions

The material presented in this chapter was published in 2011 in volume 108, pages 16170-16175 of The Proceedings of the National Academy of Sciences of the United States of America.

3.1 Abstract

Understanding and predicting the behaviour of water, especially in contact with various surfaces, is a scientific challenge. Molecular-level understanding of hydrophobic effects and their macroscopic consequences, in particular, is critical to many applications. Macroscopically, a surface is classified as hydrophilic or hydrophobic depending on the contact angle formed by a water droplet. Because hydrophobic surfaces tend to cause water slip whereas hydrophilic ones do not, the former surfaces can yield self-cleaning garments and ice-repellent materials whereas the latter cannot. The results presented herein suggest that this dichotomy might be purely coincidental. My simulation results demonstrate that hydrophilic surfaces can show features typically associated with hydrophobicity, namely liquid water slip. Further analysis provides details on the molecular mechanism responsible for this surprising result.

3.2 Introduction

Protein folding [66], micelle and cellular membrane formation [67], and frictionless flow of water through carbon nanotube membranes [68-70] are only some manifestations of hydrophobic effects. Flat surfaces are arbitrarily classified as hydrophobic when a water droplet yields a contact angle larger than 90°, hydrophilic

otherwise. A now famous 2008 commentary by Granick and Bae [71] initiated a scientific discussion to identify the molecular signature of hydrophobic vs. hydrophilic surfaces. The question is whether or not molecular properties exist for interfacial water molecules that change with the surface 'degree of hydrophobicity'. Identifying such properties could advance practical applications, e.g., designing self-cleaning surfaces, as well as fundamental scientific endeavours including understanding self-assembly [72].

Molecular simulations should allow the discovery of such molecular signatures because they allow a systematic variation of the properties of a surface, as well as of surface-water interactions [73]. Although the resultant substrates may not be realistic, the results are useful to interpret nature and to design innovative materials. It has so far been possible to relate some macroscopic observables to the degree of hydrophobicity (i.e., contact angle to adsorption free energy [74]). Garde and coworkers employed equilibrium molecular dynamics to determine a number of quantities, including local density, contact angle, and adsorption of small solutes for water near surfaces of varying degrees of hydrophobicity [75]. While the local water density provided unsatisfactory characterization, the probability of cavity formation was found to be large near hydrophobic and small near hydrophilic surfaces.

The present work focuses on the relation between one important macroscopic signature of hydrophobic surfaces, the hydrodynamic liquid slip, to molecular interfacial water properties. Large liquid slip on hydrophobic surfaces could reduce the drag in vessels navigating the seas, the pressure drop encountered by fluids flowing inside pipes, and even repel ice formation. At nano length scale, liquid slip seems to appear when a fluid does not wet a surface [4, 12, 59, 76, 77]. However, the

degree of slip depends on the surface roughness [4, 78]. Liquid slip is also found on micro-structured hydrophobic surfaces [79, 80]. On these textured surfaces, if the liquid completely penetrates into the rough grooves (Wenzel state) fluid adheres more strongly to the textured surface when compared to Cassie state (i.e., the liquid does not penetrate the grooves) [81]. In Cassie state liquid/solid interface actually consists of two interfaces: liquid/solid and liquid/vapour [82]. Liquid/vapour interface is the shear-free interface that offers liquid slip [83]. Since in Wenzel state liquid adheres strongly to the textured surface causing high contact angle hysteresis Cassie textured surface is usually preferred for some water repellent practical applications including self-cleaning surface [81]. Because the extent of slip varies systematically with the contact angle [14, 20, 84], in the case of water, slip should occur on hydrophobic surfaces [17]. In the present study the extent of water slip is quantified at various solid interfaces. Equilibrium and non-equilibrium MD are employed to search for molecular-level hydrophobic signatures.

3.3   Results and discussions

The most important result presented herein is the demonstration that contact angles larger than 90° are not necessary to attain hydrodynamic slip. Instead, slip is determined by the distribution of water molecules at contact with the solid and by the strength of water-solid interactions. When favourable adsorption sites exist, but are separated from each other by well-defined sub-nanometer distances, no slip is observed. When favourable adsorption sites are present that are close to each other, liquid slip can occur, provided water-solid attractions are not too strong. Because hydrophobic surfaces, such as graphite, are typically characterized by uniform distributions of interfacial water molecules, while hydrophilic ones, such as

crystalline silica, present isolated highly attractive adsorption sites that water molecules readily occupy and seldom leave [85], experiments typically show hydrodynamic slip on hydrophobic surfaces and no slip on hydrophilic ones. My results suggest that such observations are just a coincidence: should hydrophilic surfaces be manufactured with high density of adsorption sites close enough to each other to allow water molecules to easily migrate from one to the next, such hydrophilic surfaces could show liquid slip. My interpretation is consistent with a recent simulation study for the thermal diffusion of carbon nanotube membranes [86], with the molecular mechanism proposed for liquid slip [19], and with experimental observations reported for alkanes [87]. My interpretation could also explain the experimental results by McCarthy et al. [88], according to which the contact angle hysteresis, and not the static contact angle, should be used, macroscopically, to determine the hydrophobic vs. hydrophilic character of a surface.

In Figure 3.1 I show representative equilibrium simulation snapshots for water droplets of 1,000 water molecules on three surfaces. In all cases, water molecules are described using the SPC/E model [45]. The surface on the top is MgO, simulated by the CLAYFF force field [89]. Many experimental results demonstrated that water dissociates on MgO surface to from surface hydroxyl group [90-92]. Because in my model water dissociation is not permitted, in general my modelled MgO surface is not realistic. However, by applying this simple MgO model we can easily alter the surface properties, a common approach applied in MD simulation to study how the strength of surface/water interaction and the surface morphology can affect interfacial water properties. All simulations were conducted using LAMMPS [43], and performed at ambient conditions. Following Ref. [93] a plane perpendicular to the surface and passing through the droplet centre of mass was identified. Along this

plane the drop was sectioned in 0.5Å-wide bins used to calculate the atomic densities. The vacuum/water interface was defined when the water density decreased to 0.2 g/cm3. The contact angle simulated on MgO surface is ~47° indicating a hydrophilic surface. I arbitrarily modify the MgO surface following two protocols. In the first, I reduce the electrostatic interactions between water and the MgO atoms by a factor W, comprised between 0 and 1. When W=1 I recover MgO. When W=0 the surface interacts with water molecules only via weak dispersive interactions, and the contact angle becomes ~130° (bottom left panel), characteristic of a hydrophobic surface. In the second modification protocol I maintain both dispersive and electrostatic surface-water interactions consistent with those of MgO, but I reduce the lattice parameter that separates Mg and O atoms by a factor D. When D=1 I recover MgO. As D decreases the surface atomic density increases. When D=0.62, bottom right panel, the contact angle is ~30°, consistent with a very hydrophilic surface. It is worth mentioning that the distance between Mg and O atoms in MgO is 0.21nm, less than the diameter of one SPC/E water molecule. Thus all surfaces considered here are atomically smooth.

In the middle panels of Figure 3.1 I show the drop profiles used to calculate the contact angles from my simulations as W and D vary. Macroscopically, the MgO surface, originally hydrophilic, becomes hydrophobic when W decreases. The contact angle changes non monotonically as D decreases, although remaining in all cases lower than 90° (consistent with hydrophilic surfaces), and reaches ~30° when D=0.62.

The non-monotonic dependence of the contact angle with changes in D can be explained based on the orientation of the water molecules at contact with the solid

substrate, in qualitative agreement with the arguments proposed by Giovambattista et al. [93] and by Lee et al. [94], and also by the density of water molecules within the first hydration layer. To quantify these effects I report in Figure 3.2 the density profiles for oxygen and hydrogen atoms of water molecules in the direction perpendicular to the solid substrates as D decreases from 1 to 0.62. The results are only shown up to 4Å from the substrates.

When D = 1 (left) the first oxygen peak is found at z = 2.45Å and two hydrogen peaks are found at z = 1.65Å and z = 3.05Å. The first hydrogen peak is closer to the surface than the first oxygen peak, indicating that, on average, one of the OH bonds of about half the water molecules belonging to the first hydration layer points towards the surface. Similar density distributions are found when D = 0.9 (second panel from left), suggesting that the orientation of water molecules does not change significantly when D changes from 1 to 0.9. However, the oxygen peak is found at z = 2.65Å when D=0.9, farther from the surface than the first oxygen peak on the D = 1 surface. The oxygen peak on the D = 0.9 surface is also broader and less intense than that on the D = 1 surface. These features suggest that interfacial water molecules are, to some extent, repelled from the surface when D is decreased from 1 to 0.9. As a consequence of this molecular-level repulsion the contact angle increases from ~47° to ~72°, as shown in Figure 3.1.
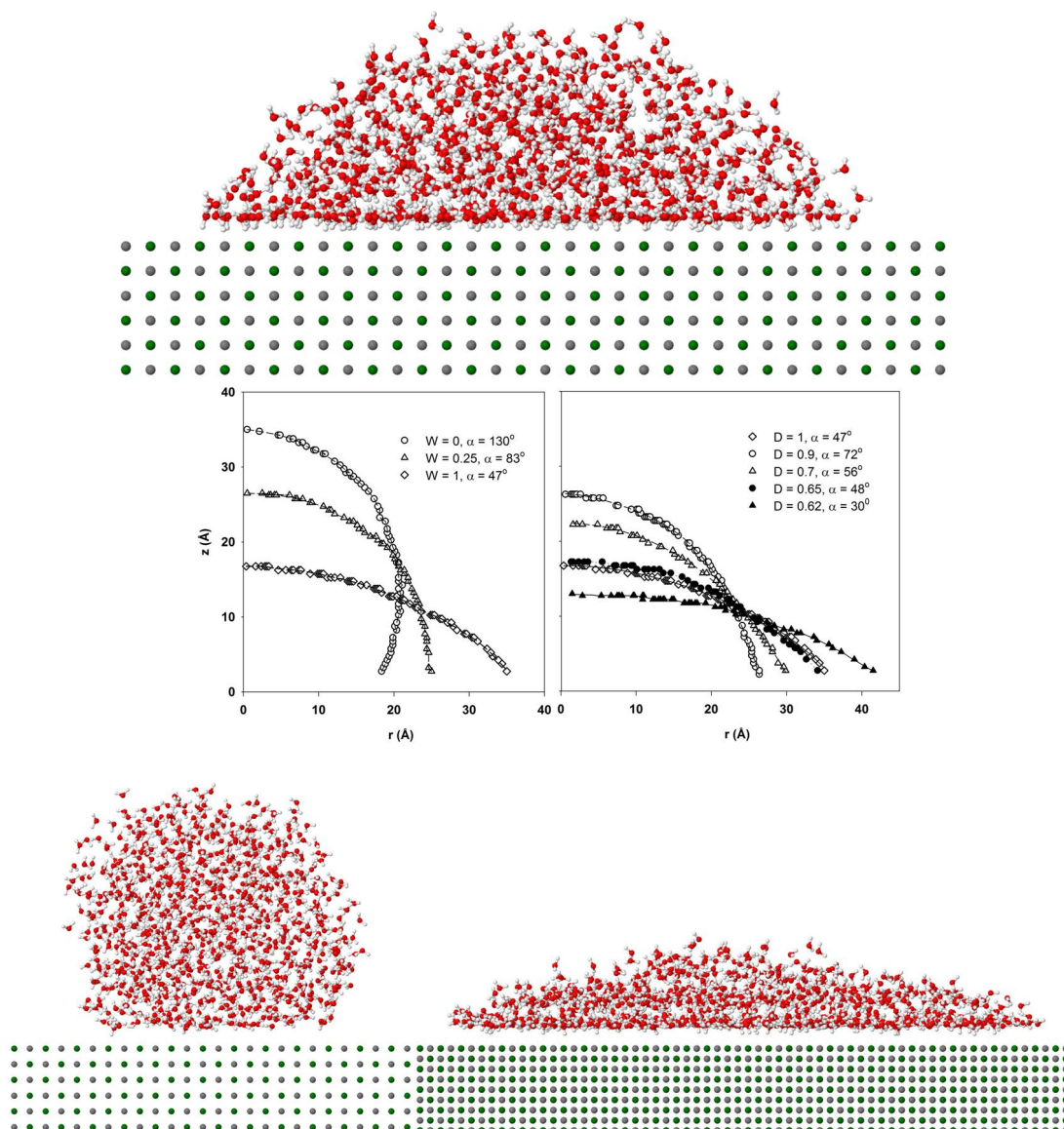
Figure 3.1 Top: Simulation snapshot for one droplet of 1,000 SPC/E water molecules on MgO, showing that water wets the solid surface (water dissociation is not allowed). Middle: Drop profiles obtained from simulation of water droplets on the various surfaces considered. As W decreases (left) the contact angle systematically increases leading to hydrophobic substrates. As D decreases (right) the contact angle changes, but not monotonically. In general the substrates remain hydrophilic, but when D=0.62 very hydrophilic surfaces are obtained. Bottom: Simulation snapshots for the most hydrophobic (left, W=0, contact angle ~130°) and the most hydrophilic (right, D=0.62, contact angle ~30°) substrates considered herein.
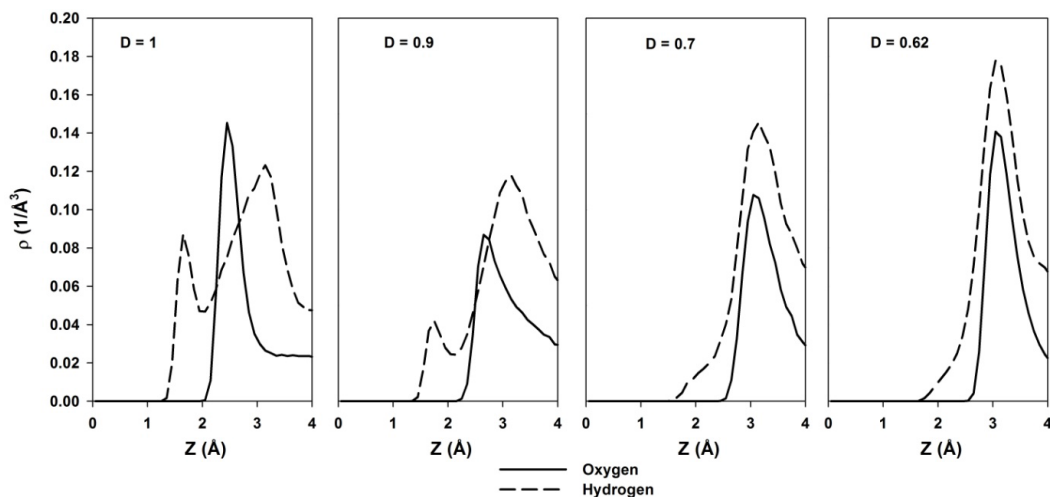
Figure 3.2 Density profiles in the direction perpendicular to the solid substrate for oxygen (continuous line) and hydrogen atoms (broken lines) of water molecules within the droplets used to calculate the contact angles of Figure 3.1. Because for the water droplet it is difficult to determine the accurate volume that water molecules occupy I estimated the density in these cases based on the same volume of a rectangular box. As a result, the densities reported here are smaller than the true densities. Comparison should only be made among these cases. Results are shown for water on model MgO surfaces in which D decreases from 1 (left panel) to 0.62 (right panel). Note that both the intensity and the position of the various peaks change as D changes, reflecting changes in orientation of contact water molecules as well as in the density of the hydration layers.

More dramatic are the changes in the density profiles for both oxygen and hydrogen atoms of interfacial water obtained when D is decreased from D = 0.9 to D = 0.7 (third panel from left) and D = 0.62 (right panel). The position of the first O peak is shifted to slightly larger distances from the solid (to z = 3.05Å), but the intensity of the peak increases as D decreases, as a consequence of the increased water-solid attraction due to the enhanced atomic density in the solid substrate. In addition, the first peak for the hydrogen atoms of water becomes centred on the position of the first O peak when D = 0.7 or less, and it is slightly more intense than the O peak. This indicates that only a few OH bonds are pointing towards the D = 0.7 and D = 0.62 surfaces (note the small shoulders near the surfaces in the H density profiles),

that more than one OH bonds per water molecule, on average, are approximately parallel to the solid surface, and that the rest are pointing away from the surface. The orientation of interfacial water molecules remain consistent with the description just provided as D decreases from 0.7 to 0.62, but the density of both first O and H peaks at contact with the D=0.62 surface are much larger than those near the D=0.7 surface, as a consequence of the increased surface-water attractions. These changes in the orientation and density of contact water molecules are responsible for the decrease in the equilibrium contact angle found in my simulations as D decreases from 0.9 to lower values.

In Figure 3.3 I report, on the top left panel, one simulation snapshot to illustrate the protocol implemented for determining the presence/absence of liquid slip. To investigate the presence/absence of liquid slip one could implement either the Couette or the pressure-driven Poiseuille flow. Hydrodynamic slip is independent of the flow type [95]. Following Thompson and Troian [59], I simulate a Couette flow. Two parallel mirror-image solid surfaces are placed along the Z axis. The bottom surface is maintained at a fixed location. The top surface is displaced along the X direction with a constant velocity, $v_X = 100$m/s. Admittedly, the resultant shear rate, which is limited by the current state-of-the-art computational resources, is much higher than shear rates typically explored experimentally [21], yet comparable to those found in high performance lubrication applications such as rocket engines and computer disk drives [65]. Nevertheless, important insights can be attained from simulations, as shown, for example, by Martini et al. [19]. In most simulations reported here the atoms within the solid are maintained rigid. To ensure that this simplification does not introduce spurious effects [18], I conducted representative simulations in which the surface atoms vibrate, while maintaining the entire system

37

at the desired temperature. No statistically significant differences were observed between the results obtained for MgO. The results presented also do not depend on the thermostat (Berendsen vs. Nose-Hoover). It should be pointed out that the Couette-type simulations are initiated after the thin film of water confined within the slit-shaped pores has been equilibrated at ambient conditions. Consequently, liquid water wets all surfaces considered in the non-equilibrium simulations discussed herein.

At steady states the water molecules confined in the gap between the two surfaces manifest a characteristic velocity profile $[v_{w,X}(z)]$. In the top right panel of Figure 3.3 I show the oxygen atomic density profile and the velocity profile for water molecules as a function of their Z position. The reference $z = 0$ is the centre atomic position of the top layer of the bottom surface. The slip velocity is defined as the velocity of the water in the first hydration layer [96]. The slip length L_s is attained by extrapolating the velocity profiles from reference $z=0$ to the distance at which the fluid velocity equals the surface velocity (i.e., $v_x=0$ m/s) [97]. A small uncertainty is expected when estimating slip length because it depends on the definition of the wall position (reference $z = 0$). Sometime the position of the wall is taken at the centre of mass of the innermost layer of solid wall. Sometime it is taken at a distance of σ (Van der Waals size of solid atom) away from the surface [16]. The temperature is maintained at 300K, as in all other cases. The surfaces considered are MgO. The results show that the contact water layer at $z = 2.5$Å has the same velocity as the immobile surface. This observation confirms that MgO shows no liquid slip, in qualitative agreement with the contact angle of ~47°, denoting hydrophilic properties. In the bottom panels I compare the velocity for confined water molecules as a function of

their position within the slit-shaped pore when W (left) and D (right) decrease. Liquid slip appears when the velocity of those water molecules in contact with the solid show different velocity than the solid. No slip is found otherwise. As W decreases the surface becomes more hydrophobic, while as D decreases the surface remains hydrophilic and the contact angle can be as low as ~30° (see Figure 3.1). The results in Figure 3.3 (left) show that while the MgO surface is characterized by no slip, as the surface becomes more hydrophobic liquid slip appears (slip velocity observed when W=0 is v_x=35 m/s), as expected [84]. More interestingly, when the surface becomes very hydrophilic (D=0.62) (right panel) slip is also possible (slip velocity is v_x=45 m/s), which contradicts conventional wisdom. It should be reiterated that for all cases considered the surfaces are atomically smooth and water wets all surfaces.

The extent of hydrodynamic slip is expected to depend on the shear rate. For example, Priezjev [98] found that at weak surface/fluid interaction the slip length increases nonlinearly with the shear rate and at strong surface/fluid interaction the slip length linearly increases when the shear rate increase. Ulmanella and Ho [99] reported that the slip velocity increases when the shear rate increases. Thompson and Troian [59] concluded that at sufficiently low shear rate the slip length equals its limiting value and at high shear rate the slip length increases rapidly with the shear rate. To investigate this ability, in Figure 3.4 I report the velocity profiles obtained after the Couette flow was fully established for surfaces with varying W (left panel, W=1, 0.25, and 0) and with varying D (right panel, D=1, 0.7, and 0.62). The shear rate in this simulation equals half of that considered in Figure 3.3 (i.e., the top surface is driven along the X direction with a constant velocity, v_X = 50m/s). Qualitatively, the results are consistent with those obtained at higher shear rates (no

slip on MgO, hydrodynamic slip on surfaces with W<1, and on surfaces with D<0.7), but the slip length was found to decrease as the shear rate decreases (see Table 3.1), in qualitative agreement with results by Thompson and Troian [59]. To estimate the extent of slip at much smaller shear rates, in alternative to non equilibrium MD simulations one could employ the Green-Kubo formalism as applied to results from equilibrium simulations, following for example Barrat and Bocquet [76]. These authors found that slip lengths estimated conducting non equilibrium MD simulations were comparable to those obtained employing the Green-Kubo formalism for Lennard-Jones fluids simulated at equilibrium between two solid surfaces.

In Figure 3.5 I report the in-plane density profiles obtained from equilibrium simulations for water molecules within the first layer near four surfaces: the MgO surface (top left); the W=0 surface (top right); the D=0.9 surface (bottom left); and the D=0.70 surface (bottom right). These results are obtained for water confined within the slit-shaped pores used for the Couette-flow calculations, but at equilibrium ($v_X = 0$m/s). The algorithm to calculate the planar density distribution is discussed in Chapter 2. On the two surfaces on the left no hydrodynamic slip is observed. Slip is observed on both surfaces on the right (see Figure 3.3). The density profiles of Figure 3.5 suggest that for slip to occur it is necessary for the water molecules adsorbed on the contact layer to be able to migrate from one adsorption site to the next without leaving the contact layer, irrespectively of the contact angle.
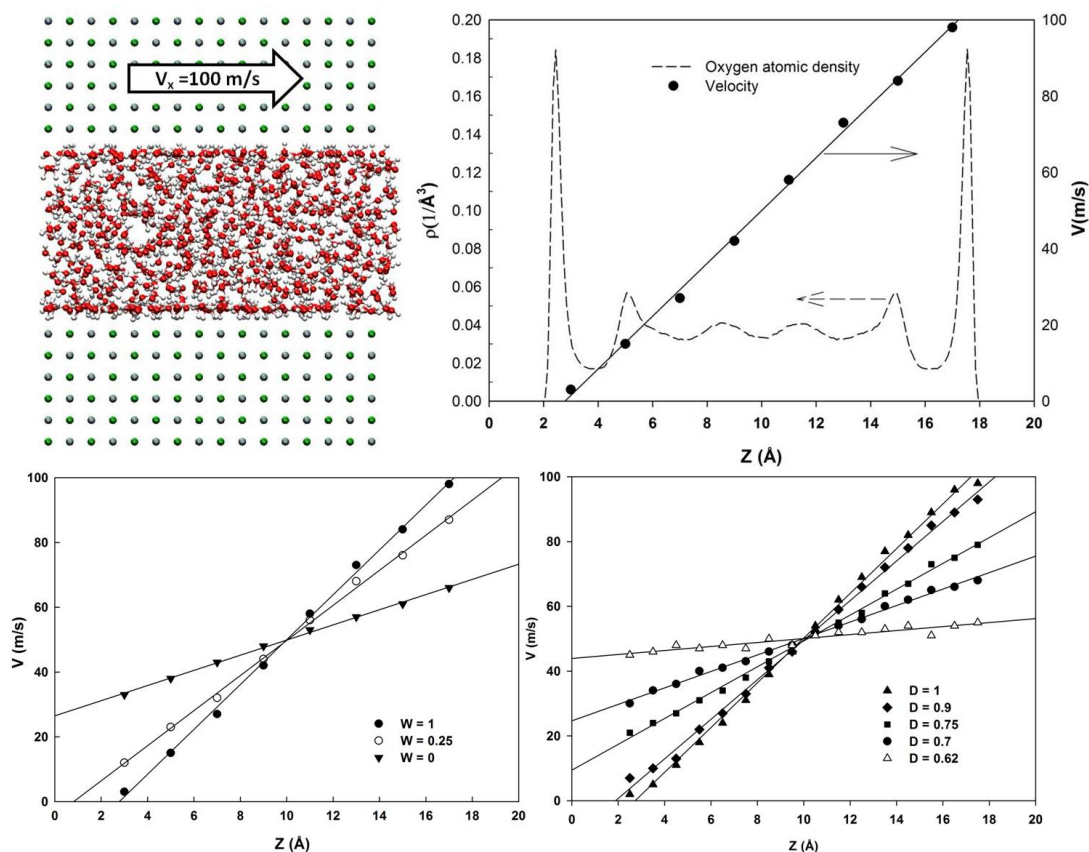
Figure 3.3 <u>Top</u>: Simulation snapshot illustrating the protocol implemented to study the transport properties for confined water in a Couette flow (left). The bottom surface is maintained in its fixed position, while the top one is moved with constant velocity of 100m/s (0.001Å/fs) along the X direction. When the Couette flow is fully established I can study the density profile of the oxygen atoms of the confined water, as well as the velocity of the confined water molecules along the X direction as a function of their position within the narrow slit-shaped channel (right, example for MgO substrate). When the velocity of the water molecules in contact with the solid substrates equals that of the solid (as in the case of MgO) the simulations suggest no slip. On the contrary, when the water velocity in contact with the solid surface differs from that of the solid, hydrodynamic liquid slip is observed. <u>Bottom</u>: Velocity profiles for confined water molecules as a function of the position within the narrow slit-shaped channel when reducing W from 1 to 0 (left) or D from 1 to 0.62 (right). In all cases T=300K. The results show that when W = 0.25 slip begins to be observed (it becomes very evident at W = 0). More interestingly, slip is also detected for hydrophilic surfaces, when D is 0.75 or less. Lines are guides to the eye. Estimations for slip lengths, useful for hydrodynamic calculations, can be attained by extrapolating the velocity profiles shown above to the distance at which the fluid velocity equals the surface velocity [97]. For example, when D=0.62 the slip length is ~ 6.7nm.
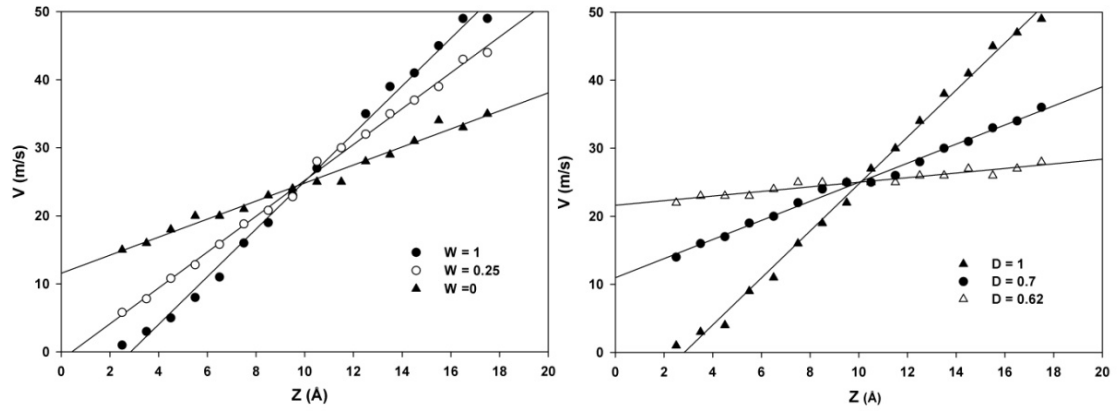
Figure 3.4 Velocity profiles obtained after the Couette flow was fully established for water confined in slit-shaped channels. The bottom surface is stationary. The top surface moves with constant velocity of 50m/s. Results on the left panel are for surfaces of varying W. Results on the right panel are for surfaces of varying D.

Table 3.1 Slip length estimated for water on two surfaces (D = 0.7 and W = 0) as a function of shear rate. Note that the calculation of slip length L_s depends on the choice of reference Z=0. If reference z =0 is taken at a distance of $\sigma \sim 4$Å (Van der Waals size of solid atom) away from the surface, the slip length L_s reported in this table become larger ($L_s + \sigma$).

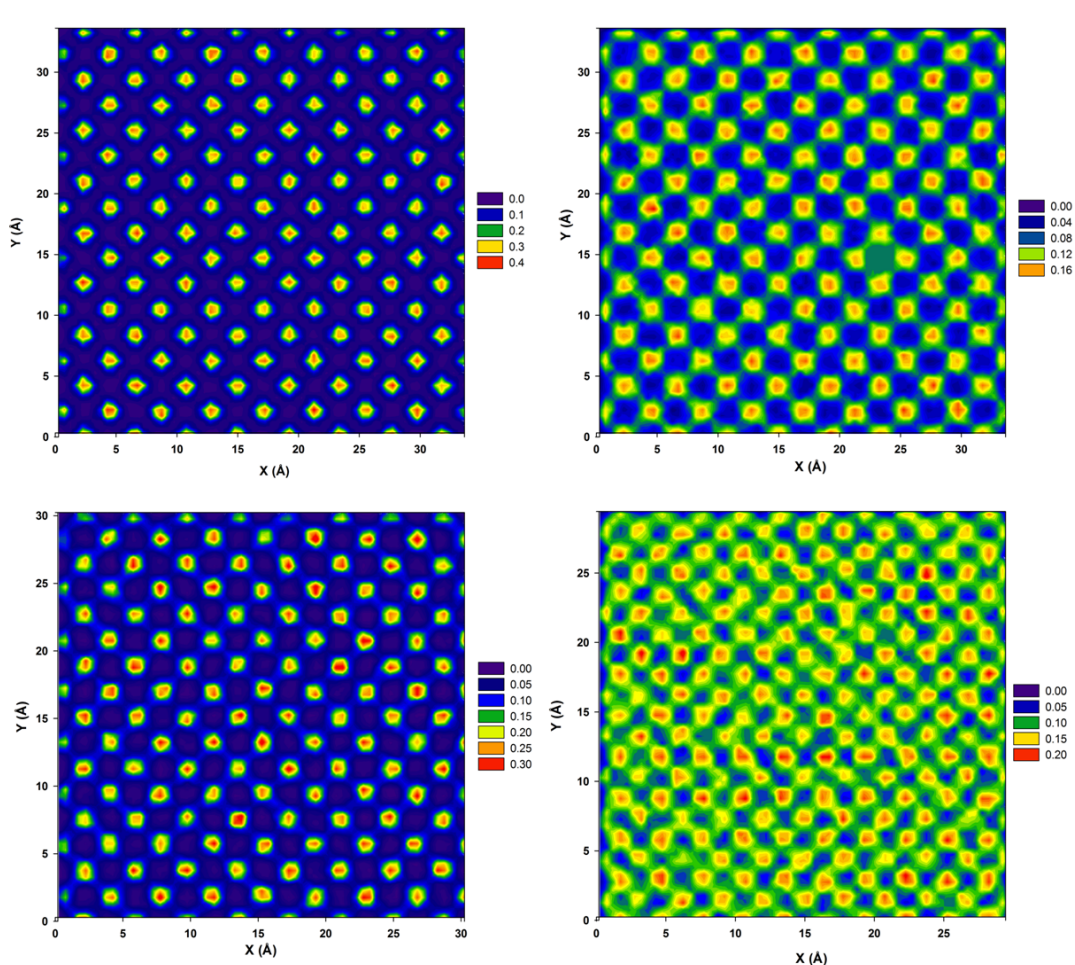| Shear rate	D = 0.7 surface	W = 0 surface
0.5×10^{11} (s^{-1})	9.6Å	11.2Å
0.25×10^{11} (s^{-1})	7.7Å	8.6Å

Figure 3.5 Surface density distribution of water molecules in the first layer on MgO surface (top left), W=0 surface (top right), D=0.9 surface (bottom left), and D=0.70 surface (bottom right). Colour scale reflects the densities (number of atoms per $Å^3$). The red areas indicate the positions preferably occupied by water molecules in the contact layers. On the MgO surface (top left) and on the D=0.9 surface (bottom left) water molecules adsorb in well defined adsorption spots. No connection between these high-density regions implies that water molecules seldom migrate from one to another. As a consequence, no hydrodynamic slip can be observed. On the W=0 (top right) and on the D=0.70 (bottom right) surfaces the preferable adsorption sites are connected to each other (see green lines connecting the yellow/red spots). On these surfaces water molecules can easily migrate from one preferable adsorption site to a neighbouring one, leading to liquid slip.

In Figure 3.6 I report the trajectory of representative contact water molecules near three substrates as obtained after the Couette flow is fully established. Lateral and

top views of the trajectories are reported on top and middle panels, respectively. The lateral views identify, via two red lines, the position of the contact water layer. The top views also report the atomic positions on the solid substrates. The left panels are for contact water on MgO (which shows no slip). The centre panels are for contact water on the W=0 surface (which shows slip). The right panels are for contact water on the D=0.70 surface (which shows slip). The trajectories have been obtained from 35, 20, and 30ps – long simulation fragments, respectively. On MgO (left), in order to migrate from one adsorption site (on top of a surface Mg atom) to a neighbouring one, the water molecule has to first desorb from the contact water layer, manifesting a hopping diffusion mechanism. On the contrary, the water molecules on either the W=0 and D=0.70 surfaces easily migrate from one adsorption site to a number of neighbouring others without necessarily leaving the contact layer. This slide mechanism is possible because the preferable adsorption sites are connected to each other on the W=0 and D=0.70 surfaces. As a quantification of the interpretation just provided, on the bottom panels of Figure 3.6 I report the density distributions of water molecules at contact with the three surfaces just described. These results differ from those presented in Figure 3.5 because they are obtained after the Couette flow has reached steady states. On MgO the density distribution obtained when shear is applied (left bottom panel in Figure 3.6) is practically indistinguishable from that obtained at equilibrium (Figure 3.5), because water molecules move from one preferential adsorption site to another following the hopping trajectories described above. On the contrary, the density distributions obtained under shear on the W=0 and on the D=0.70 surfaces (centre and right bottom panels in Figure 3.6) clearly show the formation of 'density bridges' that connect the preferential adsorption sites observed at equilibrium (see Figure 3.5). These density bridges are due to water

44

molecules sliding from one preferential adsorption site to another upon the application of shear, following the trajectories described in the top and middle panels of Figure 3.6.
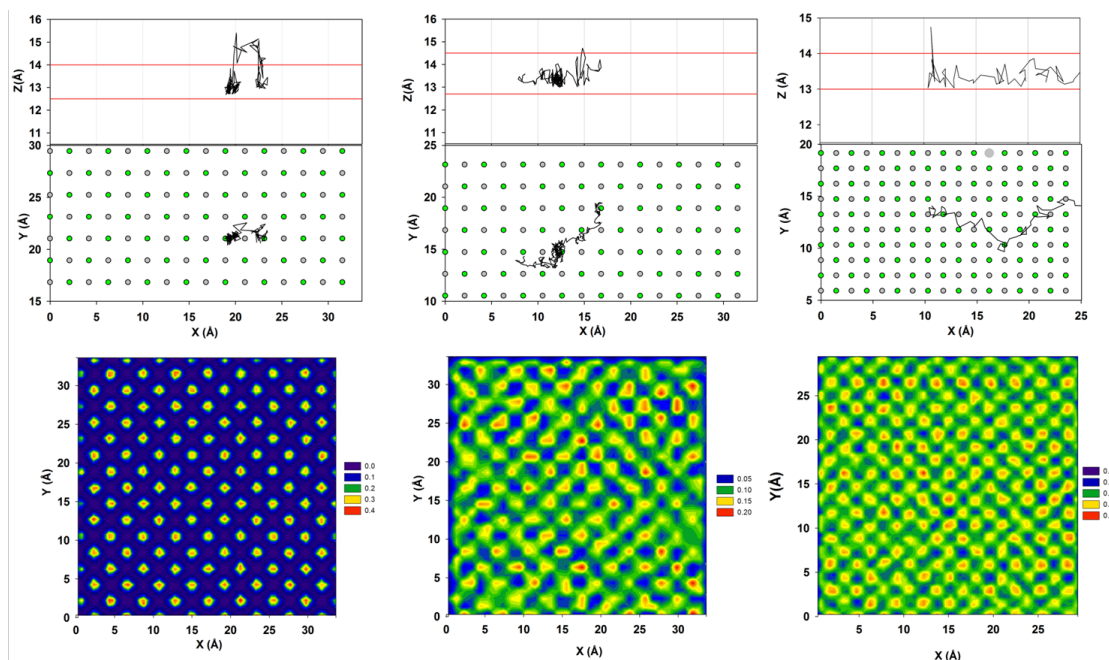

Figure 3.6 Top: Trajectory of three representative water molecules as they migrate from one adsorption site to neighbouring ones on MgO (left, no slip), W=0 surface (middle, slip), and D=0.70 surface (right, slip). The two red lines on the top panels identify the position of the contact water layer. Surface solid atoms are identified by green and grey circles (Mg and O, respectively). The black line describes the trajectory of one water molecule. On the MgO substrate the trajectory is 35 ps long. On the W=0 surface the trajectory is 20 ps long. On the D=0.70 substrate the trajectory is 30 ps long. Bottom: Planar density distributions are reported on the bottom panels for water molecules at contact with the three surfaces after the Couette flow is fully established. Colour scale reflects the densities (number of atoms per $Å^3$).

To verify whether the distribution of water molecules on the contact layer is sufficient to support hydrodynamic slip vs. no-slip conditions I conducted additional simulations for the D=0.7 surface (on which hydrodynamic slip was observed), in

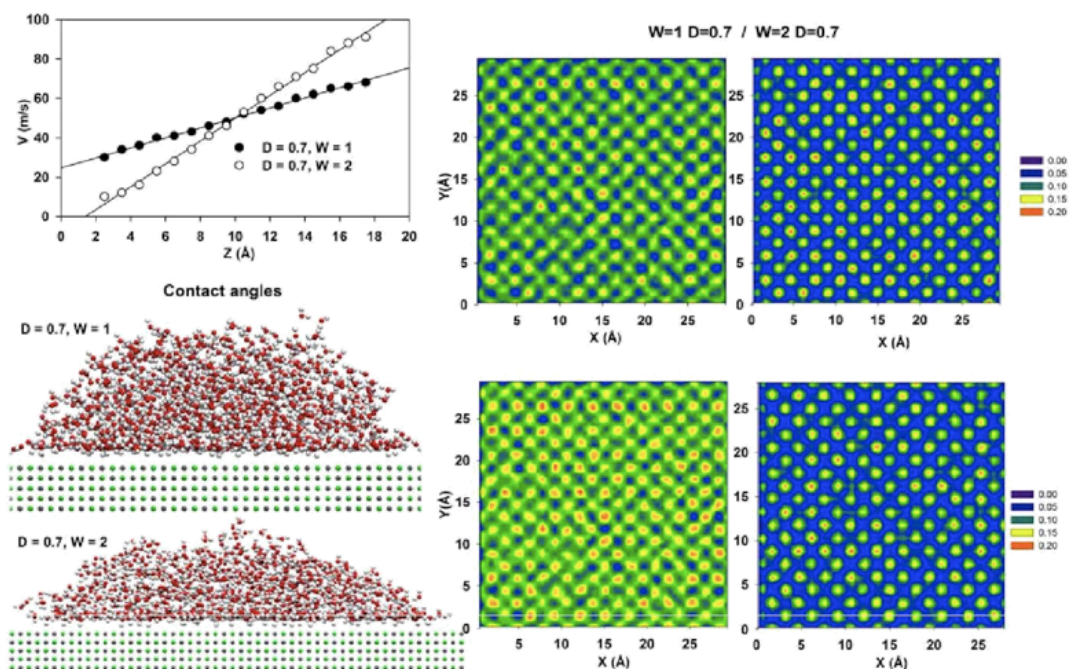which I doubled the electrostatic interactions between water and surface (W=2 in the nomenclature adopted herein).

Figure 3.7 <u>Bottom left</u>: Representative simulation snapshots for water droplets supported on model surfaces represented by W=2 D=0.7, and W=1 D=0.7, demonstrating that both surfaces are hydrophilic. <u>Top left</u>: Velocity profiles obtained for water molecules within slit-shaped channels when the Couette flow is fully established and the confining surfaces are either W=1 D=0.7 (large slip) or W=2 D=0.7 (little slip). <u>Right</u>: Planar density profiles at equilibrium (top) and after the Couette flow is fully established (bottom) for water molecules at contact with either the W=1 D=0.7 or the W=2 D=0.7 surface. Colour scale reflects the densities (number of atoms per $Å^3$)

In Figure 3.7 I compare the results obtained on the W=1 D=0.7 and on the W=2 and D=0.7 surfaces. The results considered are contact angles (bottom left panels), velocity profiles after the Couette flow is fully established (top left panel), and density profiles for water molecules within the contact layers (right panels).

Based on the contact angles, my results show that both surfaces are hydrophilic, although the contact angle is lower for the W=2 and D=0.7 (49°) than for the W=1 and D=0.7 (56°) surface. The velocity profiles show that while hydrodynamic slip is observed for the W=1 D=0.7 surface, as described in Figure 3.3, hydrodynamic slip significantly decreases when W increases to 2.

The planar density profiles are shown on the W=1 D=0.7 surface and on the W=2 D=0.7 surface at equilibrium (top panels) and after the Couette flow is fully established (bottom panels). As described in Figure 3.5, on the W=1 D=0.7 surface the planar density distributions are consistent with the presence of preferential adsorption sites that are found close to each other at equilibrium. Indeed they are so close that when the shear is applied adsorbed water molecules slide from one adsorption site to another yielding well pronounced 'density bridges' that connect the various preferential adsorption sites, as described in Figure 3.6. On the contrary, because of the enhanced surface -water attraction attained when W=2, the planar density distribution at equilibrium shows well-defined preferential adsorption sites that are well separated from each other. When shear is applied the planar density distribution is essentially undistinguishable from the one obtained at equilibrium because the water molecules are so strongly bound to their respective adsorption sites that they cannot slide on the surface.

3.4   Conclusions

In conclusion, in this chapter I demonstrated, using molecular dynamics simulations, that slip and no-slip boundary conditions can both be observed for liquid water flowing on solid surfaces on which the static water contact angle is less than 90°. The responsible molecular signature appears to be the distribution of water

molecules within the contact layer at equilibrium, coupled with the strength of water-surface interactions. When preferential adsorption sites exist that are sufficiently close to each other that water migration from one to the next can occur without requiring hopping events, hydrodynamic liquid slip occurs. Because of computing-power limitations, the shear rates considered herein are high, but comparable to those found in high performance lubrication applications (e.g., rocket engines [65]). When verified experimentally my results could lead to the advancement of a variety of applications, including the design of hydrophilic nano-porous membranes with high permeation and self-cleaning hydrophilic surfaces. The desired surfaces should permit atomic-scale sliding of contact water molecules, which could be attained by providing a sufficient amount of preferential adsorption sites, by, e.g., atomic-scale etching, molecular grafting, or by integrating nanoparticles on a surface.

Chapter 4   The Role of Thin and Mobile Electric Double Layer in Water Purification and Energy Storage

4.1   Abstract

It is well known that the electric double layer plays important roles in a variety of applications, ranging from biology to materials sciences. Many studied the electric double layer using a variety of techniques, and as a result my understanding is mature, although not complete. Based on detailed understanding, I expect that by manipulating the electric double layer I could advance tremendously applications in the water-energy nexus. This is particularly true for electric double layer capacitors and capacitive desalination devices. However, such manipulation is not straightforward because of a competition of phenomena that occur within the electric double layer itself, including solvation effects, excluded volume phenomena, and ion-ion correlations. Using molecular dynamics simulations, I designed a composite graphene-based electrode to manipulate structural and dynamical properties of the electric double layer. My design favours the formation of the compact Helmholtz layer. Inherent to my design is that the compact Helmholtz layer not only is atomically thick, but it is also highly mobile in the direction parallel to the charged surface. I suggest here how to exploit the properties of the engineered electric double layer towards developing a new continuous desalination process that combines the advantages of membrane and capacitive desalination processes, reducing their

shortcomings. Insights on the molecular mechanisms relevant to the water-energy nexus are provided.

4.2 Introduction

Growing worldwide population, changes in weather pattern, and demand for improved standards of living all contribute to shortage of both fresh water and energy (the water-energy nexus). Securing abundant fresh water and energy in economical yet environmentally friendly manners is indeed one of the critical challenges my society faces [100, 101]. A combination of water desalination technologies and renewable energy sources will most likely be needed to win such challenge. Capacitive desalination (CD) promises to purify large amounts of salty water with low energetic consumption [102]. Energy storage devices, e.g., water-based electric double layer capacitors (EDLCs), are needed to deploy renewable energy sources at the large scale [103]. The performance of both CD and EDLC devices relies on the properties of the electric double layer (EDL) formed near carbon-based electrodes.

Back in 1853, Helmholtz was the first to propose the concept of the compact EDL [104], suggesting that the excess surface charge is compensated by counter-ions closely packed near the surface. Although the Helmholtz EDL, with thickness comparable to the radius of solvated ions [105, 106], was observed in solutions of sufficiently high salt concentrations (>1M) [107, 108], the thermal motion of ions [108] yields the 'diffuse' EDL, as proposed by Gouy [109] and Chapman [110], in which the surface charge is balanced by a cloud of rather mobile counter-ions. The diffuse EDL extends to a thickness, the Debye length, that depends on salt concentration, with lower concentrations leading to larger thicknesses [111]. In many

cases the EDL resembles the 1924 Gouy-Chapman-Stern model [112], according to which some ions bind to the charged surface (i.e., the compact layer), and others remain in its vicinity (i.e., the diffuse layer).

The EDL is important in the water-energy nexus because both CD and EDLCs function by accumulating and then releasing ions near charged surfaces and/or pores. In the EDLCs literature the accumulation of ions near the surface is quantified in terms of the electrodes capacitance, C. Borrowing the Gouy-Chapman-Stern model, C can be estimated as:

$$\frac{1}{C} = \frac{1}{C_H} + \frac{1}{C_D} \ .$$ (4.1)

In Eq. (4.1) C_H and C_D are the capacitance of the Helmholtz layer and that of the diffuse layer, respectively. Note that, based on Eq. (4.1), the smaller one out of C_H or C_D dominates C. In general, C_H is smaller than C_D, and therefore it is the dominant contribution to C [107, 113]. Increasing C_H, and hence C, improves the EDLCs' energy density. In CD, because it is desired to balance the excess surface charge by counter-ions within a compact layer, augmenting the compact EDL yields the highest charge efficiency [114]. Under optimal conditions, one charge unit on the electrode removes one ion from a 1-1 (NaCl) electrolyte solution [115]. Unfortunately, in carbon-based electrodes the EDL tends to be diffuse, unless narrow pores are used to remove the solvation shell from the ions [116, 117]. Promoting the formation of the compact EDL in carbon-based electrodes has therefore the potential of positively impacting both EDLC and CD devices.

I introduce here a graphene-based composite electrode that promotes the formation of the atomically thick Helmholtz layer at conditions at which the diffuse layer would be expected. More importantly, in my design the compact layer, not mobile in conventional electrodes, can slip in the direction parallel to the charged surface. My equilibrium and non-equilibrium molecular dynamics (MD) simulation results suggest promising performance indicators towards advancements in water desalination and energy storage devices.

4.3 Simulation details

I considered two electrochemical cells consisting of an electrode pair in contact with an aqueous NaCl solution of salinity $\alpha \sim 5.45$g/l (0.093mol/l) at 300K. In the first cell ('bare electrode', Figure 4.1A), two oppositely charged graphitic layers face across the aqueous solution. This configuration has been studied extensively [118-120]. In the second cell ('composite electrode', Figure 4.1B) the configuration is similar to that of the bare electrode, except one neutral graphene membrane is placed in front of each charged graphitic electrode, at a distance of 0.7nm. In each of these graphene membranes I carved two holes, each of diameter D=10Å (Figure 4.1C) by removing the necessary carbon atoms from the graphene sheet. The holes allow both ions and water to exchange between the 'side pore', near the graphitic charged surface, and the solution at the centre of the cell. I show herein that the graphene membranes effectively modify the structure of the EDL, yielding the unexpected performance in my design.

As a first approximation, the effect of different functional groups bound to the holes is not quantified here, although it is known to have a strong effect in graphene-based membranes [35, 121]. Experimentally, graphene membranes can be produced by

several methods including chemical vapour deposition [122], graphene irradiation with a focused electron beam [123], and ultraviolet-induced oxidative etching [124]. The practical arrangement of the graphene membranes near graphitic electrodes requires mechanical aids to prevent the graphene membranes from collapsing on the graphitic electrodes. This collapse would be driven primarily by van der Waals interactions between the graphene layers, and by the tendency of water to evaporate from the region between two hydrophobic surfaces [125]. Methods similar to the one recently proposed by Huang et al. [126] could help solve this design issue. Firstly, they dissolved negatively charged graphene oxide (GO) sheets with positively charged copper hydroxide nanostrands (CHN). Because of the electrostatic interaction the CHN incorporated into GO layers to form the GO/CHN composite membrane. CHN is then removed to obtain GO laminate membranes with a narrow size distribution (3–5 nm) and superior separation performance. Further reduction of GO membrane to graphene membrane is required to obtain the pore structure depicted in my model.

To simulate the electrodes, I assign the same partial charge on all carbon atoms (i.e., I impose a constant surface charge density on each electrode). Merlet et al. [127, 128] showed that it is possible to conduct simulations similar to those discussed herein by imposing a constant potential across the cell. These authors found that the distribution of electrolytes at the solid/liquid interface is strongly dependent on the algorithm implemented at high surface charge density (i.e., $1.00e/nm^2$). At the rather low surface charge densities considered here ($0.26e/nm^2$ or less), the results are not expected to depend strongly on the algorithm implemented (i.e., constant charge density vs. constant potential).
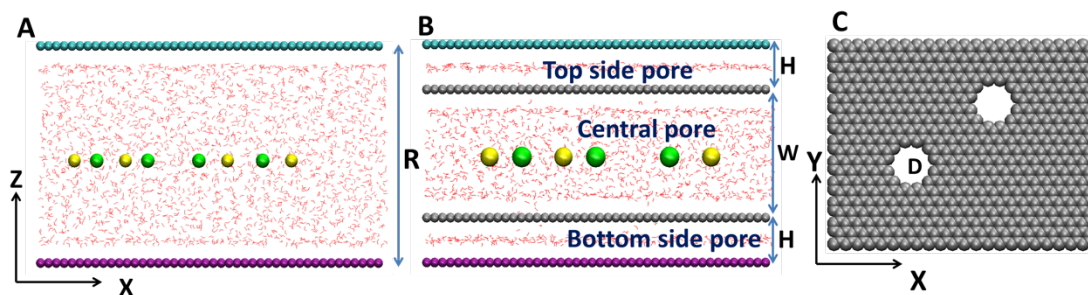
Figure 4.1 Schematic representations of the simulated electrochemical cells. In the bare cell (**A**), the negatively charged (purple) and positively charged (cyan) graphitic electrodes face across the slit pore of width R=34Å. In the composite cell (**B**), four graphene sheets are stacked vertically to create three slit-shaped pores: one central pore of width W=20Å and two side-pores (top and bottom), each of width H=7Å. The two outermost graphene sheets are charged positively (cyan) and negatively (purple), as in the bare cell, while the two inner graphene sheets (grey) are not charged. These graphene layers contain two holes each, both of diameter D=10Å (**C**). These graphene sheets act as membranes. In both bare and composite cells the area in the XY plane is 5.4x4.2nm^2. The simulations are conducted at two surface charge densities σ = 3.2μC/cm^2 and σ = 4.2μC/cm^2, in an effort to replicate realistic experimental conditions. All simulations are initiated by distributing water molecules (shown in red according to the wireframe convention) uniformly throughout the system. The desired number of Na$^+$ (yellow) and Cl$^-$ (green) ions are placed within the pore center. The simulated systems are electrically neutral. All simulations are conducted at 300 K.

Because I imposed periodic boundary conditions in all directions, the graphene electrodes are infinitely long along the X and Y directions (see Figure 4.1 for a schematic). Along the Z direction a large vacuum volume was added above and below the charged graphene layers to minimize undesired interactions between the periodic replicas of my system, which could be caused by long-range electrostatic interactions [129]. All the graphene surfaces were kept rigid and simulated by the force field proposed by Cheng and Steele [130]. The simulated bare cells contained 1764 water molecules and 3 ion pairs, while the composite cells contained 2268 water molecules and 4 ion pairs. These compositions yield the salinity α~5.45g/l

(0.093mol/l), which is consistent with that usually employed in capacitive desalination [115].

Many water models are available in the literature. In Appendix A, I compared the predictions obtained by simulating different water models on graphene [131]. I found that the structure of interfacial water predicted implementing SPC/E, TIP4P/2005, SPC/Fw, TIP4P/2005f and SWM4_DP water models is rather similar on neutral, negatively, or positively charged graphene. In this work, water is simulated by implementing the SPC/E model [45]. NaCl ions are modeled by the force field proposed by Dang [132], without considering polarization effects. Some studies suggest that polarization effects might impact water and ions properties at interfaces [133-135]. These effects are not investigated in details in this chapter because, based on my analysis (see Appendix B) [134], they should not significantly affect the results presented. In all systems considered here, the temperature is kept constant at 300K, using the Nose-Hoover algorithm. The equations of motion are integrated using the GROMACS simulation package, version 4.0.7, with the time step of 1fs.

Both equilibrium and non-equilibrium simulations were conducted. I conducted my equilibrium all-atom simulations in the NVT ensemble. The simulated systems are equilibrated for 100ns. Equilibration is considered achieved when the number of ions confined within the side pores remains constant over 50ns. The results obtained during the last 50ns of the equilibrium simulations are used to compute the averages reported herein.

Non-equilibrium simulations were conducted to study the flow of electrolyte solutions inside the electrochemical cells. In these non-equilibrium simulations all water molecules and NaCl ions are forced to move along the X direction with

constant applied acceleration 2.4×10^{13}m/s^2 (mimicking, e.g., a gravity-driven flow) [15, 28, 136]. In these simulations, because the periodic boundary conditions are applied in the direction of flow, the water and ions that exit the simulation box because of the imposed flow enter the pore from the opposite end of the electrode, thus maintaining a constant number of molecules within the simulation cell. Because of the periodic boundary conditions, the simulations do not account for phenomena that would be encountered when water and ions enter or exit the electrodes. The non-equilibrium simulations are conducted until the velocities of water and ions in the X direction remain constant over a period of 100ns (i.e., steady states are achieved). Instead of applying acceleration of 2.4×10^{13}m/s^2 to all molecules, an equivalent pressure of 100MPa can be imposed to drive the flow inside the pores. The large value of the acceleration applied in my simulations, clearly non realistic, is due to computing power limitations [13, 21]. However, because it has been reported that the time scale for fluid flow scales linearly with the applied acceleration [27, 35], and because fast water transport through graphitic nanopores and carbon nanotubes under small applied pressures was experimentally observed [60, 70], I expect that small applied pressures can drive the flow through the proposed desalination cell following mechanisms analogous to those discussed below.

4.4   Results and discussions

I first investigated how the electrode design affects the EDL in the two electrochemical cells. The surface charge density applied on both electrochemical cells is $\sigma = 3.2\mu$C/cm^2. Visual inspection of the simulation snapshots obtained once equilibration is achieved (Figure 4.2A and Figure 4.2B) reveals that the graphene membranes strongly affect the distribution of the ions. The counter-ions accumulate

near the oppositely charged surface in both electrodes, but yielding diffuse EDLs in the bare cell and compact EDLs in the composite cell. The thickness of EDL can be quantified from the charge density profiles of NaCl shown in Figure 4.2C. Within the bare cell (black line) the thickness (i.e., the distance between the electrode and the end of EDL) of the diffuse EDLs near the negative and positive electrodes are ~13.75Å and 14.25Å, respectively. In contrast, within the composite cell (red line) the thickness of the compact layers near the negative and positive electrodes are 4.75Å and 5.25Å, respectively. These data indicate the formation of compact layers at conditions at which diffuse layers are expected.

Because of the presence of the graphene membranes, when the ions migrate from the central pore to the side pores they remain trapped within the side pores instead of returning to the central pore consequently to thermal motion (as observed in the bare cell, see Figure 4.3A). The ability of the graphene membranes to keep the ions within the side pores is a crucial feature of my design. If the membrane holes diameter D is too large, the ions can easily diffuse back from the side pores to the central pore (Figure 4.3B). As a side note, I point out that, because of confinement effects, there are 6 and 4 water molecules in the first hydration shell of Cl^- and Na^+ ions, respectively, as opposed to 7 and 6 in bulk aqueous solutions [121, 137]. Clearly, the water molecules in the first hydration shells rearrange in a plane parallel to the pore surfaces (Figure 4.3C). Because of this re-arrangement, the EDL thickness found in my composite cell is not only much smaller than that of the diffuse layer but also smaller than the thickness of a typical Helmholtz EDL in which the ions remain hydrated [105, 106].
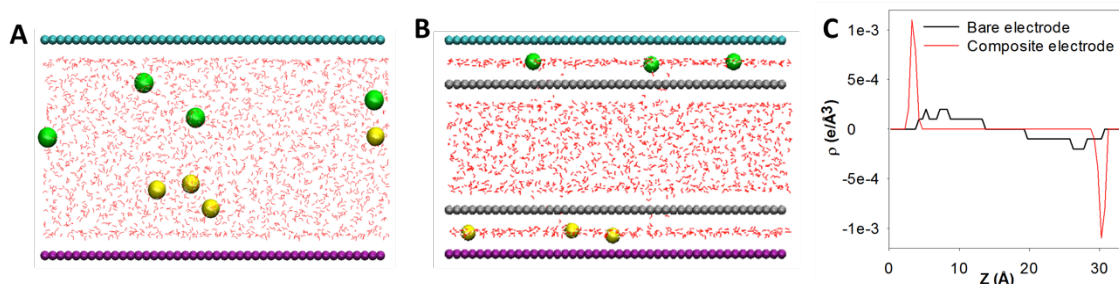
Figure 4.2 Representative simulation snapshots at equilibrium for the bare (A) and composite (B) electrochemical cells. These simulations are conducted at the surface charge density $\sigma = 3.2\mu C/cm^2$. The colour code is the same as that of Figure 4.1. Note that while in the bare cell the ions distribute throughout the entire pore, with counter-ions accumulating near the charged surfaces, in the composite cell the ions are not present within the central pore. Instead they accumulate within the side pores, with Na^+ ions near the negatively charged surface, and Cl^- ions near the positively charged one. Charge density profiles obtained at equilibrium for bare (black) and composite (red) cells (C). The density distributions are consistent with the formation of diffuse EDLs in the bare cell, as expected at the low salinity and low charge density considered in these simulations. In contrast, the high intensity and narrow peaks observed in the composite cell indicate the formation of compact layers centred at 3.5Å and 3.75Å near negatively and positively charged electrodes, respectively.
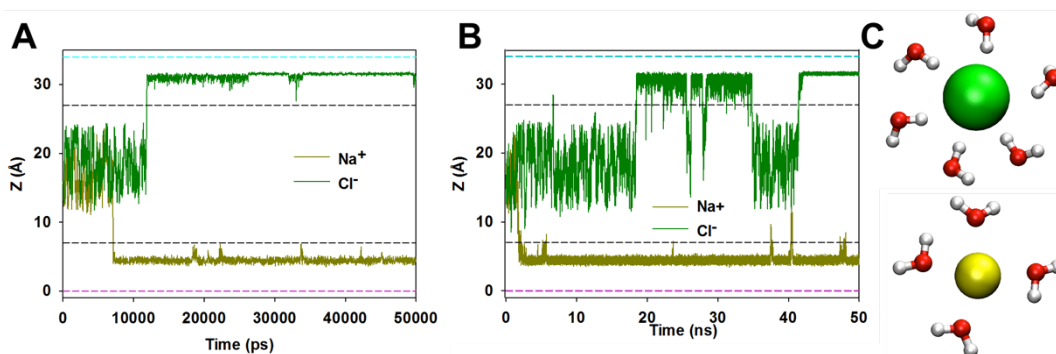
Figure 4.3 Z coordinates of representative Na^+ and Cl^- ions obtained during equilibrium simulations conducted within the composite cell as a function of time when the hole diameter D=10Å (A) and D=15Å (B). The results show that in the case of D=10Å, when the ions migrate from the central pore to the side pores (within ~ 2ns in the case of Na^+, and ~10ns in the case of Cl^-), they remain trapped within the side pores for long times. On the contrary, when D=15Å the ions can frequently move between side and central pores. Hydration shells structure of Cl^- and Na^+ (C) ions within the side-pore of composite cell.

The latter observation has an important practical consequence as reducing the Helmholtz layer thickness enhances the electrode capacitance ($C = \frac{\varepsilon A}{d}$ [113, 116], where A, d, and ε are surface area, Helmholtz layer thickness, and dielectric constant, respectively). From the charge density profiles I integrate twice (see Appendix C) the Poisson equation [111, 120] $\frac{d^2\psi(z)}{dz^2} = -\frac{\rho(z)}{\varepsilon_0}$ (ε_0, $\psi(z)$, and $\rho(z)$ are vacuum permittivity, electrical potential, and charge density, respectively) to extract the electrical potential profiles near the charged surfaces (Figure 4.4). To conduct this integration I require two boundary conditions. As first condition, I impose that the electric field in correspondence to the center of the pore is zero ($\frac{d\psi}{dz} = 0$ at $z = R/2$, where R is the pore width). The physical reason underpinning this boundary condition is that at the pore center the electric field emitted from the negative electrode neutralizes the one emitted from the positive electrode. As the second boundary condition, I impose that the electrical potential is zero at z = 0. This condition is arbitrary, and it will not affect the potential difference across the EDL. The electrical potential profiles I obtain allow us to calculate the capacitance using the equation $C = \frac{\sigma}{\psi}$, where σ is the surface charge density and ψ is the potential drop across each EDL (see Table 4.1).

The capacitance predicted for the composite electrode is much larger than that predicted for the bare electrode, as expected due to the change in the EDL thickness. It is perhaps more important to point out that the capacitance predicted for the composite electrode considered in my simulations is ~70-80% those reported for electrochemical cells that employ ionic liquids [119, 138, 139].
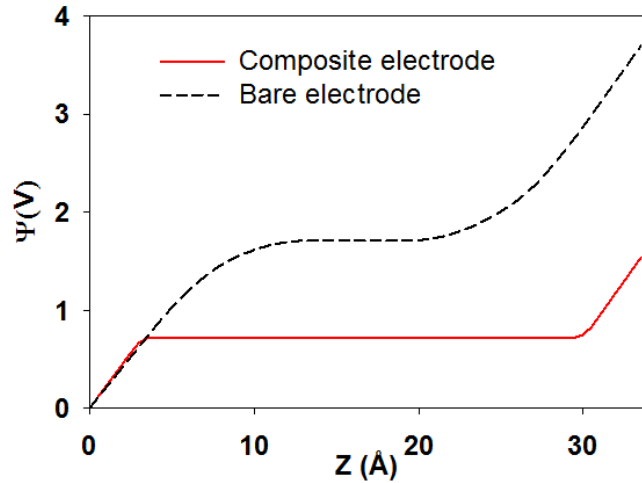
Figure 4.4 Electrical potential profiles as a function of distance Z between two electrodes. The potential drop across the EDL is the difference between the potential found at the interface and that determined at the end of the EDL. These results are obtained by integrating the charge density profiles twice using the Poisson equation following the procedure described in the Appendix C.

Table 4.1 EDL thickness, potential drop across the EDL (up to the EDL thickness), and capacitance obtained for bare and composite electrodes.

	Negatively-charged electrode			Positively-charged electrode		
	d_{EDL} (Å)	Potential drop (V)	Capacitance $\mu F/cm^2$	d_{EDL} (Å)	Potential drop (V)	Capacitance $\mu F/cm^2$
Composite	4.75	0.72	4.44	5.25	0.81	3.95
Bare	13.75	1.71	1.87	14.25	1.99	1.60

To study the effect of the salinity on the performance of the composite cell, I provide in Figure 4.5 the number of NaCl pairs accumulated within the side-pores as a function of the total number of NaCl pairs initially present in the salty water. These equilibrium simulations were conducted at surface charge density of $3.2\mu C/cm^2$. The results show that when 3 or less ion pairs are present ($\alpha \leq 5.45g/l$), they can all be extracted into the side-pores. When more ion pairs are present (up to $\alpha=29.07g/l \sim$ sea salinity), only 3 are extracted from the salty water, while the others remain inside

the central pore. This indicate that increasing the system salinity above 5.45g/l does not affect the number of ions in the side pores, and hence the capacitance of the Helmholtz EDL.
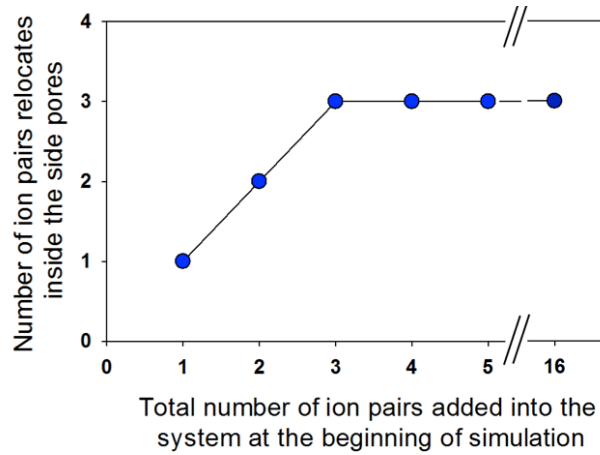
Figure 4.5 Number of NaCl pairs accumulated within the side-pores as a function of the total number of NaCl pairs initially present in the salty water.

In Figure 4.6 I compare the results obtained from the simulations of the composite cell when the side-pore width H is 7Å and 10Å. In these simulations, the surface charge density is $\sigma = 4.2\mu C/cm^2$ and salinity is α~9g/l. Visual inspection of the simulation snapshot (panel A and B) indicates that when H=10Å there is two water layers inside the side-pore. As a results the Helmholtz EDL thickness near the negatively charged electrode (panel C) increases from $d_{Helmholtz}$=4.25Å when H=7Å (red line) to $d_{Helmholtz}$=6.75Å when H=10Å (black line) (see Table 4.2 for more details on $d_{Helmholtz}$ near positively charged electrode). Because the EDL thickness increases the capacitance of the composite electrodes decreases.
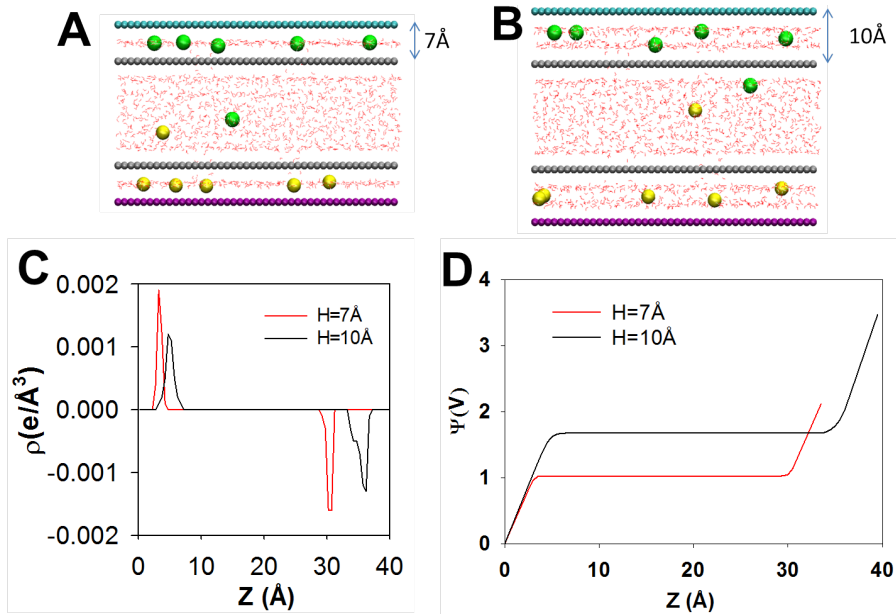
Figure 4.6 The effect of side-pore size H on the capacitance of the composite electrode. Representative simulation snapshots at equilibrium for side-pore size H=7Å (panel **A**) and H=10Å (panel **B**). The colour code is the same as that used in Figure 4.1. Charge density profiles (panel **C**) obtained at equilibrium for the composite electrochemical cells in which the side-pore size H=7Å (red) and H=10Å (black). Electrical potential profiles (panel **D**) across the composite electrode when H=7Å (red) and H=10Å (black). See Table 4.2 for thickness, potential drops, and capacitance of EDLs.

Table 4.2 Thickness, potential drop, and capacitance estimated for composite electrodes with side-pore size H=7Å and H=10Å. The correspondent simulation results are summarized in Figure 4.6

	Negatively charged electrode			Positively charged electrode		
	$d_{Helmholtz}$	Potential drop	Capacitance	$d_{Helmholtz}$	Potential drop	Capacitance
H=7Å	4.25Å	1V	4.2μF/cm^2	5.25Å	1.1V	3.8μF/cm^2
H=10Å	6.75Å	1.67V	2.5μF/cm^2	7.25Å	1.73V	2.4μF/cm^2

The compact EDL described in Figure 4.2B (composite electrode) is not only atomically thick, but it also slips in the direction of flow parallel to the electrodes (Figure 4.7A), as suggested by my non-equilibrium simulations. These simulations

are initiated either from the last configuration obtained from the equilibrium simulations (i.e., the ions are inside the side pores, Figure 4.2B) or from the configuration where the ions are inside the central pore (Figure 4.1B). The results obtained from these different initial configurations do not differ from each other. The non-equilibrium simulations are conducted until the ions relocate inside the side pores and steady-states flow is achieved, as described in the 4.3 section. The results presented in Figure 4.7A indicate that in the side pores the velocity of water molecules is nonzero (thus consistent with hydrodynamic slip), and it undistinguishable from the velocity of the ions (suggesting that the ions move with water). The velocity of Na^+ ions is larger than that of Cl^- ions because of steric effects within the narrow side pores considered in my design. In the centre of the device water molecules flow with higher velocity than in the side pores because the pore is wider, as expected. The hydrodynamic slip observed both in the side pores and within the central pore is consistent with prior experimental and modelling observations [27, 60, 68-70]. My results suggest that the slippage of the compact EDLs observed within the composite cell can tremendously improve the operation of CD devices because CD is based on the physical adsorption of ions onto charged porous electrodes. In both flow-by [102, 115] and flow-through [140] processes when salty water is exposed to a pair of fresh electrodes the counter-ions adsorb onto the charged electrodes, and fresh water is produced. However, because once the ions enter the electrodes they remain trapped there, regeneration is necessary [102, 115, 140], and the process is not continuous, unless complex operations are designed (e.g., desalination with wires) [141]. As opposed to existing technologies, the composite cell I propose promises the possibility of continuous operation, because

there is no need of electrodes regeneration (Figure 4.7B). I christened my designed '*continuous electrode-membrane desalination cell*'.
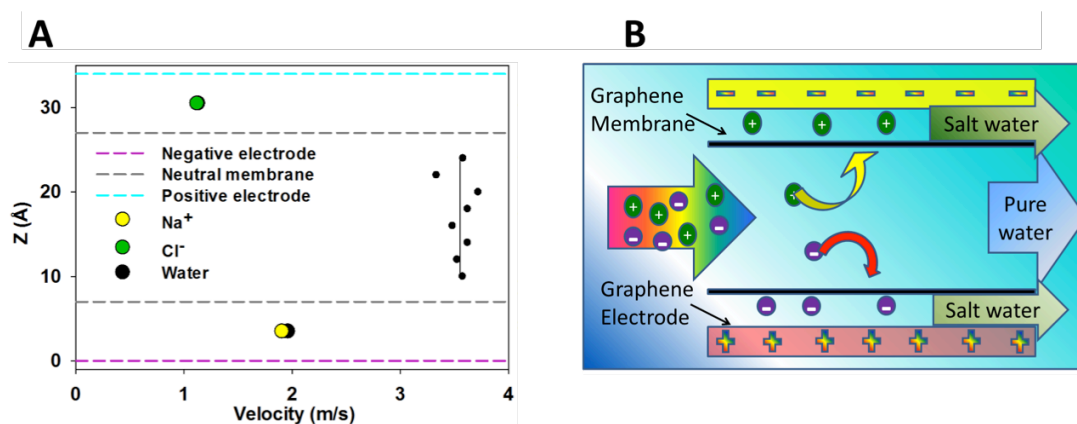
Figure 4.7 Velocity of water molecules, Na$^+$ and Cl$^-$ ions inside the composite electrode cell (A) as obtained from Poiseuille flow simulations. The water flows with the velocity of ~ 3.5m/s within the central pore. In the bottom side-pore, water and Na$^+$ ions flow with the velocity of 1.9m/s. In the top side-pore, water and Cl$^-$ ions flow with the velocity of 1.2m/s. Despite these differences in flow velocities, all the electrolyte solutions slip inside all of the pores in the composite cell, promising continuous CD operation (B).

The *continuous electrode-membrane desalination cell* I envision is operated as follows: the salty water is fed continuously into the central pore (note that in my non-equilibrium simulations, because of periodic boundary conditions, salty water cannot be fed to the system); during operation the ions diffuse from the central pore to the side pores because of the applied voltages. Compared to existing CD devices [142], the envisioned cell has the advantage that the two neutral graphene membranes provide a physical barrier to separate purified from salty water (central and side pores, respectively). Because the compact Helmholtz EDL can slip inside the side pores, and the water in the central pore can flow smoothly through the device, both fresh and salty water can be continually withdrawn from the device. I reiterate that

the operation enabled by the proposed design differs substantially compared to flow-through, flow-by, and desalination-with-wires CD devices in which the ions, once trapped, remain immobilized inside the porous electrodes [115]. I estimate water permeability (30L/cm^2/day/MPa, under the assumption that 10% of the cross surface area of an hypothetical membrane that embeds the proposed cell is constituted by pores) much larger than that obtained from current membrane-based water desalination techniques [143]. At optimum conditions (surface charge density σ = =+/-4.2μC/cm^2 and salinity < 10.9g/l) the proposed desalination cell can capture all salty ions within the side pores (100% rejection), recover 70% of the salty water initially fed to the system, and yield a charge efficiency of 83%. Higher charge efficiency, pershaps 100% can be obtained at higher salinity using larger pores (Figure 4.8). Note that 100% charge efficiency has been reported in the literature [115]. Operating the cell will require energy for applying voltages on the electrodes and pumping the salty water through the cell. Because fast water transport through graphitic nanopores and carbon nanotubes under small applied pressures was experimentally observed [60, 70], because it has been reported that CD of brackish water consumes much less energy than reverse osmosis does [102, 144, 145], and because high charge efficiency can be obtained in the engineered cell I propose, I expect the proposed cell to be competitive against existing processes. Unfortunately, quantification of operational costs cannot be conducted reliably at this stage.
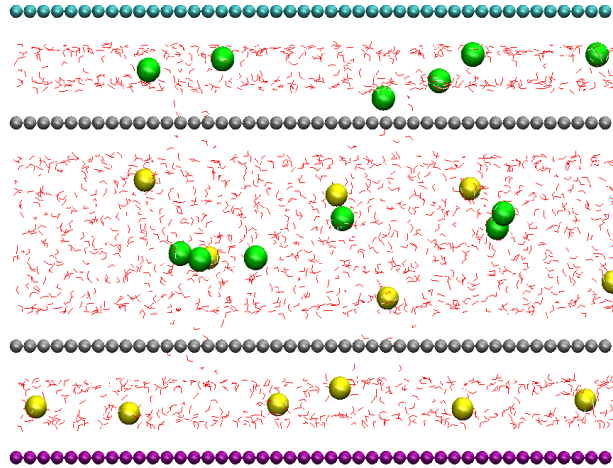
Figure 4.8 Representative simulation snapshot at equilibrium for the composite electrochemical cells in which the side-pore size is H=10Å, salinity 18g/l, and surface charge density μ =+/-4.2μC/cm^2 [6e/(5.4x4.2nm^2)]. There are 6 ion pairs extracted to the side-pores. Unity charge efficiency is obtained: 6 charge units on each electrode extract 6 monovalent ions from NaCl solution.

4.5   Conclusions

To conclude, I managed to alter the structure of the electric double layer formed within graphitic electrochemical cells. This was achieved by inserting graphene membranes near charged graphitic electrodes. I demonstrated that the ability of manipulating the electric double layer has important implications for the water-energy nexus, as it allows us to both effectively and efficiently store energy and purify water. The compact Helmholtz layer found in the envisioned composite electrochemical cell is not only atomically thick, but it is also able to slip in the direction parallel to the electrodes. The formation of the compact electric double layer significantly enhances the electrodes capacitance, with important implications for the design of electric double layer capacitors. It cannot be overstated that the slippage of the Helmholtz layer is important for the practical realization of the *continuous electrode-membrane desalination cells*. Based on my simulation results,

66

the proposed desalination cell can be operated continuously, achieving up to 100% charge efficiency, recovering 70% of the water initially loaded to the system with 100% salt rejection at salinity < 10g/l, and yielding high water permeability (30L/cm^2/day/MPa).

Supplemental Information

Details on the molecular dynamics simulation of different water models on graphene surfaces are presented in Appendix A. The polarizability effects in molecular dynamics simulations of graphene/water interface are reported in Appendix B. In Appendix C, details regarding the integration of the Poisson are reported.

Chapter 5   Water and Methane in Shale Rocks: Flow Pattern Effects on Fluid Transport and Pore Structure

5.1   Abstract

Using molecular dynamics simulation I study the two-phase flow of water and methane through slit-shaped nano-pores carved from muscovite. The simulations are designed to investigate the effect of flow patterns on the fluids transport and on the pore structure. The results indicate that the movement of methane with respect to that of water changes when the flow pattern is altered. This can happen when the driving force, i.e., the pressure drop, increases above a pore-size dependent threshold. My results illustrate the importance of the capillary force, due to the formation of water bridges across the clay pores, not only on the fluid flow, but also on the pore structure, in particular its width. When the water bridges are broken, perhaps because of fast fluid flow, the capillary force vanishes leading to significant pore expansion. Because muscovite is a model for illite, a clay often found in shale rocks, these results advance my understanding regarding the mechanism of water and gas transport in tight shale gas formations.

5.2   Introduction

In just a few decades, shale gas has become one of the most important energy resources for the USA, with significant contributions to the natural gas production in the country [146]. The economical success related to shale gas production has generated interest worldwide, and research has been initiated in many countries to explore the vast shale formations present throughout the world.

Research is needed because shale formations are characterized by small porosity, compared to, e.g., sandstone formations, composed of pores with size ranging from 1 to 200nm [147]. Because of these features, the permeability of shale rocks can be as low as 1 - 100 nanodarcy, (for comparison, the permeability of sandstone is of the order of 1-10 millidarcy). Hydraulic fracturing is practiced to increase the extremely low permeability of shale rocks to enable the economic production of gas, and sometimes oil [148]. Because water can both be injected and be present naturally in some shale formations, one complicating characteristic is that water and natural gas can co-exist within the pores, leading to the possibility that two-phase flow occurs through the extremely narrow pores of shale formations [149]. The interactions between water, gas, and shale rocks within such tight environment can lead to capillary forces and surface phenomena. Understanding these interactions and how they affect the fluid transport is crucial to design effective stimulation practices and optimal gas production strategies, as well as for reducing the environmental impact of shale gas [148, 150]. Building on the results obtained by those scientists devoted to study the behaviour of fluids in narrow pores (i.e., the adsorption community), it is my goal to better understand the mechanism of fluid migration, in particular when two phases form, through shale formations using various modelling approaches.

Two-phase flow is a common problem encountered in many practical applications in chemical engineering, oil recovery, food industry, and bio-technologies [151]. Although much is known about two-phase flow in macro- and

micro-scale channels [152], little is known about it in nanochannels due to the technical difficulty in fabricating and manipulating nano-devices, in measuring the flow rate in such systems, and in visualizing the flow patterns [153]. As mentioned above, it is expected that the two-phase flow in nanochannels will differ compared to that in wider channels because capillary and surface forces could generate unexpected effects.

Darcy's law is often used to describe macroscopically the fluid flow through a porous material: $Q = -\frac{kA}{\eta}\frac{dP}{dx}$, where Q is the flow rate, A is the cross-sectional area, η is the viscosity of the fluid, k is the permeability, and $\frac{dP}{dx}$ is the pressure drop [154]. According to Darcy's law, the flow rate is linearly proportional to the driving force (i.e., the pressure drop). When two phases are present, the flow rate of each phase is linearly proportional to the driving force [155] only if one phase does not interfere with the flow of the other [156]. In this case, one phase effectively reduces the pore area available for the flow of the other. However, when fluid transport occurs in nano-pores, the enhanced complexity due to the combination of the interactions between the fluids, the significance of viscous and capillary forces, and the pore morphology might cause Darcy's law to no longer provide accurate predictions of fluid flow [155, 157, 158]. Some of these effects, in particular the flow pattern of two-phase flow and its dependence on the pore morphology, have been studied extensively in micro- and macro-channels [152, 159, 160]. Similar studies are prohibitive at the nanoscale because of multiple technical challenges [153]. Recently, Wu et al. [149, 153] used optical

imaging to study single and two-phase pressure-driven flows in silicon nitride nanochannels of width 100nm. They concluded that the linear correlation between flow rate and pressure drop was upheld for single-phase flow, and they reported three different flow patterns including single, annular, and stratified for two-phase flow. Perhaps molecular modelling can help better understanding the two-phase flow mechanism in nanochannels.

In this work I employ molecular dynamics simulations to study the flow of water and methane inside slit-shaped nanochannels obtained from muscovite. Muscovite is a popular substrate because of its perfect cleavage, which allows the creation of large surfaces that are atomically smooth [161]. I chose muscovite because it has similar structure to illite [162], a common clay in sedimentary rock environments, including the shale formations [163] found in the Marcellus and Barnett regions [164, 165].

In the remainder of this chapter I first present details regarding the model substrate and the algorithms implemented for my simulations, I then discuss the results and how they are pertinent to (i) the two-phase flow in narrow pores and (ii) the pore deformation due to fluid flow and imposed pressure. Finally, I summarize the results.

5.3   Simulation details

In Figure 5.1 I report a schematic representation of one of my simulated systems. For all simulations, 1800 water and 600 methane molecules are placed inside the slit-shape pore obtained from muscovite. Muscovite is a phyllosilicate mineral

[166, 167] with TOT structure: an Al-centred octahedral sheet is sandwiched between two Si-centred tetrahedral sheets, in which one Al atom substitutes one out of every four Si atoms. An interlayer of potassium ions balances the negative charge due to the Al substitution. The potassium interlayer holds the TOT layers together by electrostatic interactions [168]. In my model, the muscovite substrate spans 6.2nm along the X, 5.5nm along the Y, and 1.96nm along the Z directions. The atoms in the muscovite mineral, water, and methane are simulated by implementing the CLAYFF [89], SPC/E [45], and TraPPE [169] force fields, respectively. In all cases, the temperature is kept constant at 300K. The pore-pressure is either 75MPa or 250MPa, conditions usually implemented in laboratory studies for rock permeability using the triaxial-test method [170, 171].

Periodic boundary conditions are applied in all directions for all simulations. Therefore, the muscovite substrate is infinitely long in X and Y directions. Following the methods implemented in my prior studies, in the Z direction a large vacuum volume is added above the muscovite layer to minimize unphysical effects due to interactions between periodic images of the simulated system [172]. The equations of motion are integrated using the GROMACS simulation package, version 4.0.7, with the time step of 1fs.

Pore-pressure control

To obtain the desired pore-pressure, I apply a force along the Z direction onto the top surface. The pore pressure is calculated dividing the applied force by the XY simulation box area. Both muscovite surfaces are described as rigid bodies. The

top surface is kept rigid in X and Y directions, but is free to move along the Z direction. The bottom surface is kept rigid (see Figure 5.1). I start from an initial configuration in which the pore size is 5nm (shown in Figure 5.1). I apply a force F_1 as necessary to apply 250MPa to the pore. During this simulation the pore shrinks from 5nm to 2.65nm.

To prepare the 75MPa pore system I follow two simulation protocols. In the first protocol, the 'compression' protocol, I start from the initial configuration in which the pore width is 5nm (system of Figure 5.1) and apply a force F_2 ($F_2 < F_1$) onto the top surface. As the simulation progresses, the pore shrinks to a width, discussed later, that is wider than the 2.65nm achieved for the 250MPa pore-pressure system. In the second protocol, the 'expansion' protocol, I use as initial configuration the system of width 2.65nm (the 250MPa pore-pressure system) and I reduce the applied pressure from F_1 to F_2. As the applied pressure is reduced, the pore widens. All of the pore-pressure simulations are conducted for 30ns. A constant pore size is usually obtained after 6ns.
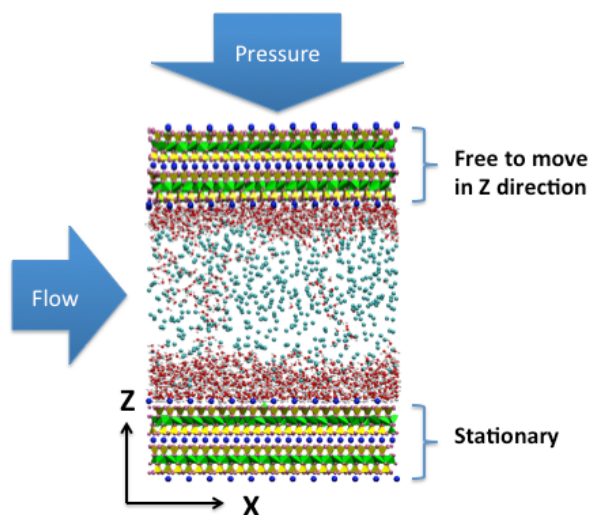
Figure 5.1 Schematic representation of the initial configuration of my simulated systems. Water (red and white spheres) and methane (cyan spheres) are confined in a slit-shape muscovite nanopore. Al-centred octahedral, Si-centred tetrahedral, and potassium atoms are presented in green, yellow, and blue colour, respectively.

Poiseuille flow simulations

The two-phase flow inside the muscovite nanopore is studied by conducting Poiseuille flow simulations, using a non-equilibrium approach. These simulations are initiated from the final configurations of the pore-pressure control simulations described above. The simulation conditions are the same as those applied above, i.e., the surfaces are treated as rigid bodies and I continue to apply the force along the Z direction, however, a constant acceleration is applied along the X direction of the simulation box, ranging from 0.02 to 0.08nm/ps^2, to all water and methane molecules within the pore. This method is widely used to study the fluid transport through infinite nanopore with periodicity, which is the condition of our model [173-175]. For non-periodic finite nanopore, fluid flow through the pore is driven

by reservoir pressure control [173, 176]. This system is usually applied to study the flow through membrane [176]. Two reservoirs (source and sink of water flow) are connected to the membrane. A force is applied on the moveable wall [176] or on the fluid within the user-defined region [173] to produce pressure drop between two reservoirs. If one applies the second approach the corresponding pressure drop across the pore should range approximately from 1.5×10^{16} Pa/m to 6×10^{16} Pa/m to reproduce my simulation condition. Although these applied accelerations are meant to mimic a pressure-driven flow [15, 28, 136], they are too high to be realistic; this is due to computing power limitations [13, 21]. The simulations are conducted until steady states (i.e., constant velocity profiles for the fluid inside the pore) are obtained. The Poiseuille flow simulations are conducted for 30ns. The steady state is usually obtained after 10ns.

5.4 Results and discussions

5.4.1 Pore-pressure 250MPa
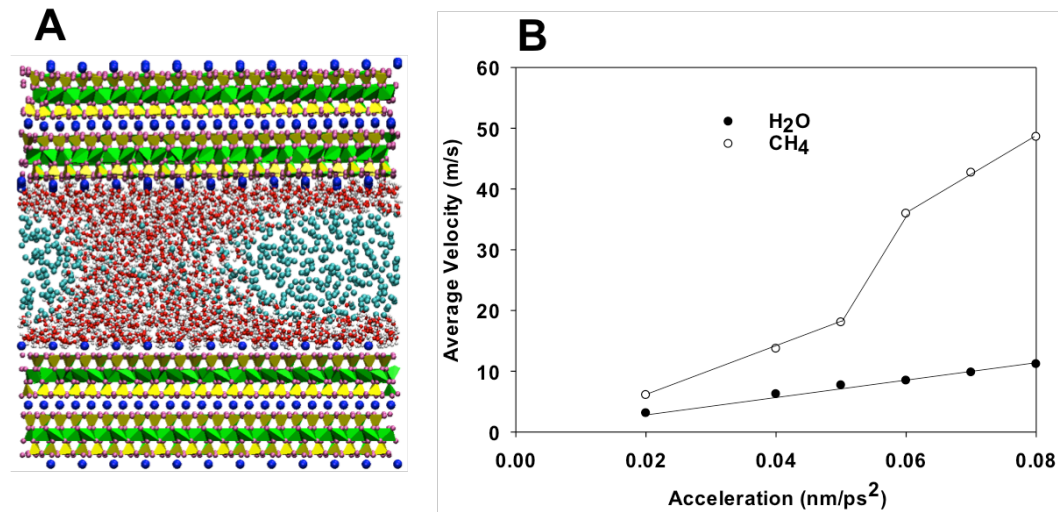
Figure 5.2 Simulation snapshot representing the final configuration of the 250MPa pore-pressure control simulation (A). Average velocity along the X direction of water (filled circles) and methane (empty circles) during the two-phase flow within the muscovite nano-pore as a function of the applied acceleration (B).

In Figure 5.2A I report a simulation snapshot representing the final configuration of the 250MPa pore-pressure control simulation. The simulation snapshot confirms that I are in the presence of a two-phase system. Visual inspection shows that water preferentially wets the muscovite surfaces and that a bridge of water molecules is formed between the two pore surfaces. Methane molecules form one gas bubble that is trapped within water. From this equilibrium configuration I initiate the flow simulations by applying a constant acceleration to the fluid molecules along the X direction. The average velocities of water (filled circles) and methane (empty circles) obtained at steady states as a function of the applied acceleration are presented in Figure 5.2B. The results indicate that the

average velocity of water increases linearly as the applied acceleration increases, which is consistent with Darcy's law, as the applied acceleration is the driving force for the flux of water. The results obtained for methane differ significantly from those just described for water. In particular, the average velocity for methane increases linearly when the acceleration increases from 0.02 to $0.05nm/ps^2$, and then again from 0.06 to $0.08nm/ps^2$. As the acceleration increase from 0.05 to $0.06nm/ps^2$, a step increase of the methane velocity is observed. It is also worth pointing out that, even though below $0.05nm/ps^2$ and above $0.06nm/ps^2$ the relationship between average velocity and applied acceleration is linear, the slopes of the lines differ, suggesting that the effective permeability of the pore is larger at higher applied accelerations. As I will show below, the results in Figure 5.2 suggest that the Darcy's law can be used to describe the two-phase flow in nanochannels only if there is no change in flow pattern. They also suggest, perhaps more importantly, that the permeability of the porous material depends strongly on the structure of the confined fluid, which can change upon changes in external stimuli, including applied pressure drops. Visualization of the flow patterns, presented in Figure 5.3, provides justification for these insights, in particular concerning the step increase of the velocity of methane when the acceleration increases from 0.05 to $0.06nm/ps^2$.
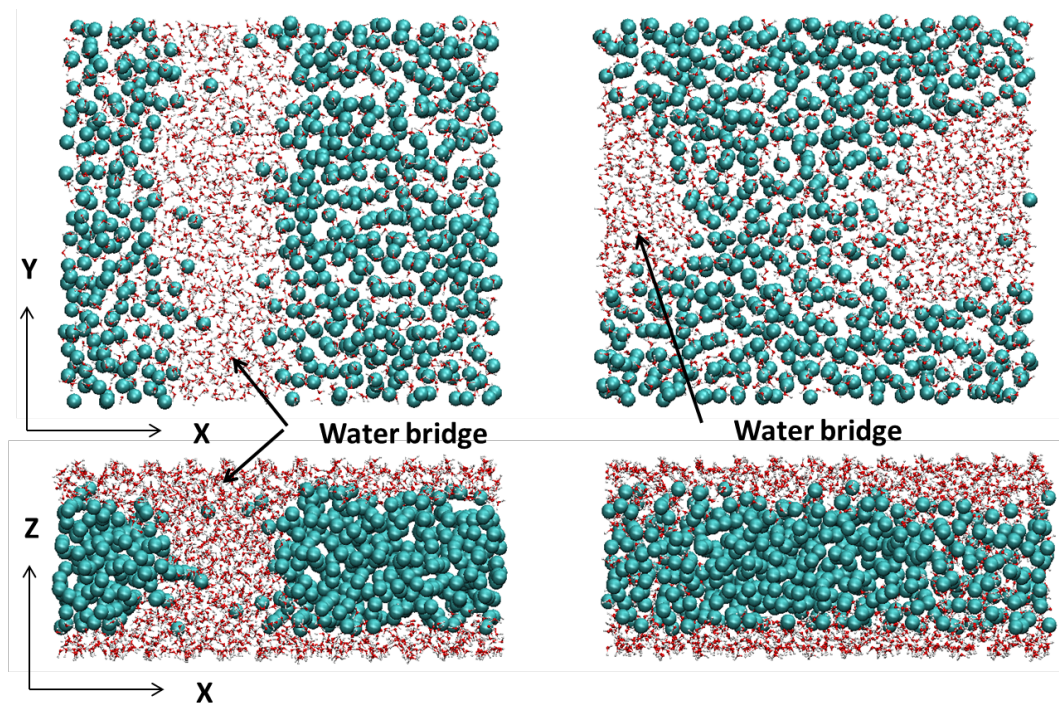
Figure 5.3 Top (top panels) and side (bottom panels) views of the flow patterns inside the pore of Figure 5.2 (surfaces are removed for clarity) when the applied acceleration is 0.05nm/ps^2 (left) and 0.06nm/ps^2 (right).

In Figure 5.3 I present the flow patterns inside the pore of Figure 5.2 when the applied acceleration is 0.05nm/ps^2 (left) and 0.06nm/ps^2 (right). In all cases, the flow occurs along the X direction, and the snapshots are obtained after steady states conditions are established. The results presented in the left panels show the water bridge, formed between the two surfaces, which spans the entire length of the pore along the Y direction. Further investigation is necessary to study the dependence of this structure on the length of the simulation box along the Y direction. This flow pattern is observed when the applied acceleration is 0.05nm/ps^2 or smaller. This pattern is consistent with the 'slug flow' observed for

two-phase flow at larger length scales when the gas phase exists as a large bubbles separated from each other by liquid 'slugs' [177].

When the acceleration increases to $0.06nm/ps^2$, the flow pattern changes, as shown in the right panels of Figure 5.3. The water bridge between the two surfaces is still present, but it no longer spans the entire length of the pore along the Y direction and resembles a water 'pillar' surrounded by methane. As a consequence, water molecules reduce the flow area available to methane, but they do not slow methane flow. The flow pattern just described does not change when the acceleration increases from 0.06 to $0.08nm/ps^2$. Because within the conditions of Figure 5.2 and Figure 5.3 when the flow pattern changes the pore size does not change, my results suggest that the step increase in the velocity of methane when the applied acceleration increases from 0.05 to $0.06nm/ps^2$ is due to the change in flow pattern just discussed. Within this range of conditions the flow of water continues to obey the Darcy's law. I also point out that the flow pattern change just discussed is irreversible. In other words, even if I reduce the applied acceleration from 0.06 to any value below $0.05nm/ps^2$, the flow pattern remains the one described in the right panels of Figure 5.3, and the one described on the left panels of the figure is not re-established. This is probably evidence of the possibility that long-lived metastable states can strongly affect two-phase fluid flow through nano-pores.
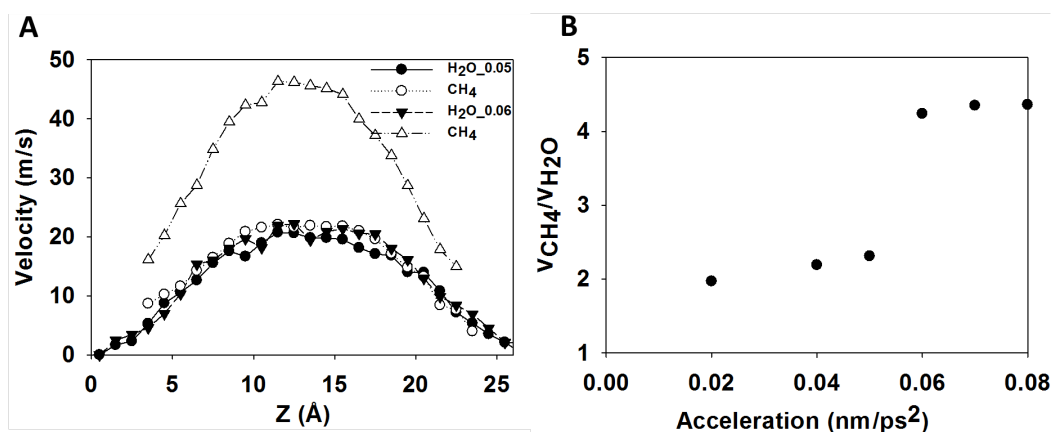
Figure 5.4 Velocity profiles of water (filled symbols) and methane (empty symbols) during the two-phase flow within muscovite pore when the applied accelerations are 0.05nm/ps^2 (circles) and 0.06nm/ps^2 (triangles) (A). Ratio between the average velocity of methane and that of water during the two-phase flow as a function of applied acceleration (B).

To better understand how the flow pattern affects the flow of water and methane through the slit-shaped muscovite nanopore I present in Figure 5.4A the velocity profiles of water (filled symbols) and methane (empty symbols) as a function of the position within the pore when the acceleration is 0.05nm/ps^2 (circles) and 0.06nm/ps^2 (triangles). At the acceleration of 0.05nm/ps^2 (circles) the velocity profiles of water and that of methane suggest that at the pore center methane travels at the same speed as water does (note that very few methane molecules are found near the surface). This suggests that, effectively, the water bridge (see Figure 4.3) blocks the methane transport in the direction of flow. At the higher applied accelerations, the results in Figure 5.4A show that, at every position within the pore methane travels much faster than water does. This happens because the water bridge no longer blocks methane transport, as it no longer

80

spans the entire width of the nano-pore. In this configuration methane molecules can move through the pore free from physical interactions with water. The effect of the change in flow pattern becomes more evident when I compare the average velocity of methane to that of water inside the pore (Figure 5.4B). For example, at low accelerations (0.02 to $0.05nm/ps^2$) the ratio between the average velocity of methane and that of water is ~ 2, while at higher accelerations (0.06 to $0.08nm/ps^2$) this ratio is ~ 4.3. Note that at $0.05nm/ps^2$, despite the velocity of water and that of methane are the same in the middle of the pore (see Figure 5.4A), the average velocity of methane is as twice the average velocity of water (see Figure 5.4B). This is because water wets the muscovite surface, and the water molecules in the region near the solid surface are effectively not moving along the direction of motion.

5.4.2 Pore-pressure 75MPa

The results discussed in Figure 5.2 strongly depend on the presence of the water bridge and on the flow pattern within the muscovite pore. Building on prior simulation studies for water in clay pores [178, 179], I expect that the stability of the water bridge will depend on the amount of water present within the pore, on the pore size, and on the pore pressure. To test this possibility I conducted simulations reducing the pore pressure from 250MPa to 75MPa. In Figure 5.5 I show how the pore width changes as a function of time when the applied pressure is instantaneously changed from low to 75MPa (compression protocol, filled circles), and when the applied pressure is reduced from 250MPa to 75MPa (expansion protocol, empty circles). In the compression protocol the pore width

decreases from 5nm to 3.58nm, while in the expansion one the pore width increases from 2.65nm to 3.19nm. These results indicate that starting from two different initial configurations, I obtain two stable configurations (insets A and B) that, although characterized by the same pore pressure, are 0.4nm different in width. Analysis of the simulation snapshots (insets) show that the fluid molecules assume different structures within the system: in the configuration presented in the inset A, water molecules accumulate near the solid surfaces while methane remains in the pore center. In the configuration presented in the inset B, water molecules form a bridge between the two solid surfaces. The resultant capillary force brings the two pore surfaces closer by 0.4nm compared to when the bridge is not present. Investigation of the total energy of both compression and expansion systems (results not shown) indicate that the configuration shown in inset B is more stable than that depicted in inset A, suggesting that the capillary force is essential in determining the stable pore structure at the nanoscale. Because we observed two different final configurations starting from two different approaches (expansion vs. compression) it is suggested that more simulations initiating from different initial configurations should be performed to obtain the significant statistics.

From the last configurations shown in insets A and B for the pore at 75MPa I initiate flow simulations. The results show that the imposed flow does not change the fluid distribution within the pore when the simulations start from the structure shown in inset A for all accelerations applied. In this case my results are consistent with the annular two-phase flow described in micro-channels. The

82

correspondent average velocity along the X direction for water (empty circles) and methane (empty triangles) during the simulated two-phase flow are shown in Figure 5.6A. The results suggest that the average velocities of both water and methane increase linearly for the whole range of acceleration studied, which is consistent with Darcy's law. The ratio between the average velocity of methane and that of water (empty circles, Figure 5.6B) is ~ 12.

When I simulate the fluid flow starting from the configuration presented in the inset B of Figure 5.5, my results show that the flow pattern changes over time. When the imposed acceleration is in the range from $0.02nm/ps^2$ to $0.06nm/ps^2$, the water pillar remains, but it becomes thinner as the simulation progresses. One macroscopic consequence of this result is that the pore width slightly increases over time (see filled triangles in Figure 5.5). When the applied acceleration is increased further to 0.07 and $0.08nm/ps^2$, the water bridge vanishes, causing the expansion of the pore from 3.19nm to 3.59nm (empty triangles in Figure 5.5). In other words, when the applied acceleration is large enough, the fluid structure within the pore changes from that pictured in inset B to that in inset A. The correspondent average velocity along the X direction for water (filled circles) and methane (filled triangles) during the simulated two-phase flow are shown in Figure 5.6A. The results indicate that the average velocities of both water and methane increase linearly when the applied acceleration increases from 0.02 to $0.06nm/ps^2$, which is consistent with Darcy's law. Within this range of applied accelerations, the ratio between the average velocity of methane and that of water (filled circles, Figure 5.6B) is around 6.4. When the applied acceleration

increases to 0.07 and 0.08nm/ps^2, as a step increase of the methane average velocity and a slight decrease of the water average velocity are observed. The ratio between the average velocity of methane and that of water increases to 12 (filled circles, Figure 5.6B), consistent with the results obtained starting the flow simulations from the configuration of inset A of Figure 5.5. As described above, when the acceleration increases to 0.07nm/ps^2, there are major changes in flow pattern and in pore size. Both changes contribute to the step increase of the average velocity of methane. Unexpectedly, the change in flow pattern slightly decreases the average velocity of water, despite of the increase in acceleration. This is because the water in the centre of the pore of inset B of Figure 5.5 can move faster, even at the smaller acceleration, along the X direction than the water in the water film near the surface in the inset A of Figure 5.5. The water molecules at the center of the pore move closer to the surface when the bridge is disrupted, leading to lower average velocity for water molecules.

84
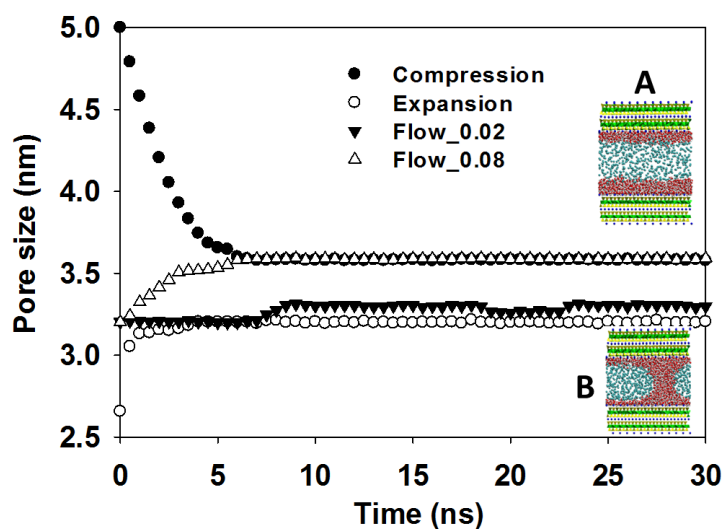
Figure 5.5 Pore size as a function of simulation time obtained for 75MPa compression (filled circles), expansion (empty circles), flow at acceleration of 0.02nm/ps^2 (filled triangles), and 0.08 nm/ps^2 (empty triangles) simulations.
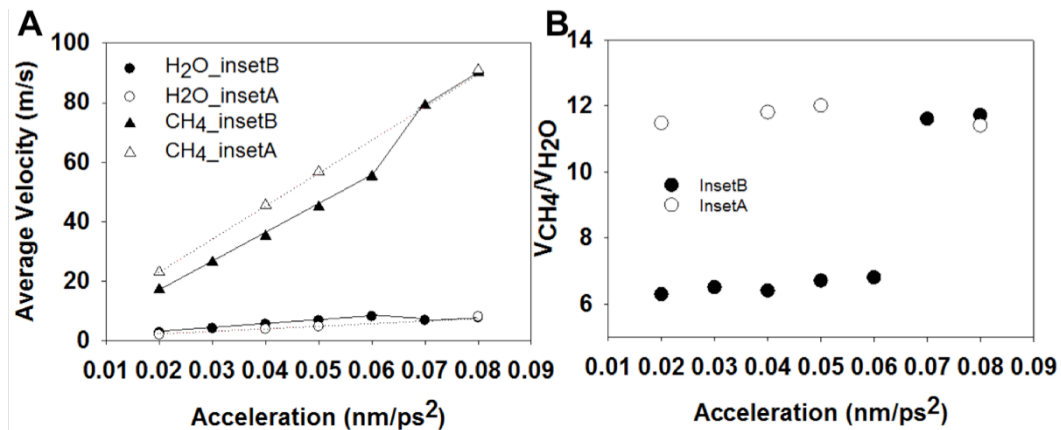
Figure 5.6 Average velocity along the X direction of water (circles) and methane (triangles) during the two-phase flow simulated within the muscovite nano-pore described in inset A (empty symbols) and inset B (filled symbols) of Figure 5.5 as a function of the applied acceleration (A). Ratio between the average velocity of methane and that of water during the two-phase flow described in inset B (filled circles) and inset A (empty circles) of Figure 5.5 as a function of applied acceleration (B).

The results just discussed indicate that the fluid flow can alter the effective interactions between water, methane, and pore surfaces, with effects not only on flow patterns and applications of the Darcy's law, but also on the pore structure.

5.5 Conclusions

Using molecular dynamics simulation I study the two-phase flow of water and methane inside slit-shape pores obtained from muscovite. The simulations are designed to investigate the effect of flow patterns on the fluids transport and on the pore structure at the temperature of 300K and pore-pressure of either 75MPa

or 250MPa. The results indicate that Darcy's law is obeyed as long as the flow pattern does not change. When the fluid structure changes, the movement of methane with respect to that of water changes. My results illustrate the importance of the capillary force, due to the formation of water bridges across the clay pores, not only on the fluid flow, but also on the pore structure, in particular on its width. When the water bridges are broken, perhaps because of fast fluid flow, the capillary force vanishes leading to the significant expansion of the pore. Because muscovite is considered a model of illite, a clay often found in the shale formations in the Marcellus and Barnett regions, these results advance my understanding regarding the mechanism of water and gas transport in tight shale gas formations.

Chapter 6   Summary and Outlook

6.1   Summary

In this thesis I focus on studying the interfacial fluid behaviours and how these behaviours govern nanoscale fluid transport. In particular, I employ equilibrium and non-equilibrium atomistic molecular dynamics simulations using LAMMPS and GROMACS to study the properties of water, aqueous electrolyte solutions, and methane in contact with metal oxide surfaces, clay minerals, and graphene. From the fundamental understanding of the structural and dynamical properties of the interfacial fluids I learn how to manipulate these properties to enhance the performance of practical applications including nano-fluidic devices, water desalination, energy storage, and shale gas exploration.

The results presented in Chapter 3 demonstrate that liquid water can slip on hydrophilic surfaces, which contradicts conventional knowledge. The responsible molecular signature appears to be the dynamic properties of water molecules within the contact layer, coupled with the strength of water-surface interactions. When preferential adsorption sites exist that are sufficiently close to each other that water migration from one to the next can occur without requiring hopping events, hydrodynamic liquid slip occurs. Because of computing-power limitations, the shear rates considered herein are high, but comparable to those found in high performance lubrication applications. When verified experimentally my results could lead to the advancement of a variety of applications, including the design of hydrophilic nano-porous membranes with

high permeation and self-cleaning hydrophilic surfaces. The desired surfaces should permit atomic-scale sliding of contact water molecules, which could be attained by providing a sufficient amount of preferential adsorption sites, by, e.g., atomic-scale etching, molecular grafting, or by integrating nanoparticles on a surface.

In Chapter 4, I manage to alter the properties of the electric double layer formed within graphitic electrochemical cells. This is achieved by inserting graphene membranes near charged graphitic electrodes. I demonstrate that the ability of manipulating the electric double layer has important implications for the water-energy nexus, as it allows us to both effectively and efficiently store energy and purify water. The compact Helmholtz layer found in the envisioned composite electrochemical cell is not only atomically thick, but it is also able to slip in the direction parallel to the electrodes. The formation of the compact electric double layer significantly enhances the electrodes capacitance, with important implications for the design of electric double layer capacitors. It cannot be overstated that the slippage of the Helmholtz layer is important for the practical realization of the *continuous electrode-membrane desalination cells*. Based on my simulation results, the proposed desalination cell can be operated continuously, achieving up to 100% charge efficiency, recovering 70% of the water initially loaded to the system with 100% salt rejection at salinity < 10g/l, and yielding high water permeability ($30L/cm^2/day/MPa$).

In Chapter 5, I study the two-phase flow of water and methane inside slit-shape pores obtained from muscovite. The simulations are designed to investigate the

effect of flow patterns on the fluids transport and on the pore structure at the temperature of 300K and pore-pressure of either 75MPa or 250MPa. The results indicate that the Darcy's law is obeyed as long as the flow pattern does not change. When the fluid structure changes, the movement of methane with respect to that of water changes. My results illustrate the importance of the capillary force, due to the formation of water bridges across the clay pores, not only on the fluid flow, but also on the pore structure, in particular on its width. When the water bridges are broken, perhaps because of fast fluid flow, the capillary force vanish leading to the significant expansion of the pore. Because muscovite is considered a model of illite, a clay often found in the shale formations in the Marcellus and Barnett regions, these results advance my understanding regarding the mechanism of water and gas transport in tight shale gas formations.

Although some models may not be realistic because of limitation in computational resources my research results significantly contributes to my understanding of the mutual relation between the microscopic properties of interfacial fluids and macroscopic observations. This understanding could provide us a systematically strategy in designing innovative materials and engineering processes.

6.2 Outlook

The results presented in Chapter 3 can be used to further my understanding toward a few phenomena and applications. For example, Rafiee et al. [180] reported experimental and simulation results illustrating the wetting transparency

of graphene. They took advantage of this property to improve the performance of the condensation heat transfer applications. Copper is the material used in heat transfer equipment due to its very high thermal conductivity. To prevent the oxidation of Cu coating is required. If the coating surface becomes more hydrophilic condensed water forms a liquid film that can reduce the heat transfer coefficient. If the coating Cu surface becomes more hydrophobic the nucleation density of condensed water decreases leading to the decrease of heat transfer coefficient. The authors shown that coating one layer of graphene on Cu surface does not significantly change its the intrinsic wettability, as the contact angle measured on Cu surface is comparable with that measured on one-layer-graphene-coating one. Graphene coating not only prevents Cu surface from oxidation but also increases 30-40% heat transfer efficiency. Although coating Cu surface with one layer of graphene does not significantly alter the static contact angle I believe that it would severely change the dynamic contact angle and dynamic properties of water near the copper surface. This is because, based on my result reported in Chapter 3, the graphene with the distance between two carbon atoms is ~1.42Å which is smaller than the diameter of water molecule will be an excellent platform for water slippage. This argument is currently being investigated in my group.

The results reported in Chapter 4 indicate that the water molecules and ions can slip inside very narrow charged graphene channels. My hypothesis is that charged graphene surface might become very hydrophilic, but water still can slip on it. To support this hypothesis, I will investigate the effect of surface charge density on

the contact angle and on the degree of water slippage. If successful, this work will serve as a reliable complement to my research reported in Chapter 3 because charged graphene surface can be obtained experimentally.

I are also interested in CO_2 sequestration research. The interactions among injected CO_2, saline fluids, and sedimentary rocks, in particularly the migration of CO_2 are important to designing, predicting the behaviours, and monitoring sequestration systems and sites. As a first prediction, the water 'bridge' observed in Chapter 5 might prevent the CO_2 migration during the injection stage, but can act like a 'seal' to prevent CO_2 leakage during storage stage. The effect of ions on the two-phase system is also of interest. These will be studied in my future research.

Appendix A   Molecular Dynamics Simulation of the Graphene/Water Interface: Comparing Water Models

A.1 Abstract

In this work, different water models (i.e., SPC/E, TIP3P, TIP4P/2005, TIP5P, SPC/Fw, TIP4P/2005f, and SWM4_DP) are implemented to simulate water on neutral, negatively charged, and positively charged graphene. In all cases ambient conditions are considered. Structural and dynamical properties for water are calculated to quantify the differences among the various water models. The results show that SPC/E, TIP4P/2005, SPC/Fw, TIP4P/2005f, and SWM4_DP water models yield a similar structure for interfacial water on graphene, whether it is neutral, negatively charged, or positively charged. TIP5P is the model whose predictions for the structure of the interface deviate the most from those of the other models. Although qualitatively the results are for the most part similar, a large quantitative variation is observed among the dynamical properties predicted when the various water models are implemented. Although experimental data are not available to discriminate the most/least accurate of the model predictions, my results could be useful for comparing results for interfacial water obtained implementing different models. Such critical comparison will benefit practical applications such as the development of energy-storage and water-desalination devices (e.g., electric double layer capacitors), among others.

A.2 Introduction

Graphene is an exceptional material possessing a unique combination of high surface area, extraordinarily mechanical, thermal, chemical, electronic, and optical properties [181, 182]. Graphene is being used in many applications, ranging from materials sciences [183, 184] to the energy field (batteries and electric double layer capacitors) [185-188], from sensing technologies [189] to catalysis [190]. Because some of these applications take place in aqueous environments, it is important to understand at the molecular level the structure and dynamics of interfacial water on graphene under different conditions. Molecular simulations, both dynamics (MD) and Monte Carlo have been carried out for this purpose, and many results have appeared in the literature [35, 85, 191-195]. However, simulation results are known to depend on the force fields implemented. Because several models are available for simulating water [196], one is often left wondering which, among the results reported for water-graphene systems, are general, and which are instead model-dependent observations. Regarding the water/graphene interface, for example, Gordillo et al. [38], and Marti et al. [197] used the single point charge (SPC) water model. Sala et al. [192] implemented the single point charge extended (SPC/E) model and the revised polarizable water model RPOL [137, 198] to detail specific ion effects for aqueous electrolyte solutions confined within graphene sheets. Argyris et al. [39] and Ho et al. [199] used the SPC/E model to study the water/graphite interface. Kannam eta al. [16] implemented the SPC/Fw water model to study the slip length of water on graphene. Cohen-Tanugi and Grossman [35] used TIP4P water model to study how graphene could be used to desalinate water. Taherian et al. [200] studied the contact angle of SPC/E water on graphene. Ulberg and Gubbins used the TIP4P model to study water adsorption in microporous graphitic carbons [195].

Ab initio calculation is also widely used to study graphene/water system. For example, Rana and Chandra [201] compared the results obtained from *ab initio* and classical molecular dynamics simulation to study hydrogen-terminated graphene and water. They concluded that *ab initio* results of water density at interfaces can be reproduced reasonably well by classical simulations with a tuned dispersion potential between the surface and SPC/E water molecules. Tocci et al. [202] applied *ab initio* method to study water/graphene and water/boron nitride systems. They found that although water has very similar structure on graphene and boron nitride surfaces the friction coefficient of water flow on these two surfaces are very different. Cicero et al. [203] reported a first principle study focusing on water confined between single-wall carbon nanotubes and graphene sheets, 1-2.5 nm apart. Their results indicated the presence of the interfacial liquid layer (~5 Å) whose microscopic structure and thickness are independent of the distance between confining layers.

The goal of this contribution is to quantify the effect of implementing different water models on the properties predicted for water at the graphene interface at ambient conditions. I considered several popular water models, including rigid, flexible, and polarizable ones. The properties computed include density profiles, orientation distributions, hydrogen bond networks, residence times for water at contact with graphene, and mobility in the direction parallel to the substrate. In addition to neutral graphene, because of the growing practical importance of devices such as electric double layer capacitors, I also considered uniformly charged graphene substrates. Structural properties for interfacial water such as density profiles and orientation distributions might affect the charge density at the graphene/water interface, and hence affect the performance of electric double layer capacitors. The dynamical properties of interfacial water might determine the time required to charge/discharge

these devices, hence affecting their power density. Although experimental data are not yet available to discriminate the most/least accurate of the models, my results help generalizing the results obtained from different research groups for water at contact with graphitic substrates.

A.3 Simulation details and algorithms

The popular water models used in my simulations are either rigid (SPC/E [45], TIP4P/2005 [46], TIP3P [47], TIP5P [48]), flexible (SPC/Fw [204], TIP4P/2005f [49]), or polarizable (SWM4_DP [205]). SPC/E is a three sites rigid water model. Partial charges were assigned to oxygen and hydrogen atoms, while the center of LJ interactions is the oxygen atom. Many have used extensively the rigid SPC/E water model, which is known to satisfactorily reproduce structure and diffusion of bulk liquid water at ambient conditions. In my simulations, when the rigid SPC/E model was implemented, the two O-H bonds and the fictitious H-H bond lengths were constrained using the SHAKE algorithm [51]. TIP4P/2005 is a four sites rigid model. The oxygen atom carries no charge and is the center of LJ interaction. Partial charges were assigned to each hydrogen atom and to a dummy atom M located along the bisector of the HOH angle. The TIP4P/2005 model is rapidly becoming popular because it reproduces well a variety of thermodynamics properties for water in a wide range of temperatures and pressures [56]. TIP5P is a rigid five-sites water model. A partial charge is placed on each hydrogen atom, and partial charges of equal magnitude and opposite sign are placed on two lone-pair interaction sites. The oxygen atom has no charge and it functions as the center of LJ interactions. The TIP5P water model is known to reproduce well the liquid water density. The average error in the density over the temperature range from -37.5 to $62.5\,°C$ at 1atm is 0.006

g cm^{-3}. In addition, this model predicts the density of liquid water with an average error of ~2% at 25°C over the range from 1 to 10000atm [48]. However, the TIP5P model does not outperform the TIP4P/2005 model when several thermodynamic properties are considered, as discussed by Vega and collaborators [56]. TIP3P is a three-sites rigid water model. It was developed to improve the energy and density for liquid water [47].

Sometimes it is assumed that flexible models are more reliable than rigid ones, because they better represent atomic phenomena such as librations. To test the effect of flexibility on the predicted structure and dynamics of water on the graphene interface I considered two flexible models: SPC/Fw and TIP4P/2005f, the flexible versions (i. e., the O-H bond and HOH angle are allowed to vibrate) of SPC and TIP4P/2005 water models, respectively [49, 204].

Polarizability seems to be extremely important for predicting the properties of aqueous systems at interfaces [206-211], and more and more sophisticated methods are being used to study such systems [212]. To quantify the effect of polarizability on my predictions for the water/graphene interface, I implemented the polarizable model SWM4_DP [205], which is relatively easy to implement, and reproduces well vaporization enthalpy, dielectric constant, self-diffusion coefficient, and air/water interfacial tension [205]. SWM4_DP is a water model with four sites and Drude polarizability. The oxygen atom is the center of LJ interactions. The charge distribution is represented by three point charges: two hydrogen sites and one additional site positioned along the HOH bisector. Electronic induction is described by introducing a classical charged Drude particle attached to the oxygen by a

harmonic spring. The oxygen atom carries a partial charge equal and opposite that of the Drude particle.

The graphene surface in my simulations is neutral, positively charged, or negatively charged. All carbon atoms were maintained rigid and modeled as Lennard-Jones (LJ) spheres by employing the parameters proposed by Cheng and Steele [130]. The cross LJ interaction between unlike species is given by the Lorentz-Berthelot mixing rules: $\sigma_{ij} = \frac{\sigma_{ii}+\sigma_{jj}}{2}$ and $\varepsilon_{ij} = \sqrt{\varepsilon_{ii}\varepsilon_{jj}}$. In Table A.1 various LJ parameters for water-carbon interaction used in this work and in literature are summarized.

Table A.1 Summary of LJ parameters for various water-carbon interactions from my work and from literature.

Water model	σ_{C-O} (Å)	ε_{C-O}(kJ/mol)
SPC/E	3.283	0.3892
TIP4P/2005	3.279	0.4249
SWM4_DP	3.290	0.4476
SPC/Fw	3.283	0.3892
TIP4P/2005f	3.282	0.4249
TIP5P	3.260	0.3949
TIP3P	3.275	0.3851
Wu and Aluru [213]	3.43	0.4865
Wu and Aluru [213]	3.372	0.4343
Pertsin and Grunze [214]	3.256 [215]	1.881 [215]
Feller and Jordan [216]	3.2473	1.297
Scocchi et al. [217]	3.19	0.1998
Werder et al. [215]	3.19	0.3916
Hummer et al. [31]	3.275	0.4784
Won et al. [218]	3.2779	0.4334

Wu and Aluru [213] developed carbon-water non-boned interaction parameters from ab initio calculation data of the interaction energies between graphene and single water molecule. In their calculation, infinite graphene is represented by extrapolation of a series of increasing-size polycyclic aromatic hydrocarbon (PAH) clusters. They

computed PAH-water interaction energies using Moller-Plesset perturbation theory of the second order (MP2) method. They claimed that the interaction parameters obtained ($\sigma_{C-O} = 3.43\text{Å}, \varepsilon_{C-O} = 0.4865 \frac{kJ}{mol}$) from MP2 data predict well the carbon nanotube radial breathing mode frequency shift when compared with experimental data. They also developed the carbon-water interactions from ab initio data available in the literature [219] from density functional theory-symmetry-adapted perturbation theory (DFT-SAPT). The obtained interaction parameter ($\sigma_{C-O} = 3.372\text{Å}, \varepsilon_{C-O} = 0.4343 \frac{kJ}{mol}$) predicted the contact angle of water on clean graphene surface is 42 ± 7°, which is agreement with experimental value [220]. Feller and Jordan [216] used MP2 method to calculate the electronic binding energy of $24.27 \pm 1.67 \frac{kJ}{mol}$ between a water molecule with single-layer graphite. In MD simulation parameters of $\sigma_{C-O} = 3.2473\text{Å}, \varepsilon_{C-O} = 1.297 \frac{kJ}{mol}$ are expected to recover this binding energy [215]. Pertsin and Grunze [214] implemented MP2 method to calculate the binding energy of water-acene complexes and proposed the interaction parameters of $\sigma_{C-O} = 3.256\text{Å}, \varepsilon_{C-O} = 1.881 \frac{kJ}{mol}$ for a single-site water model.

Scocchi et al. [217] tuned the carbon-water interaction (they used SPC/Fw water model) to fit the contact angle obtained from MD simulation with the experimental contact angle of water on graphite. The carbon-water interaction parameters of $\sigma_{C-O} = 3.19\text{Å}, \varepsilon_{C-O} = 0.1998 \frac{kJ}{mol}$) predict the contact angle of 127° of water on graphene, which is agreement with experiment [221]. Werder et al. [215] recovered experimental contact angle of 86° [222] when using $\sigma_{C-O} = 3.19\text{Å}, \varepsilon_{C-O} = 0.3916 \frac{kJ}{mol}$.

From the discussion above it can be seen that different methods used to develop carbon-water interaction result in different parameters. In this chapter, I simulate different water model on graphene with aim to quantify the effect of implementing different water models on the properties predicted for water on the neutral and charged graphene at ambient conditions and to enrich the results obtained for water/graphene system.

When the graphene surface was charged, all the fixed carbon atoms belonging to the graphene sheet on top of the graphitic slab (shown below) carried the same partial charge. In this contribution, I only compare the structural and dynamical properties of water simulated by different water models on $-10\mu C/cm^2$ and $+10\mu C/cm^2$ charged graphene. The selected surface charge densities (positive and negative), although larger than expected in practical devices (e.g., in electric double layer capacitors) were chosen to enhance the different behaviour of interfacial water as predicted by the various models implemented. To maintain the neutrality of the system, I added the necessary ions to water. Because the number of ions is small, these are not expected to affect the water properties reported herein [223]. A systematic investigation regarding the effect of surface charge density (from $-10\mu C/cm^2$ to $+10\mu C/cm^2$) on the behaviour of water at water/graphene interface will be reported elsewhere [223]. The graphene surface used here is non-polarizable. The effect of graphene polarization on the water properties has been recently discussed [224] and presented in Appendix B.
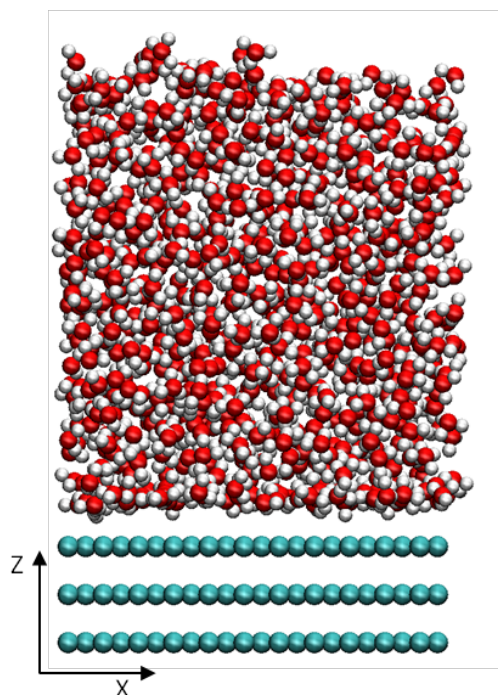
Figure A.1. Side view of the simulation box with SPC/E water molecules on a graphitic surface. Red, white, and cyan spheres represent oxygen, hydrogen, and carbon atoms, respectively.

In Figure A.1 I represent schematically a simulation domain containing SPC/E water molecules on a neutral graphitic surface. Similar domains were employed for all other simulations discussed herein. In my simulation box, a thin film composed of 829 water molecules was placed on a $27 \times 30 \text{Å}^2$ graphitic substrate. Other simulation details were discussed elsewhere [224].

In all simulations presented here the temperature was maintained constant at 300K. It is known that temperature has a strong effect on both structural and dynamical properties of fluids, including those of water. For brevity, such effects are not discussed herein, but I refer to recent work by Gordillo and Marti, and their coworkers, who addressed temperature effects for water confined in carbon-based

pores. For example, in a recent contribution they observed that the density profiles of oxygen atoms near graphite obtained at 298K and 323K are identical [38].

A.4 Results and discussions

Density Profiles

In Figure A.2 I present the oxygen (left) and hydrogen (right) density profiles obtained for different water models on neutral (top), $-10\mu C/cm^2$ charged (middle), and $+10\mu C/cm^2$ charged (bottom) graphene. The results obtained for water on neutral graphene presented in the top panels suggest that SPC/E, TIP3P, TIP4P/2005, SPC/Fw, TIP4P/2005f, and SWM4_DP water models yield quantitatively slightly different, but qualitatively very similar vertical distributions for both oxygen and hydrogen density profiles. The one model that systematically yields results that differs compare to those obtained using the other models is the TIP5P water model. The differences are particularly evident when the hydrogen density profiles on neutral graphene are compared (top right panel). In particular, this model yields a lower and slightly wider first hydrogen peak compared to those predicted using the other models. This difference suggests that TIP5P water assumes a different orientation at the graphene interface, compared to the one predicted using the other models. On the density profiles obtained water simulated on neutral graphene oxygen water forms the first peak at 3.15Å and second peak at 6.15Å for all water model. These results are in good agreement with thoes reported by Werder et al. [215] (they observed first and second peak at 3.2 and 6.2, respectively). Note that the carbon-water interaction used by Werder et al. [215] obtained by fitting the contact angle obtained from MD simulation with experimental data. The heights of the first peak obtained for SPC/E, TIP4P/2005, TIP4P/2005f, SPC/FW, TIP3P water models are

consistent with their results (2.74g/cm^3). SWM4-DP model overestimate and TIP5P model underestimate the height of the first peak compared with that reported by Werder et al. [215]. TIP4P/2005f and SWM4-DP models overestimate the height of the second peak compared to that predicted from other model and that reported by Werder et al. (1.3g/cm^3) [215]. When comparing the height of the first and second peaks with those reported by Tocci [202] we observed that our results is much smaller (3.7 and 2g/cm^3 for the first and second peaks, respectively). In general SPC/E, SPC/FW, TIP4P/2005, and TIP3P water models predict the density profiles in good agreement with that reported by Werder et al. [215]. It is also worth pointing out that although the TIP3P water model is known not to predict reliably the structure of bulk liquid water at ambient conditions [56], my simulations suggest that this model yields predictions for the vertical distribution on neutral graphene that are essentially indistinguishable compared to those obtained using the SPC/E, TIP4P/2005, SPC/Fw water models.

By comparing the density profiles obtained on neutral vs. charged substrates (both positive and negative) I can quantify the effect of an applied field on the properties of interfacial water. As expected because of electrostatic interactions, when the graphene substrate is positively charged the hydrogen atoms of water are repelled from the substrate; on the contrary, when the substrate is negatively charged the hydrogen atoms are attracted to the surface. A detailed systematic discussion regarding such effects has been reported elsewhere [223], but for the scopes of the present work the important results from Figure A.2 is that all models yield qualitatively similar results. This observation (i.e., that the predictions do not depend on the model details) suggests that electrostatic effects dominate the geometric differences intrinsic of the various implemented models (e.g., 3 vs. 5-site models).

Quantitatively, I observe that on the negatively charged substrate the TIP3P and the TIP5P water models yield results slightly different than those obtained using the other models (less structured water). On the positively charged surfaces no large differences are observed among the various models. These effects are related to the different orientation expected for water on the two substrates, as discussed in more details below.
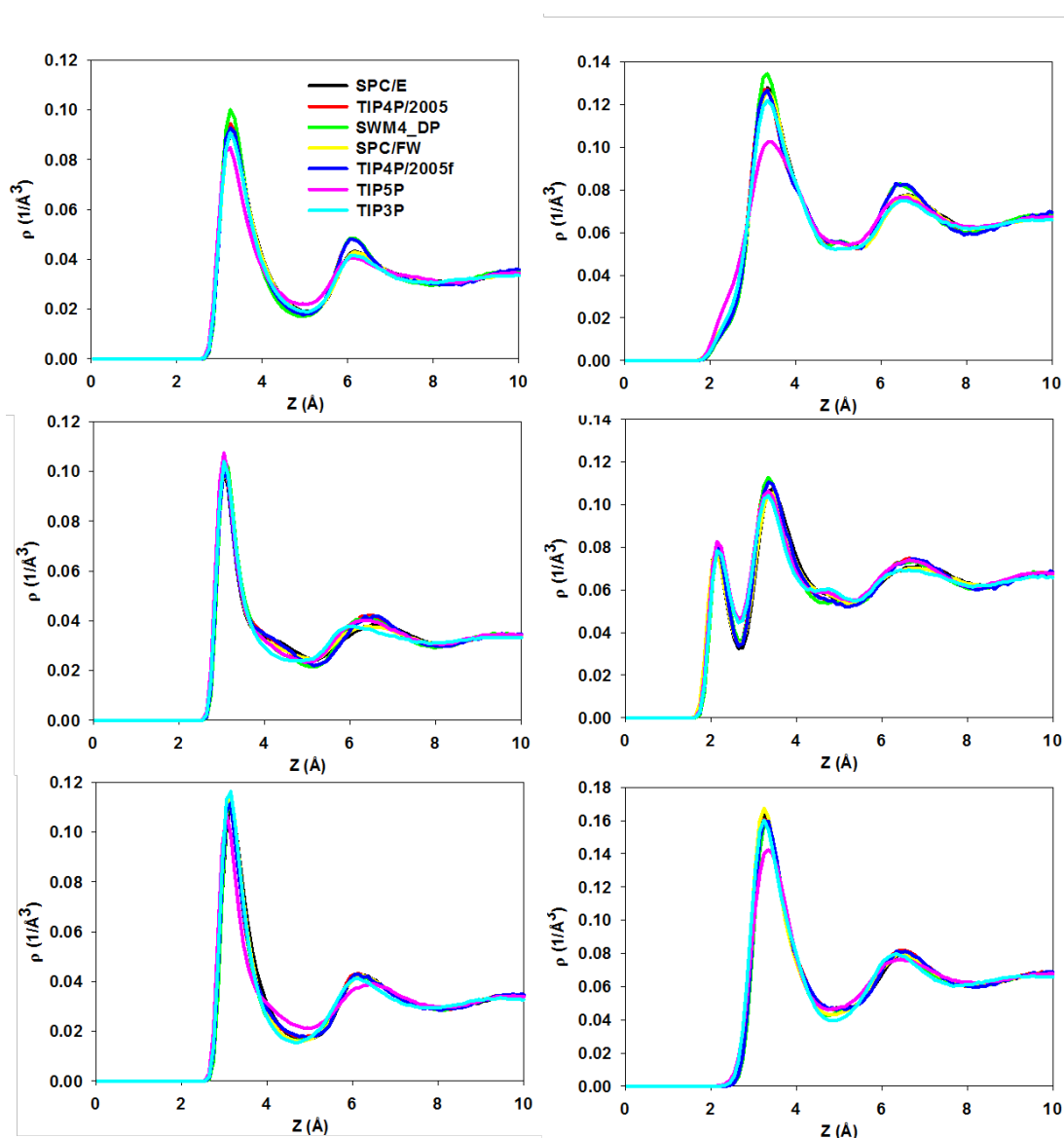

Figure A.2. Oxygen (left) and hydrogen (right) density profiles of water molecules on neutral (top), -10μC/cm^2 charged (middle), and +10μC/cm^2 charged (bottom) graphene. The simulations were conducted at 300 K.

Water orientation

In Figure A.3 I report the orientation distribution probability for interfacial water on neutral (left), negatively charged (middle), and positively charged (right) graphene. The angle Φ is that between the OH bond of one water molecule and the normal vector of the surface. When $\cos(\Phi) = 1$, the OH bond points away from the surface. When $\cos(\Phi) = -1$, the OH bond points towards the surface. Since I are interested in the behaviour of interfacial water molecules, only those water molecules found within the first hydration layer (i.e. within 5Å from the surface, which corresponds to the first minimum observed in the vertical oxygen density profiles) were considered. I report the probability $P[\cos(\Phi)]$ of observing the various angles Φ. The results are in qualitative agreement with the data shown in Figure A.2. Namely, the orientation distribution predicted for all models is very similar, except that obtained for TIP5P water. On neutral graphene, interfacial water molecules simulated by SPC/E, TIP3P, TIP4P/2005, SPC/FW, TIP4P/2005f, and SWM4_DP models prefer to point one of their OH bonds toward the bulk and to maintain the other approximately parallel to the surfaces. On the negatively charged graphene, interfacial water molecules prefer to point the OH bonds toward the surface. On positively charged graphene, the interfacial water molecules seldom point their OH bonds toward the surfaces. More systematic details regarding the effect of surface charge density on the orientation of interfacial water molecules will be reported elsewhere [223]. The differences among predictions from the various models are more evident on neutral and positively charged substrates, while the results obtained on the negative graphene are not significantly different from each other. This suggests that the differences among the various models are due to a large extent to how the water molecules interact with a

neutral surface (i.e., predominantly via dispersive interactions) and/or with a positive one (i.e., predominantly via the interactions between the negative partial charges on the water model and the positive surface charge density). The effect of surface-water interactions is expected to be modulated by water-water interactions, including preferential ones such as hydrogen bonds.
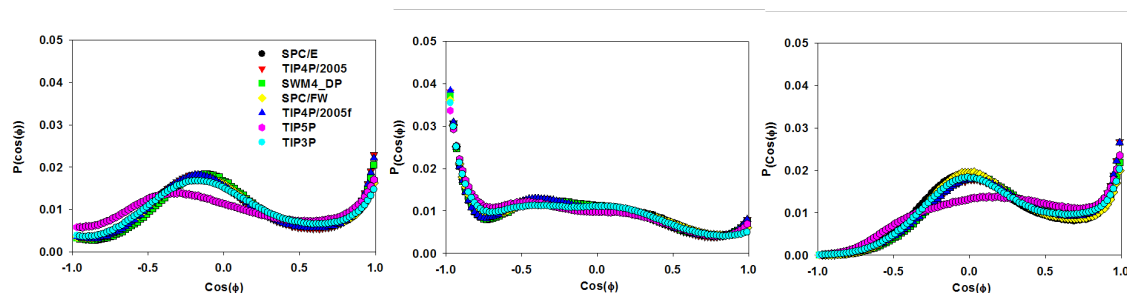
Figure A.3. Orientation distribution of interfacial water molecules on neutral (left), negatively charged (middle), and positively charged (right) graphene. Only the water molecules in the first hydration layer are considered in these calculations. The simulations were conducted at 300 K.

For the scopes of the present work, the important result from Figure A.3 is that the TIP5P water model yields quantitatively different orientation probability distributions $P[\cos(\Phi)]$ compared to those obtained using any of the other models. On neutral graphene TIP5P water has the tendency to point one OH to the bulk and to maintain the other parallel to the surface, but the probability distribution is much more uniform than those predicted for the other models, suggesting that many orientations for interfacial water are possible when the TIP5P model is considered. On the negatively charged graphene, TIP5P yields an orientation distribution that is very similar to those predicted by the other models. My results show that TIP5P water does not point OH bonds towards the positively charged graphene, as

expected. However, the orientation distribution does not show the pronounced preference for $\cos(\Phi) = 0$, as the other models do.

Hydrogen-bond network

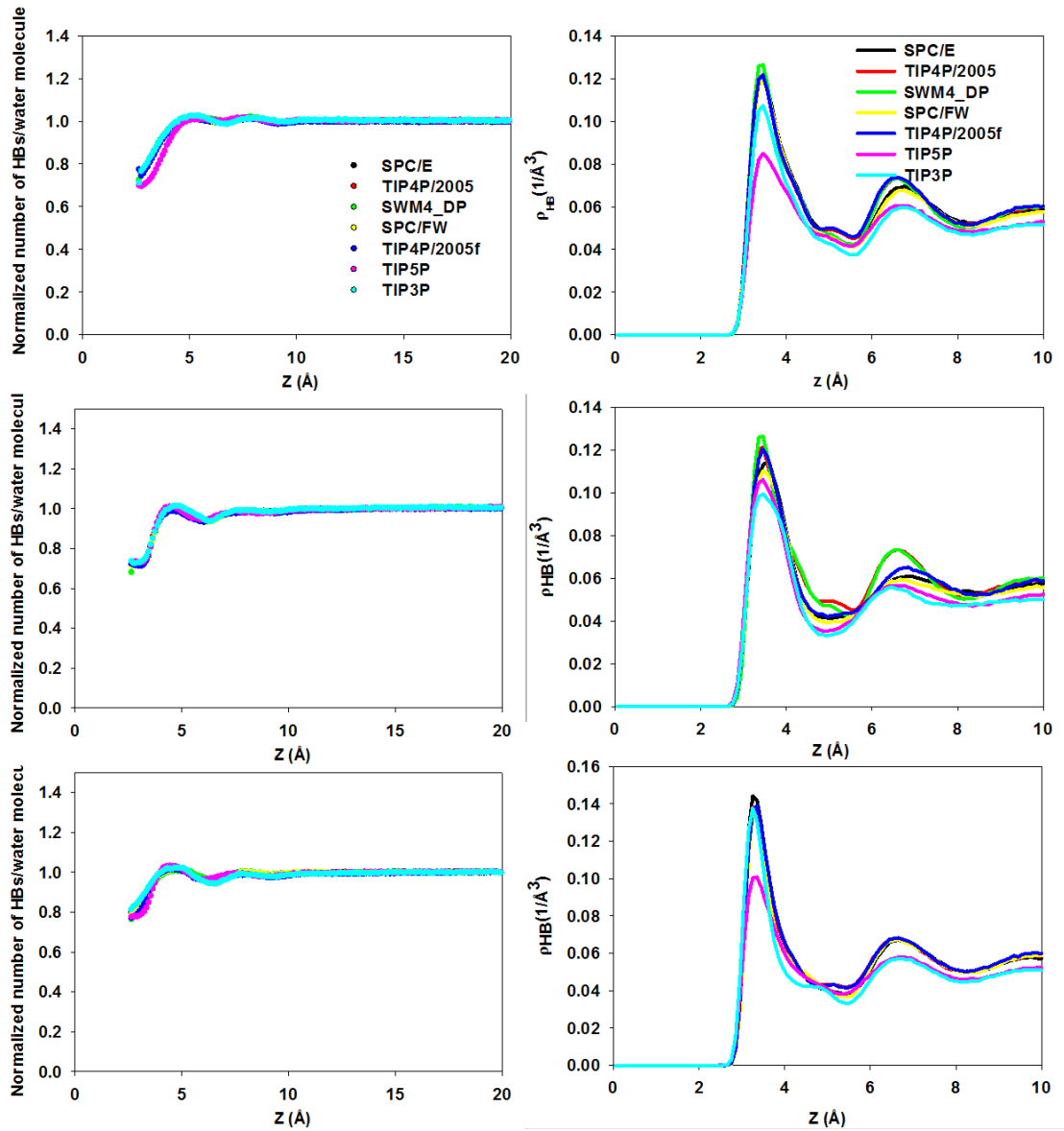Figure A.4. Normalized number of hydrogen bonds per water molecule (left panels) and hydrogen bond density profiles as a function of the vertical distance z from the surface (right panels). The results were obtained for water on neutral (top), negatively charged (middle), and positively charged graphene (bottom). Simulations conducted at 300 K.

In Figure A.4, I report the normalized number of hydrogen bonds (HBs) per water molecule (left), and the hydrogen bond density profiles as a function of the vertical distance z from the surface (right) obtained for water molecules simulated by different models on neutral, negatively charged, and positively charged graphene surfaces. One hydrogen bond was identified using the geometric criterion proposed by Marti [225]. The position of each hydrogen bond was considered as the middle point between the hydrogen of the donor and the oxygen of the acceptor molecules. The number of HBs per water molecule as a function of the distance z from the surface was normalized by the number of HBs the various water models can form in the bulk. Based on my calculations, the number of HBs formed by one water molecule in the bulk depends on the model: 3.45 for SPC/E, 3.50 for TIP4P/2005, 3.45 for SWM4DP, 3.40 for SPC_FW, 3.55 for TIP4P/2005f, 3.10 for TIP5P, and 3.10 TIP3P. I point out that others have reported the number of HBs per bulk water and that the data reported depend on the algorithm used to define a HB [226-228]. The number of HBs/water molecule calculated for SPC/E, TIP4P/2005, SWM4DP, SPC_FW, and TIP4P/2005f water models reasonably agrees with the experimental value of 3.3 reported by Smith et al. [229] and ab initio data found by Tocci et al. (3.5HBs/water molecule) [202]. However, the number of HBs reported here is smaller than that reported by Werder et al. (3.7HBs/water molecule) [215]. I observed that TIP5P and TIP3P models yield fewer hydrogen bonds per water molecule, both in the bulk and at the interface. When the number of hydrogen bonds per water molecule is normalized by the value obtained in the bulk, however, all models yield similar results (left panels in Figure A.4), suggesting that the effect of neutral or charged graphene on the hydrogen bond network is general, and does not depend on the model implemented to simulate water. I only observe small

differences between the TIP5P predictions and those by the other models on neutral graphene, and TIP3P and the other models on positive graphene.

In general, I observe two maximums on the number of HBs/water molecule profiles. The first maximum is observed at 5Å and the second maximum is found at 7.8Å. This observation is consistent with that reported by Werder et al. [215], even though the peak height is different because of the difference in the number of HBs/bulk water molecule as I mentioned in previous paragraph. My results also suggest that the water molecules in the first hydration layer (up to 5Å from the surface) form fewer hydrogen bonds than the molecules in the bulk region do because of the asymmetry of the system generated by the presence of the flat surface (left panels). However, in correspondence of the first hydration layer I observe a large density of hydrogen bonds (right panels – note that the results on the right panels have not been normalized by bulk values), which is due to the high density of water molecules within the first hydration layer (see density profiles in Figure A.2). These observations are in qualitative agreement with the results obtained for SPC water on graphite reported by Marti et al. [197] and by Gordillo et al. [38]. The results on the right panels show that the density of hydrogen bonds predicted for the TIP5P water model within the first hydration layer is much lower than that predicted for the other models. This is in part due to the lower number of hydrogen bonds this water model is able to form, even in the bulk, and also to the lower density of TIP5P water within this region, as discussed in Figure A.2, compared to the results observed for other models. The TIP3P water model also yield lower HBs density compared to SPC/E, TIP4P/2005, SPC/FW, TIP4P/2005f, and SWM4_DP models. This is mainly because of the lower of the number of HBs per water molecule of the TIP3P, while I point out that the density of interfacial TIP3P water is comparable to that predicted by the

models just listed. On the neutral and negatively charged substrates I observe that the SWM4_DP, the TIP4P/2005, and the TIP4P/2005f models yield a higher density of water-water HBs within the second hydration layer, compared to predictions from other models. The results obtained for the SWM4_DP model also suggest the presence of a shoulder in between first and second hydration layer, suggesting a higher probability, compared to results obtained for the other models, of HBs between water molecules in the first hydration layer and those in the second. This shoulder is present for other models as well (i.e., for the TIP4P/2005 on neutral and negative substrates, and for TIP3P on the positive substrate). It is likely that the position of this shoulder is a consequence of the criterion used to define a HB, as several pieces of evidence suggest that water-water HBs do form between water molecules belonging to different hydration layers [230, 231].

Dynamic Properties

As I discussed above, the structural properties predicted for water simulated by SPC/E, TIP4P/2005, SPC/Fw, TIP4P/2005f, and SWM4_DP models are very similar to each other. TIP5P and TIP3P water models yield somewhat different results, although the differences are not very pronounced. In this section I present some dynamical properties such as the mean square displacement in the direction parallel to the substrate, MSD, and the residence auto-correlation function obtained for interfacial water molecules as a function of time. I compare results obtained on neutral, negatively charged, and positively charged graphene surfaces.

The method to calculate MSD is described elsewhere [224]. The slope of the in-plane MSD as a function of time could be used to estimate the self-diffusion coefficient for water molecules in the direction parallel to the surface. However, to quantitatively

estimate the self-diffusion coefficient form this analysis, the MSD analysis should last for infinite times, which is not possible as water molecules eventually leave the hydration layer. Qualitatively, I estimate the mobility of interfacial water from the slope of the MSD data. The larger of the slope, the faster interfacial water molecules diffuse [232]. The obtained results are presented in Figure A.5 for interfacial water on neutral (top left), negatively charged (top right), and positively charged (bottom left) graphene.

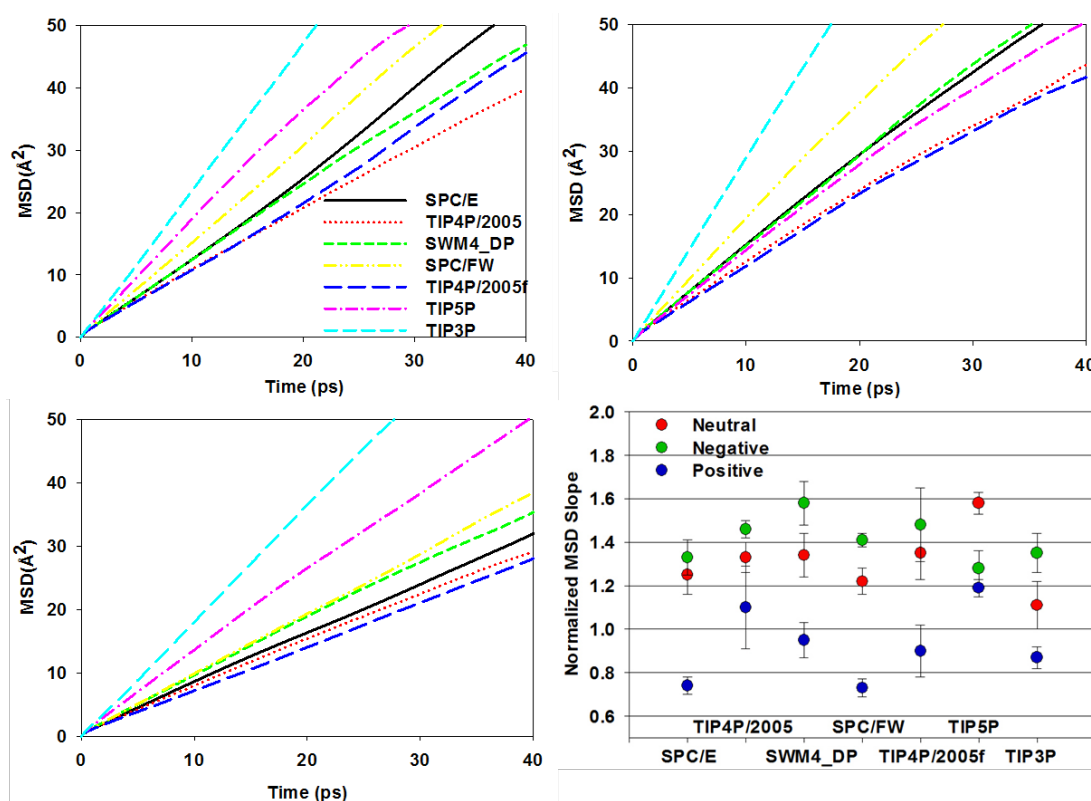Figure A.5. Mean square displacement as a function of time for interfacial water simulated by different models. The results were obtained on neutral (top left), negatively charged (-10μC/cm^2, top right), and positively charged (+10μC/cm^2, bottom left) graphene substrates. In the bottom right panel the slope of the MSD data obtained for interfacial water is normalized by the correspondent values for bulk water.

I also performed the in-plane MSD analysis for water molecules found within a slab of thickness 5Å, parallel to the surface but located in the bulk region. In the bottom right panel of Figure A.5 I report my results for the mobility of interfacial water in the form of the MSD slope obtained for interfacial water normalized by the MSD slope calculated for the bulk water. These data are shown explicitly for each model. When the ratio shown in Figure A.5, bottom right panel, is larger than 1 the mobility of interfacial water is predicted to be larger than that of bulk water, and, vice versa, when the ratio is lower than 1 interfacial water is predicted to have slower mobility than bulk water.

Before discussing the results shown in Figure A.5 for interfacial water, it should be noted that the slope of MSD vs. time obtained for bulk water decreases in the following order: TIP3P > SPC/FW > TIP5P > SPC/E > SWM4_DP > TIP4P/2005 > TIP4P/2005f. These results are not shown for brevity, as I focus here on interfacial water. The latter results, shown in Figure A.5, indicate that the various water models yield very different MSD vs. time data. On the neutral surface (top left) the slope of MSD vs. time for interfacial water decreases in the following order: TIP3P > TIP5P > SPC/FW > SPC/E > SWM4_DP > TIP4P/2005 ~ TIP4P/2005f. When I normalize the MSD data for interfacial water to the correspondent values obtained for bulk water I obtain the results shown in the bottom right panel of Figure A.5 (red circles). Qualitatively, these results suggest that interfacial water has higher mobility in the direction parallel to the interface than bulk water does. Quantitatively, data for SPC/E, TIP4P/2005, SWM4_DP, SPC/FW, and TIP4P/2005 water models are consistent with each other (interfacial water on neutral graphene has mobility ~ 1.3 times that of bulk water). Results for TIP5P and TIP3P water models differ in that

111

TIP5P shows interfacial mobility nearly 1.6 faster than bulk TIP5P water, while interfacial TIP3P water moves just 1.1 times faster than bulk TIP3P water does.

On the negatively charged graphene (top right panel in Figure A.5), interfacial water migrates faster than interfacial water does on neutral surfaces, and my data show a strong dependence on the model implemented to simulate water. However, the normalized slope of MSD vs. time data (green circles in the bottom right panel) suggest that the mobility of interfacial water on the negative substrate is $\sim 1.3 - 1.5$ times that of bulk water for all water models considered. It appears that the intrinsic properties of water are such that on a negatively charged and atomically smooth substrate the water mobility is faster than in the bulk.

On the positively charged graphene, the results for the MSD show strong dependency on the model implemented to simulate water (bottom left panel). When the MSD slopes are normalized by the values obtained in the bulk for the correspondent models (blue circles in the bottom right panel), my data suggest that in general interfacial water on positively-charged graphene is predicted to have slower mobility than bulk water does. For SPC/E, TIP4P/2005, SWM4DP, SPC/FW, TIP4P/2005f, TIP3P water models the ratio between the MSD slopes is $\sim 0.7 - 0.9$. Some exceptions are however noticeable. For example, my results for TIP5P water yield mobility of interfacial water ~ 1.2 times that of bulk water. Experimental data for the mobility of water on positively charged graphene would be extremely valuable for discriminating the abilities of the various models to reproduce experimental observations.

As suggested by Wu et al. [204], it is likely that differences in quantitative predictions are due to differences in equilibrium bond length and angles predicted by

the various water models. The fact that results obtained for TIP4P/2005 and TIP4P/2005f models are comparable suggests that flexibility (bond stretch and angel bend) negligibly affects the water properties presented herein.

Table A.2. Time (ps) for C_R decay from 1 to 1/e for each water model on the three substrates considered. For comparison, I also report the correspondent values obtained for bulk water.

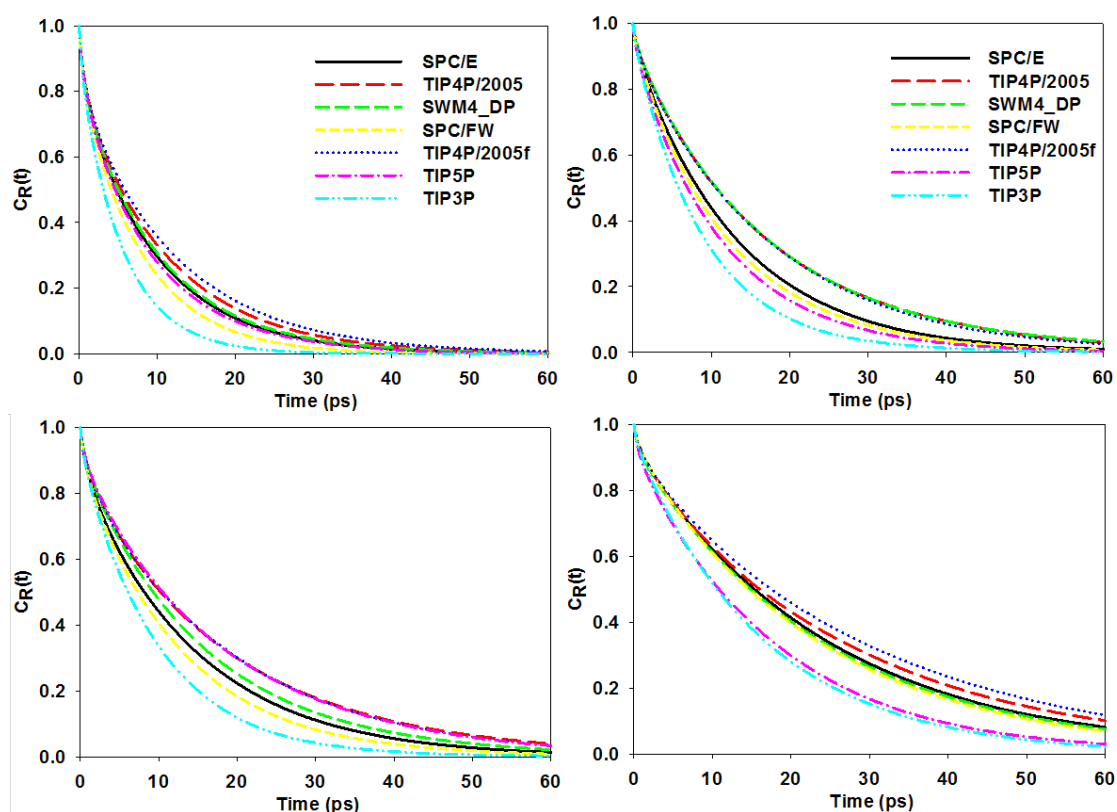| Water model	Neutral	Negative	Positive	Bulk
SPC/E	12.6±0.2	12.9±0.3	23.0±0.2	7.8±0.2
TIP4P/2005	16.0±0.2	15.8±0.2	23.8±0.6	9.0±0.2
SWM4_DP	15.9±0.3	14.2±0.2	22.6±0.4	8.2±0.2
SPC/FW	11.4±0.2	11.4±0.2	21.8±0.2	6.6±0.2
TIP4P/2005f	16.0±0.2	16.5±0.3	26.2±0.4	9.6±0.2
TIP5P	10.3±0.3	15.7±0.5	16.1±0.3	7.4±0.2
TIP3P	8.7±0.3	9.2±0.2	15.6±0.2	4.8±0.2

Figure A.6. Residence auto-correlation functions for interfacial water simulated by different models. The results were obtained for bulk water (top left), for interfacial water on neutral (top right), negatively -10µC/cm^2 charged (bottom left), and positively +10µC/cm^2 charged (bottom right) graphene. Simulations conducted at 300 K.

The residence auto-correlation function was estimated following the method I used previously [224]. By studying the residence auto-correlation function it is possible to estimate the average residence time for water molecules at contact with the graphene (e.g., the time required for the auto-correlation function to decay from 1 to 1/e) [232]. For comparison, I also calculated the residence auto-correlation function for bulk water in a slab of thickness 5Å, parallel to the substrates, and centered at 22Å from it. It should be noted that the water molecules in this bulk slab can leave it from two surfaces, and therefore C_R is expected to decay much more quickly in the bulk than at the interface.

The results for C_R obtained for all water models on the various substrates are shown in Figure A.6. In this figure I also show the results obtained for the various water models in the bulk (note that the results in the bulk do not depend on the charge applied to the substrate). Visual inspection of the data shown in Figure A.6 suggests that TIP3P water resides at all interfaces for the shortest times. TIP3P is also found to leave the bulk volume more quickly than the other water models. On the positively charged graphene, TIP5P water shows comparable dynamics than TIP3P water. The SPC/E, SWM4_DP, TIP4P/2005, TIP4P/2005f water models yield comparable results on positively and negatively charged graphene substrates.

To further quantify the data shown in Figure A.6, I calculate the time required for C_R to decay from 1 to 1/e for each water model on each of the substrates considered (residence time). The results are shown in Table A.2. For comparison, the residence times for the various water models in the bulk are also reported in Table A.2. Analysis of the results in Table A.2 suggests that water molecules reside on average for much longer times within the first hydration layer on each of the substrates

114

considered than they do on a equal volume in the bulk. This is expected, because, as mentioned above, water molecules can leave the bulk volume across two surfaces, while interfacial water can only leave the interface via one surface. In addition, the presence of the solid support, the higher local density of water, and the hydrogen bond network are likely to retain water molecules for longer times within the first hydration layer. My results suggest that for most of the models considered the residence time near neutral graphene is comparable to that near negatively charged graphene. Two exceptions are evident: SWM4DP water resides longer on the neutral than on the negative support, while TIP5P water resides longer on the negative than on the neutral graphene. Comparing the residence times on positive and negative supports I observe that all models predict that water molecules reside far longer times within the hydration layer on the positively charged graphene than on the negatively charged graphene. The only exception is SWM4DP water, for which the residence time on the positive surface is only slightly longer than that on the negative substrate. The longer residence times observed on the positively charged graphene substrates appear to be consistent with the slower mobility predicted on these substrates by analyzing the MSD results (see Figure A.5). Unfortunately, experimental data are not available to discriminate between reliable and non-reliable models.

One additional interesting dynamic property, the HBs lifetime, was not quantified in this chapter. However, I point out that Zielkiewicz [226] compared predictions by SPC, SPC/E, TIP4P, and TIP5P water models against experimental results, and concluded that the TIP5P model under-performs compared to the other models. The HB lifetime reported by Zielkiewicz is 0.551 ps for SPC/E, 0.398 ps for SPC, 0.41 ps

for TIP4P, and 0.253 ps for TIP5P. Experimental data suggest this value should be ~0.6 ps at 298K.

A.5 Conclusions

In this work, the popular water models SPC/E, TIP3P, TIP4P/2005, TIP5P, SPC/Fw, TIP4P/2005f, and SWM4_DP were implemented to simulate interfacial liquid water on neutral, negatively charged, and positively charged graphene substrates at ambient conditions. Some structural and dynamical properties were quantified to rationalize how the solid substrates affect the properties of interfacial water, and whether such effects are general or should be ascribed to model-specific features. My results suggest that SPC/E, TIP4P/2005, SPC/Fw, TIP4P/2005f, and SWM4_DP water models yield very similar structure on the three substrates considered, although small, quantifiable changes are observed among the various models. In short, water is found to yield a hydration layer much denser than bulk water; the orientation of water within this layer depends on the surface charge density and on the formation of a dense water-water hydrogen-bond network. TIP3P and TIP5P water models yield structures for interfacial water that are consistent, yet markedly different compared to those obtained when the other water models are implemented. Based on the comparison among water models recently reported by Vega and coworkers, my results suggest that the predictions obtained implementing TIP3P and TIP5P water models are most likely inferior compared to the others. Out of all the models implemented here, the TIP5P is the only one that employs 4 sites carrying a permanent partial charge. It is possible that this separation of charges leads to the structural differences observed compared to the other, supposedly superior models.

Unfortunately, experimental data are at present not available to substantiate this claim.

When the predicted dynamical properties of interfacial water are compared, my results show more significant model-specific differences among the predicted quantities (residence time for water at contact with the solid substrates, and mobility in the direction parallel to the substrate). In general water molecules reside within the first hydration layer longer than they do in an equal volume found in the bulk, and the residence time is predicted to be much longer on positively than on neutral or negatively charged substrates. In general, the water mobility in the direction parallel to the surface is larger within the first hydration layer than in the bulk for water on neutral and negatively charged substrates; while it is slower on positively charged substrates. Some differences are observed among the model-specific predictions, with SWM4DP, TIP3P, and TIP5P yielding the most marked differences compared to predictions from the other models. My results suggest that the dynamical properties of interfacial water molecules depend more sensitively on the details of the models implemented than the structural properties do. It is likely that the number of charged sites used to describe one water molecule, and the partial charges on each site, have a strong effect on the association and relative between neighboring water molecules, which in turn should affect the molecular dynamics.

Although experimental data are not available to discriminate among reliable and not reliable water models for interfacial studies, my results highlight a number of qualitative results that are consistently predicted when the various models are implemented.

Appendix B   Polarizability Effects in Molecular Dynamics Simulations of the Graphene/water Interface

B.1 Abstract

The importance of including the polarizability of both water and graphene in molecular dynamics simulations of the water/graphene system was quantified. A thin film of rigid SPC/E and polarizable SWM4_DP water on non-polarizable and polarizable graphene surfaces were simulated. The graphene surface was either maintained neutral or charged, positively and negatively. The results suggest that SPC/E and SWM4_DP water models yield very similar predictions for the water structural properties on neutral non-polarizable graphene, although they yield slightly different dynamical properties of interfacial water on neutral non-polarizable graphene.

More pronounced were the differences obtained when graphene was modeled with a polarizable force field. In particular, the polarizability of graphene was found to enhance the number of interfacial SWM4_DP water molecules pointing one of their OH bonds towards the neutral surface. Despite this structural difference, the dynamical properties predicted for the interfacial SWM4_DP water were found to be independent on polarizability as long as the polarizability of a carbon atom is smaller than $\alpha = 0.878\text{Å}$. On charged graphene surfaces, the effect of polarizability of graphene on structural properties and some dynamical properties of SWM4_DP water is negligible because electrostatic forces due to surface charge dominate

polarization forces, as expected. For all cases, my results suggest that the hydrogen bond network is insensitive to the polarizability of both water and graphene. Understanding how these effects will determine the accumulation of ions near neutral or charged graphene could have important implications for applications in the fields of energy storage and water desalination.

B.2 Introduction

Many groups have discussed the importance of including the polarizable term in molecular dynamics (MD) simulations, especially in those simulations conducted for ions at the water/air interface [206-209, 233-235]. Levin argued that the ability of adjusting the charge distribution of an ion, i.e., its polarizablity, is necessary to capture the right physic of ions at interfaces [133]. Berkowitz and Perera found significant differences in both energy and geometry for $Na^+(H_2O)_n$ and $Cl^-(H_2O)_n$ clusters depending on whether or not polarizable force fields were implemented [236]. Dang and Smith found that the properties predicted by simulations for water-ion clusters depend on the magnitude of the ion polarizablity [237]. Jungwirth and Tobias [135] demonstrated that heavier halogen anions have a propensity to accumulate at the water/air interface, proportional to their polarizability. Recent interesting results by Caleman et al. explain the surface preference of halides using MD simulations that implemented polarizable force fields [211].

The work briefly summarized above suggests the need of implementing polarizable force fields in simulating aqueous electrolytes at the water/air interfaces. As other interfaces are of practical interest, one wonders whether polarizable effects are important to describe every interface. For example, it is still unclear whether it is important to implement polarizable force fields to simulate solid/water interfaces. In

this work I are concerned with the graphene/water interface. Graphene is an exceptional material possessing a unique combination of high surface area, extraordinary mechanical, thermal, and chemical stability, and remarkable electronic and optical properties [181, 182]. It is being used in many applications, ranging from materials sciences [183, 238] to the energy field (batteries and electric double layer capacitors) [185-188], from sensing devices [189] to catalysis [190]. Because some of these applications take place in aqueous environments, it is important to understand at the molecular level the structure of interfacial water on graphene under different conditions. Simulations are often conducted for such purposes. Most of the simulations for water on graphene reported in the literature were obtained implementing non-polarizable force fields [38, 193, 203]. One exception is the work of Sala et al. [192] These authors studied aqueous electrolyte solutions confined within a graphene slit-shaped pore. Two sets of potential models were implemented: (a) the rigid non-polarizable SPC/E potential for water with non-polarizable ions, and (b) the rigid polarizable RPOL model for water with polarizable ions. Graphene was in both cases treated as non-polarizable. The results indicated that polarizable force fields favor the accumulation of ionic species near the solid/liquid interface. To secure progress, I believe it is necessary to quantify the effect of polarizability of both water and graphene on the water properties, as predicted by simulations. When synergistically coupled to experimental data, this quantification will allow accurate prediction of the properties of aqueous electrolyte solutions at the graphene interface, necessary for the development of energy storage (e.g., electric double layer capacitors) and water desalination devices, among others. The performance of these devices depends in fact on the accumulation of ions near graphene, which, as

suggested by the results obtained at the water/air interface, might be affected by polarization effects.

B.3 Simulation methods

In this work, three simulation sets were conducted. In the first set, I considered a thin film of either SPC/E [45] or SWM4_DP [205] water on neutral, non-polarizable graphene. These simulations were conducted to verify the importance of implementing a polarizable water model when the water/graphene system is of interest. Within the SPC/E model water is described as rigid with three point charges: two hydrogen sites and one oxygen site. The oxygen site also corresponds to the center of Lennard-Jones (LJ) interactions. This model has been extensively used by many, and it is known to satisfactorily reproduce structure and diffusion of bulk liquid water at ambient conditions. In my simulations one SPC/E water molecule was kept rigid by applying the SHAKE algorithm [51] to constrain the two OH bonds and the fictitious H-H bond length. The polarizable water model SWM4_DP was chosen because it reproduces well vaporization enthalpy, dielectric constant, self-diffusion coefficient, and air/water interfacial tension. In the SWM4_DP model, the permanent charge distribution of a water molecule is represented by three point charges: two hydrogen sites and one site positioned along the HOH bisector. The electronic induction is represented by a classical charged Drude particle [239, 240], bound to the oxygen site by a harmonic spring. The oxygen site carries a charge equal and opposite to the one of the Drude particle. The oxygen site is also the center of intermolecular LJ interactions. In neutral non-polarizable graphene, all carbon atoms were maintained rigid and modeled as LJ spheres employing literature parameters [130].
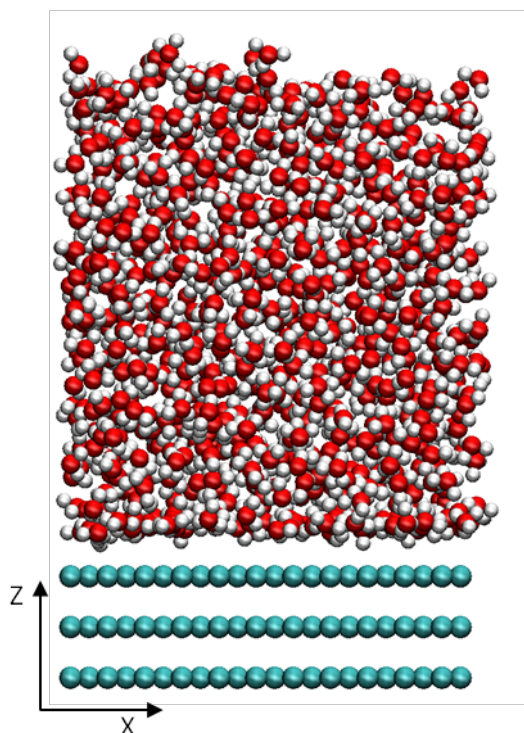
Figure B.1. Side view of the simulation box with SPC/E water molecules on a neutral non-polarizable graphite surface. Red, white, and cyan spheres represent oxygen, hydrogen, and carbon atoms, respectively.

In the second simulation set, a thin film of polarizable SWM4_DP water [205] (polarizability $\alpha \sim 1.042\text{Å}^3$) on neutral polarizable graphene surfaces was simulated to study the effect of graphene polarizability on water properties. To simulate the polarizability of carbon atoms, I implemented the Drude-particle method [239, 240], inspired by the SWM4_DP water model (described in the paragraph above). Each carbon atom was represented by a fixed charged LJ carbon atom and a Drude particle carrying a charge opposite in sign to that fixed on the center. The fixed carbon atom and the Drude particle were connected by a spring. Manipulating the spring constant and the charge on the Drude particle results in different polarizability. The LJ parameters for the fixed carbon atoms were identical to those used in the first simulation set. The polarizability of a carbon atom in graphene is expected to be

around $\alpha \sim 0.878\text{Å}^3$, which is the polarizability of the carbon atom in CCl_4 as simulated by Chang and Dang [241]. Because I excluded the interactions among the carbon atoms in the graphene sheet, the polarizability of carbon atoms used in my simulations should reflect the out-of-plane value. According to Langlet et al. [242], the out-of-plane polarizability of a carbon atom varies from 0.5 to 1.5Å^3. They used 0.86Å^3, close to the value $\alpha \sim 0.878\text{Å}^3$ I expect to be reasonable. Karapetian and Jordan [243] implemented out-of-plane $\alpha \sim 0.57\text{Å}^3$ to study the properties of a water cluster on graphite. They concluded that using an anisotropic polarizability on the carbon atoms gave the similar structures and binding energies to those obtained using an isotropic polarizability. To fully understand the effect of polarizability I conducted additional simulations, varying the polarizability α of a carbon atom from 0 (no polarizability) to 1.1Å^3 (i.e., $\alpha = 0\text{Å}^3$, $\alpha = 0.578\text{Å}^3$, $\alpha = 0.878$ Å^3 and $\alpha = 1.1\text{Å}^3$).

In the third and last simulation set, a thin film of polarizable water SWM4_DP was simulated on charged polarizable graphene and on charged non-polarizable graphene surfaces to understand the role of the polarizability of graphene on the water properties when the graphene surfaces are charged, negatively or positively. The water/charged graphene interface is encountered in many practical applications such as electric double layer capacitor (EDLC) or capacitive desalination (CD) [244]. In the present contribution I considered two representative surface charge densities (i.e., -8 and $+8\mu C/cm^2$). The non-polarizable graphene was simulated as discussed in the first simulation set. The polarizable graphene was simulated using the approach described in the second simulation set, with polarizablity $\alpha = 0.878\text{Å}^3$. When the graphene surface was charged, all the fixed carbon atoms belonging to the graphene sheet on top of the graphitic slab (shown below) carried the same partial charge.

In Figure B.1 I represent a simulation domain containing SPC/E water molecules on a neutral non-polarizable graphite surface. Similar domains were employed for all other simulations. In my simulation box, a thin film composed by 829 water molecules was placed on a 27.0x29.8Å^2 graphite surface. All simulations presented below were conducted using the GROMACS simulation package [42], version 4.0.7. During each simulation the number of particles (N) in the system, the volume (V), and the temperature (T) were maintained constant (i.e., I implemented the NVT ensemble). The system temperature was maintained at 300K by applying the Nose-Hoover thermostat with the relaxation time of 100fs. Periodic boundary conditions were applied in all three directions (note that the Z direction is the one perpendicular to the solid substrate). Long-range interactions were calculated by the particle mesh Ewald (PME) method [245]. Along the Z direction a large vacuum volume was added to eliminate unphysical interactions between periodic images of the simulated system. Similar approaches have been implemented in my prior work [172]. Alternatively, one can apply two-dimensional algorithms available for treating long-ranged electrostatic interactions [246]. The resultant lengths of the simulation box used herein along the X, Y, and Z directions were 2.70, 2.98, and 10.00nm, respectively.

The equations of motion were integrated with a time step of 1fs. After equilibration, the system coordinates were recorded every 200 time steps (i.e., 200fs of simulation), and used for subsequent analysis. Each simulation lasted 3ns. The results obtained during the first 1ns were discarded (equilibration), while the trajectories recorded during the last 2ns of the simulation were used to calculate the properties of interest. By monitoring temperature, density profiles, and orientation probability as a function of simulation time I confirmed that the reported results are obtained after

equilibration is complete. The simulation trajectories were analyzed to extract detailed information regarding atomic density profiles, orientation, residence time, translation and rotational dynamics for interfacial water. Additional details concerning the hydrogen bond network near the interface were extracted. The algorithms employed for such analysis have been described in previous publications from my group [13, 39, 40, 85, 172, 247].

B.4 Results and discussions

Density profiles

In Figure B.2 I present the density profiles in the direction perpendicular to the surface for oxygen (left) and hydrogen (right) atoms of water molecules near graphite. The results are compared when different force fields are implemented.

On the top panels I compare the density profiles obtained for SPC/E and SWM4_DP water simulated on the neutral non-polarizable graphene surface. The comparison suggests a minimal difference due to the polarization. The oxygen density profile obtained for SPC/E water indicates that a first intense density peak forms at z = 3.25Å and a second, less pronounced density peak forms at z = 6.05Å. This is in agreement with results reported by other groups [38, 193, 203]. The oxygen density profile obtained for SWM4_DP water is different from that obtained for SPC/E water, but the differences are almost insignificant. For example, the peaks observed on the oxygen density profile for SWM4_DP are higher and narrower than those observed for SPC/E water. Quantitative calculations presented below indicate that water molecules are predicted to pack in the interfacial layer at a constant surface coverage (9.9 water molecules per nm^2), independently on the water model

implemented. The hydrogen density profiles (top right) also show negligible differences between results obtained implementing either the SPC/E or the SWM4_DP water models. The results presented on the top panels of Figure B.2 demonstrate that the distribution of oxygen and hydrogen atoms of water molecules in the direction perpendicular to the surface are predicted to be comparable when either the rigid non-polarizable SPC/E or the polarizable SWM4_DP water models are implemented.

The next question I address is whether including the polarizability of carbon atoms of graphene and the polarizability of water molecules will affect the predicted structure of water. In the middle panels of Figure B.2 I compare the results obtained using the polarizable SWM4_DP model of water, combined with a Drude-particle model to describe polarizable effects in the carbon atoms of graphene. The results suggest that including the polarizability of graphene negligibly affects the vertical distribution of oxygen atoms of interfacial water (left panel). However, the prediction for the density profiles of hydrogen atoms (right panel) is affected by the polarizability of carbon atoms. In particular, a small shoulder at $z = 2.15\text{Å}$ gradually forms when the polarizability increases. The shoulder found at $z = 2.15\text{Å}$ on the hydrogen density profile is 1Å closer to the surface than the first oxygen peak observed on the oxygen density profile. This suggests that polarizability affects the orientation of interfacial water molecules. My results indicate that the number of water molecules in the first hydration layer projecting one of their hydrogen atoms toward the surface increases when the graphene polarizability increases. This observation is supported by additional results, discussed below, for the orientation of interfacial water molecules and by the estimation of the number of water molecules pointing one of their hydrogen atoms towards the surface. The results just discussed

126

show that polarizability is important in predicting the orientation of interfacial water molecules near neutral graphene. The next question I address is whether or not the same observation holds when the graphene surface, instead of being neutral, is charged.

In the bottom panels of Figure B.2 I present the density profiles predicted when the SWM4_DP water is simulated on charged non-polarizable and charged polarizable graphene surfaces. Graphene was either positively or negatively charged. The density profiles for SWM4_DP water on neutral non-polarizable graphene (black line) are also shown for comparison. The results shown in the bottom panels of Figure B.2 indicate that the surface charge density has a strong effect in determining the orientation of interfacial water. More importantly for the scopes of the present work, however, is that when graphene is charged, my results show that including the polarizability of graphene in the calculations has little effect. For instance, the oxygen density profile (left panel) for water on $-8\mu C/cm^2$ non-polarizable graphene (solid red line) shows little difference compared to that obtained on polarizable graphene (green solid line). The same can be repeated for the hydrogen density profile (right panel) on $+8\mu C/cm^2$ non-polarizable or polarizable graphene.
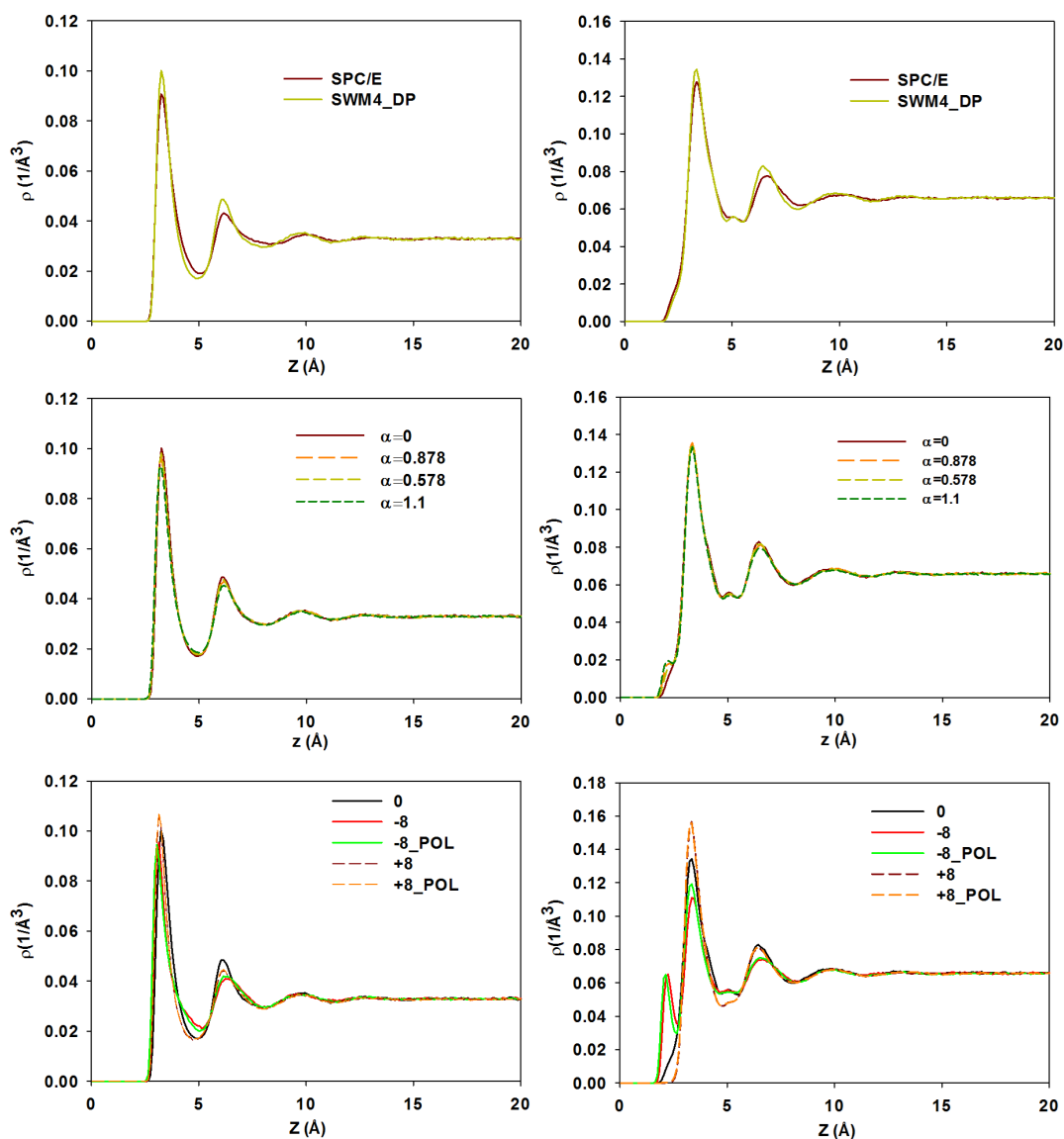
Figure B.2. <u>Top:</u> Oxygen (left) and hydrogen (right) density profiles of SPC/E and SWM4_DP water on neutral non-polarizable graphene surfaces. <u>Middle:</u> Oxygen (left) and hydrogen (right) density profiles of SWM4_DP water on neutral polarizable graphene surfaces of different polarizability α. <u>Bottom:</u> Oxygen (left) and hydrogen (right) density profiles of SWM4_DP water on charged non-polarizable and charged polarizable graphene surfaces.

Orientation

In the left panel of Figure B.3 I present the orientation distribution of interfacial SPC/E (pink circles) and SWM4_DP (black circles) water on neutral non-polarizable graphene. In the left panel I also report the results obtained for SWM4_DP water on

neutral polarizable graphene (red circles, green triangles, and yellow triangles). The angle Φ was defined as the angle between the OH bond of one water molecule and the normal vector of the surface. When $\cos(\Phi) = 1$, the OH bond points away from the surface. When $\cos(\Phi) = -1$, the OH bond points towards the surface. The probability $P\big[\cos(\Phi)\big]$ of observing the various angles Φ for the water molecules whose oxygen atom is found within 5Å from the surface is reported. It should be remembered that Lee et al. [248] were the first to predict that water molecules within the first hydration layer near a hydrophobic surface point some of their OH groups towards the surface to minimize the number of hydrogen bonds lost because of the presence of the surface. Many subsequent simulations for water on graphite agree with such prediction [38, 193, 203]. Qualitatively, the results obtained here on the neutral graphene also show that some of the water molecules within the first hydration layer point one of their OH bonds towards the surface. Further, the results obtained for SPC/E (pink circles) and SWM4_DP (black circles, obtained for α = 0) suggest that the polarizability of water insignificantly affects the orientation of interfacial water when graphene is neutral and not polarizable. However, my results show that the polarizability of graphene affects the orientation of interfacial water. The results obtained for interfacial SWM4_DP water on neutral polarizable graphene indicate that the probability $P\big[\cos(\Phi) \sim -1\big]$ increases when the polarizability increases, indicating that more interfacial water molecules point one of their OH bonds towards the surface when the surface polarizability increases.

In the right panel of Figure B.3 I report the number of oxygen and hydrogen atoms found in the first peak on the density profiles obtained for SPC/E water on neutral non-polarizable graphene (pink circles), and for SWM4_DP water on neutral

129

polarizable graphene. The number of oxygen and hydrogen atoms were counted up to 5Å (the first minima on oxygen density profile) and 2.65Å from the surface (the shoulder on the hydrogen density profile), respectively. On neutral non-polarizable graphene nearly 9% of interfacial water molecules (either SPC/E or SWM4_DP) point one of their OH bonds toward the surface. On the most polarizable graphene considered (α = 1.1), nearly 14% of interfacial SWM4_DP water point one of their OH bonds toward the surface. At the expected polarizability of a carbon atom (α = 0.878), approximately 12% of interfacial water molecules point one OH bond towards the surface. Experimental results show that at water/air interface more than 20% water molecules have 'dangling' OH bonds projecting into the air [249], suggesting that perhaps including polarizability is important for capturing the correct physics of the water/graphene interface as well. Experimental data necessary for validating my predictions are at present not available.
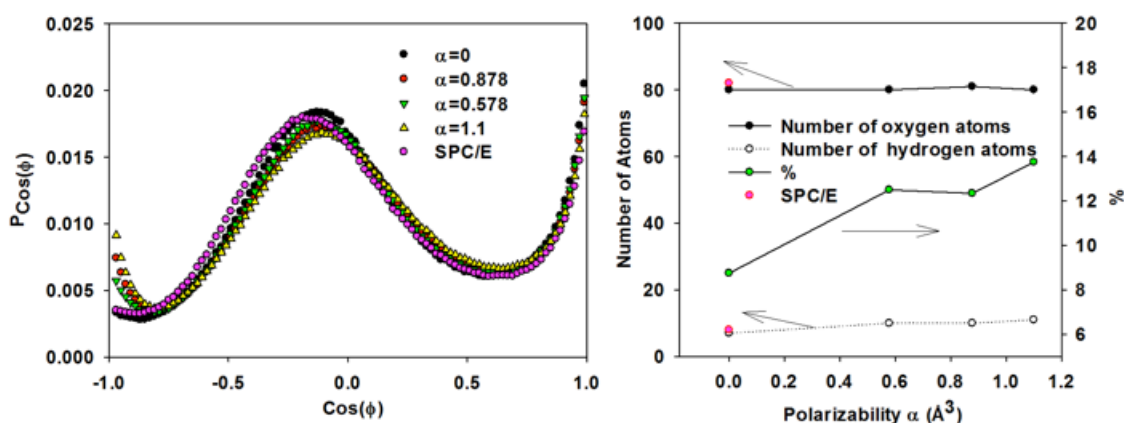
Figure B.3. Left: the orientation distribution of SWM4_DP water molecules on polarizable graphene surfaces. Only the water molecules in the first hydration layer are considered in this calculation. Right: The number of hydrogen and oxygen atoms of SWM4_DP water molecules within the first peaks observed on the atomic density profiles (see Figure B.2). On both left and right panels, the results obtained for SPC/E water on non-polarizable graphene were also reported (pink circle) to compare with the results obtained for SWM4_DP (black) water on neutral non-polarizable graphene.

The orientation distribution of SWM4_DP water on neutral graphene surfaces, presented in the left panel of Figure B.3, clearly indicates the effect of graphene polarizablility on the orientation of interfacial water. Will the polarizability of graphene affect the orientation of water on graphene when the graphene, instead of being neutral, is charged? The orientation distributions of interfacial SWM4_DP water on charged non-polarizable and charged polarizable graphene are presented in Figure B.4. The results obtained for SWM4_DP water on neutral non-polarizable graphene are also shown in this figure for comparison (black). Changing the surface charge density from negative to positive has the expected effect on the orientation of interfacial water. Briefly, water preferentially points more OH bonds towards the negatively charged surface (red triangles, note the high $P[\cos(\Phi) \sim -1]$ in Figure B.4). On the contrary, water points no OH bonds towards the positively charged surface (yellow diamonds, note the low $P[\cos(\Phi) \sim -1]$ in Figure B.4). I focus here on the effect of graphene polarizability on the orientation distribution of interfacial SWM4_DP water on charged graphene. My results show that such effect is negligible. For instance, the orientation distribution of interfacial water on $-8\mu C/cm^2$ non-polarizable (red) and $-8\mu C/cm^2$ polarizable graphene (green), or the orientation distribution of interfacial water on $+8\mu C/cm^2$ non-polarizable (yellow) and $+8\mu C/cm^2$ polarizable (blue) graphene are identical. The electrostatic forces clearly dominate the effect of polarizable forces.
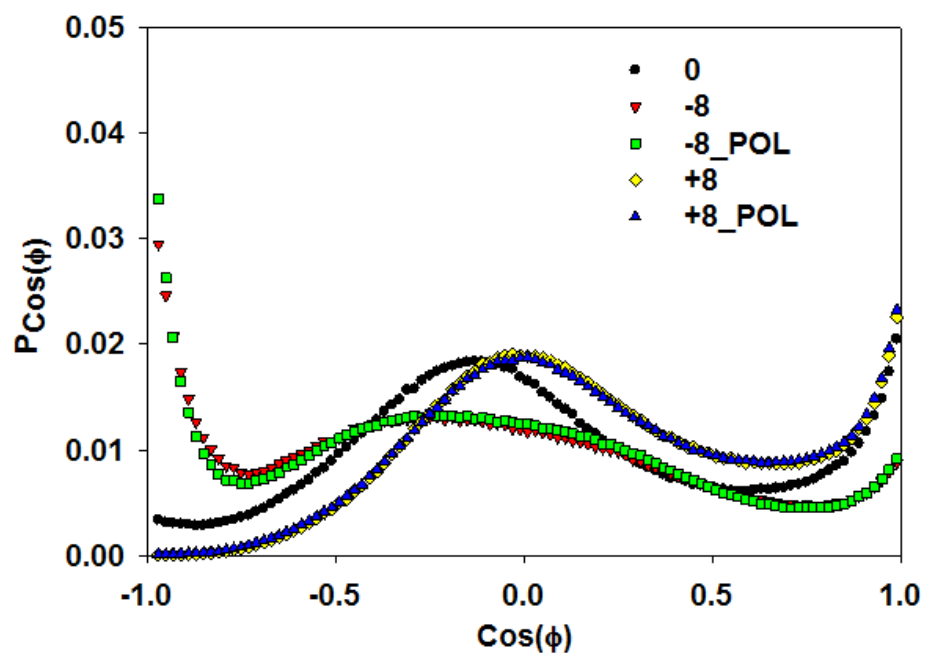
Figure B.4. The orientation distribution of SWM4_DP interfacial water on charged non-polarizable and charged polarizable graphene surfaces. The results obtained for SWM4_DP water molecules (black circle) on neutral non-polarizable graphene are also shown for comparison. Only water molecules in the first hydration layer are used for this analysis.

Hydrogen-bond network
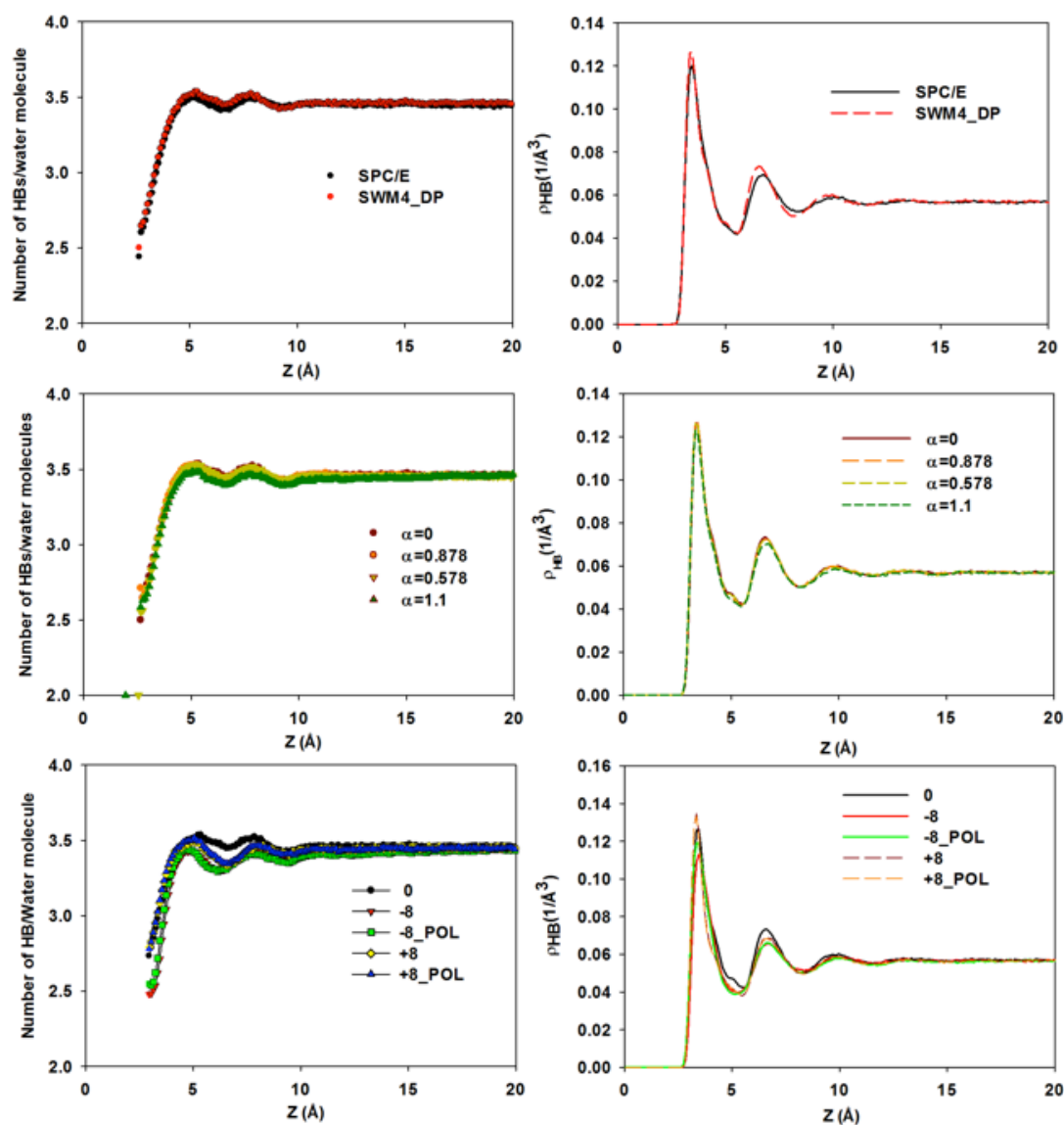
Figure B.5. Number of hydrogen bonds per water molecule (left panels) and hydrogen bond density profiles (right panels) as a function of vertical distance z from the surface. The results obtained for SPC/E and SWM4_DP water on neutral non-polarizable graphene, for SWM4_DP water on neutral polarizable graphene, and for SWM4_DP water on charged non-polarizable and charged polarizable graphene are shown in the top, middle, and bottom panels, respectively.

In Figure B.5 I present the number of hydrogen bonds per water molecule (left) and the hydrogen bond density profiles (right) obtained for SPC/E and SWM4_DP water

on neutral non-polarizable graphene (top), for SWM4_DP water on neutral polarizable graphene surfaces (middle), and for SWM4_DP water on charged non-polarizable and charged polarizable graphene (bottom). One hydrogen bond was identified using the geometric criterion proposed by Marti [225]. The position of each hydrogen bond was considered as the middle point between the hydrogen of the donor and the oxygen of the acceptor molecules. The results presented in the top and middle panels indicate that the polarizability of either water or graphene have an insignificant effect on the hydrogen bond network. The water molecules in the first hydration layer (up to 5Å from the surface) form fewer hydrogen bonds than the molecules in the bulk region do because of the asymmetry of the system (left panels). However, the hydrogen bond network is very dense in the contact layer as observed on the hydrogen density profiles (right panels) because the density of water molecules in the first hydration layer is high (see density profiles in Figure B.2). These observations are in agreement with the results reported by Marti et al. [197] and Gordillo et al. [38]. The results obtained on charged graphene surfaces (bottom panels) also indicate that at the same surface charge density, the non-polarizable and polarizable graphene substrates do not affect the hydrogen bond network differently from each other.

Dynamical properties

In Figure B.6 I present several dynamical properties computed for interfacial water on various graphene surfaces. Only water molecules within the first hydration layer were considered for these calculations. I computed the residence auto-correlation function (left panels), the mean square displacement as a function of time (middle

panels), and the reorientation correlation function (right panels). The results are compared when different force fields were implemented.

The residence auto-correlation function was defined as: $C_R(t) = \dfrac{\langle P(t)P(0)\rangle}{P(0)P(0)}$ $C_R(t) = \dfrac{<P(t)P(0)>}{P(0)P(0)}$. At time $t = 0$ $t = 0$, $P(0) = 1$ for all the water molecules whose oxygen atom is found within the first peak on the oxygen density profile (see Figure B.2). If the water molecules continuously stay in the first hydration layer when the time t progresses, then $P(t) = 1$, otherwise, $P(t) = 0$. The auto-correlation function decays from 1 to 0 when the system evolves because the interfacial water molecules leave the hydration layer as time progresses [232]. By studying the residence auto-correlation function it is possible to estimate the average residence time for water molecules at contact with the graphene (e.g., the time required for the auto-correlation function to decay from 1 to 1/e).

The in-plane MSD was quantified as: $(t) = \dfrac{<\Sigma[(x_i(t)-x_i(0))^2+(y_i(t)-y(0))^2]>}{N(t)}$, where N(t) is the number of water molecules remaining in the hydration layer at time t. Note that as time progresses, $N(t)$ decreases. Once a water molecule leaves the hydration layer, it does not contribute any more to the mean square displacement, even if it returns after some time. The slope of the in-plane MSD as a function of time could be used to estimate the self-diffusion coefficient for water molecules in the direction parallel to the surface, although the correlation should last for infinite times, which is not possible as water molecules eventually leave the hydration layer. Qualitatively, I estimate the mobility of interfacial water from the initial slope of the MSD data. The larger of the slope, the faster interfacial water molecules diffuse [232].

The reorientation correlation function was obtained as: $C_{DM}(t) = \frac{<M(t)M(0)>}{<M(0)M(0)>}$, where

M(0) is the dipole moment of water molecule vector at time $t = 0$ $t = 0$, $M(t)$ is the

dipole moment of water molecules vector at time t. Only water molecules

continuously staying within the first hydration layer were considered for this

calculation. The slower the reorientation correlation function decays from 1 to 0, the

slower the water molecules rotate [232]. The rotational diffusion can be estimated,

qualitatively, from the time required by the reorientation correlation function to

decay from 1 to 1/e.

The comparison of the dynamical properties obtained for SPC/E and SWM4_DP

water on neutral non-polarizable graphene surface is shown in the top panels of

Figure B.6. The results for the residence correlation function (top left) demonstrate

that the SPC/E water molecules stay in the contact layer on average shorter than

SWM4_DP water molecules do. However, the MSD results (top middle) suggest

that SPC/E and SWM4_DP water molecules have similar mobility in the direction

parallel to the substrate. The reorientation correlation function data (top right)

indicate that the SPC/E water molecules rotate more slowly than SWM4_DP water

molecules do. This appears to be counter-intuitive, since SPC/E water was found to

reside in the first hydration layer for shorter times than the SWM4_DP water.

However, I note that the differences are rather small.

The dynamical properties predicted for SWM4_DP water on neutral graphene as a

function of graphene polarizability (middle panels from the top) show differences

only when the polarizability of a carbon atom is larger than α = 0.878Å. Because on

neutral polarizable graphene the orientation of SWM4_DP water was found different

compared to that on non-polarizable graphene, it is surprising that the dynamical

properties of water are not affected by the surface polarizability when α < 0.878Å. It is possible that the dynamics of interfacial water molecules depend more strongly on the presence of ions, whose predicted behaviour (i.e., surface adsorption) might depend on polarizability [192]. This possibility will be explored in the future.

The structural properties of water on charged graphene were found not to depend on graphene polarizability. However, the dynamical properties predicted for interfacial SWM4_DP water on charged graphene appear to depend, to some extent, on the graphene polarizability (bottom panels of Figure B.6). Note that these results were obtained when the polarizability α of carbon atoms of graphene was either 0 or equal to the expected value of $0.878Å^3$. The residence auto-correlation function data (bottom left) show no difference, as a function of surface polarizability, when graphene is charged. However, the MSD data (bottom middle) show that water molecules on charged polarizable graphene have faster mobility along the direction parallel to the substrate compared to water on charged non-polarizable graphene. For example, water molecules on the $-8μC/cm^2$ non-polarizable graphene (dash red) diffuse more slowly than on the polarizable surface with the same surface charge density (dash green). The same can be repeated for the positively charged graphene. Experimental data such as those obtained from NMR or neutron scattering are needed to determine which of these predictions better reproduces reality. The reorientation correlation function data (bottom right) indicate that the effect of polarizability of graphene on the rotation of water on charged graphene is negligible.
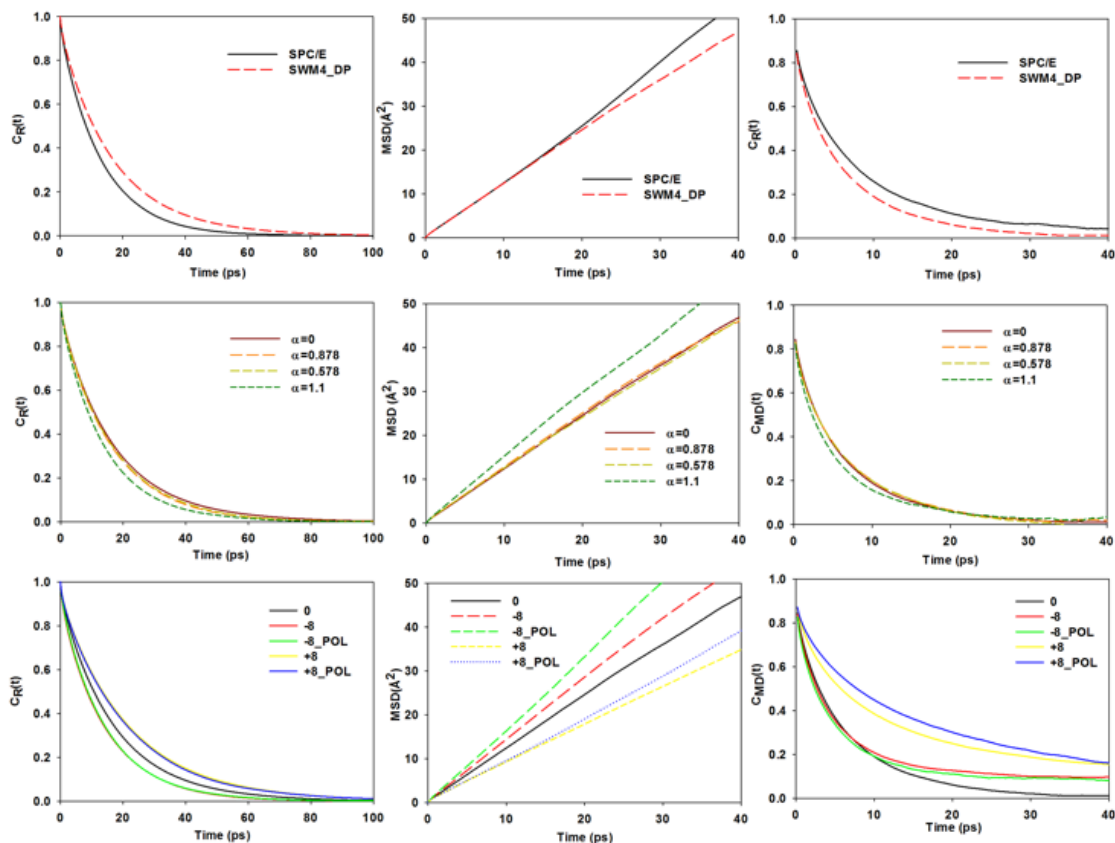
Figure B.6. Residence auto-correlation function (left panels), mean square displacement as a function of time (middle panels), and reorientation correlation function (right panels) for interfacial water on graphene surfaces. Top, middle, and bottom panels are for the results for SPC/E and SWM4_DP water on neutral non-polarizable graphene surface, SWM4_DP water on neutral graphene as a function of graphene polarizability, and SWM4_DP water on charged graphene, polarizable and non-polarizable, respectively.

B.5 Conclusions

The importance of including the polarizablity of water and graphene in molecular dynamics simulation of the water/graphene system was explored. A thin film of rigid SPC/E and polarizable SWM4_DP water on non-polarizable and polarizable graphene surfaces was simulated. The graphene surface was either maintained neutral or charged. The obtained results suggest that the SPC/E and SWM4_DP yield

very similar structural properties of water on neutral non-polarizable graphene, while the dynamical properties of SPC/E and SWM4_DP on neutral non-polarizable graphene are slightly different. More importantly, I found that including explicitly in the calculations the polarizability of graphene enhances the number of interfacial SWM4_DP water molecules pointing one of their OH bonds toward the surface, although it insignificantly affects the dynamical properties of interfacial SWM4_DP water if the polarizability of carbon is smaller than $\alpha = 0.878Å$. On charged graphene surfaces, the effect of polarizability of grahene on the structural properties and some of the dynamical properties of SWM4_DP water is negligible because the electrostatic forces dominate the polarization forces, as expected. For all cases, the hydrogen bond network is insensitive to the polarizability of both water and graphene. These results, when accompanied by experimental data, will provide a comprehensive picture of water properties and insight into the importance of polarization at graphene/water interface. Applications that will benefit from this fundamental understanding include the design of energy storage devices as well as water desalination processes.

Appendix C   Integration of the Poisson Equation

The Poisson equation reads (the symbols are explained in the Chapter 4):

$$\frac{d^2\psi}{dz^2} = \frac{-1}{\varepsilon_o}\rho(z) \tag{C.1}$$

The first and second integrations with respect to the variable z, the distance from the charged surface, yield:

$$\frac{d\psi}{dz}(z) = \frac{-1}{\varepsilon_o}\int_0^z \rho(u)du + C_1 \tag{C.2}$$

$$\psi_z = \frac{-1}{\varepsilon_o}\int_0^z \int_0^s \rho(u)du\,ds + C_1 z + C_2 \tag{C.3}$$

In Eqs. (C.2) and (C.3) u and s are dummy variables, C_1 and C_2 are constants of integration that are defined by imposing appropriate boundary conditions.

As the the first boundary condition, I impose that

$\frac{d\psi}{dz} = 0 \ at \ z = R/2$ (i.e., the electric field at the pore centre is zero), which yields

$$C_1 = \frac{1}{\varepsilon_o}\int_0^{R/2} \rho(u)du.$$

As the second boundary condition I impose $\psi(z) = 0 \ at \ z = 0$

(i.e., the potential is chosen to be zero at z = 0), which for all electrochemical cells yields

$$C_2 = 0.$$

The last equality implies that all electrical potentials shown in this work as expressed relative to the potential of the electrode at z=0.

Using the relations just derived for C_1 and C_2, Eq. (C.3) becomes

$$\psi_z = \frac{-1}{\varepsilon_o} \int_0^z \int_0^s \rho(u)du\, ds + \left[\frac{1}{\varepsilon_o} \int_0^{R/2} \rho(u)du\right] z \tag{C.4}$$

From Eq. (C.4) I switch the order of integration within the double integrals to obtain

$$\psi_z = \frac{-1}{\varepsilon_o} \left[\int_0^z \int_u^z \rho(u)ds\, du - \left(\int_0^{R/2} \rho(u)du\right) z\right] \tag{C.5}$$

and subsequently

$$\psi_z = \frac{-1}{\varepsilon_o} \left[\int_0^z (z-u)\rho(u)du - \left(\int_0^{R/2} \rho(u)du\right) z\right] \tag{C.6}$$

The results presented in Figure 4.4 and Figure 4.6 are obtained by numerical integration of Eq. (C.6) using the respective charge density profiles as input.

Bibliography

1.   Duan C, Wang W, & Xie Q (2013) Review article: Fabrication of nanofluidic devices. *Biomicrofluidics* 7(2):026501.

2.   Sparreboom W, van den Berg A, & Eijkel JCT (2009) Principles and applications of nanofluidic transport. *Nat Nano* 4(11):713-720.

3.   Yang SC (2006) Effects of surface roughness and interface wettability on nanoscale flow in a nanochannel. *Microfluid Nanofluid* 2(6):501-511.

4.   Neto C, Evans DR, Bonaccurso E, Butt HJ, & Craig VSJ (2005) Boundary slip in Newtonian liquids: a review of experimental studies. *Reports on Progress in Physics* 68(12):2859-2898.

5.   Karnik R, Castelino K, Duan CH, & Majumdar A (2006) Diffusion-limited patterning of molecules in nanofluidic channels. *Nano Letters* 6(8):1735-1740.

6.   Stein D, Kruithof M, & Dekker C (2004) Surface-Charge-Governed Ion Transport in Nanofluidic Channels. *Phys Rev Lett* 93(3):035901.

7.   Chang HC & Yossifon G (2009) Understanding electrokinetics at the nanoscale: A perspective. *Biomicrofluidics* 3(1):012001.

8.   Berezhkovskii A & Hummer G (2002) Single-file transport of water molecules through a carbon nanotube. *Phys Rev Lett* 89(6):064503.

9.   Eijkel JCT & van den Berg A (2005) Nanofluidics: what is it and what can we expect from it? *Microfluid Nanofluid* 1(3):249-267.

10.   Sparreboom W, van den Berg A, & Eijkel JCT (2010) Transport in nanofluidic systems: a review of theory and applications. *New J Phys* 12:015004.

11.   Thomas M, Corry B, & Hilder TA (2014) What Have We Learnt About the Mechanisms of Rapid Water Transport, Ion Rejection and Selectivity in Nanopores from Molecular Simulation? *Small* 10(8):1453-1465.

12.   Cottin-Bizonne C, Cross B, Steinberger A, & Charlaix E (2005) Boundary slip on smooth hydrophobic surfaces: intrinsic effects and possible artifacts. *Phys Rev Lett* 94(5):056102-056102.

13.   Ho TA, Papavassiliou DV, Lee LL, & Striolo A (2011) Liquid water can slip on a hydrophilic surface. *P Natl Acad Sci USA* 108(39):16170-16175.

14.   Huang DM, Sendner C, Horinek D, Netz RR, & Bocquet L (2008) Water slippage versus contact angle: a quasiuniversal relationship. *Phys Rev Lett* 101(22):226101.

15.   Kannam SK, Todd BD, Hansen JS, & Daivis PJ (2011) Slip flow in graphene nanochannels. *J Chem Phys* 135(14):144701.

16.   Kannam SK, Todd BD, Hansen JS, & Daivis PJ (2012) Slip length of water on graphene: Limitations of non-equilibrium molecular dynamics simulations. *J Chem Phys* 136(2):024705 -024713.

17.   Maali A, Cohen-Bouhacina T, & Kellay H (2008) Measurement of the slip length of water flow on graphite surface. *Appl Phys Lett* 92(5):053101.

18.   Martini A, Hsu H-Y, Patankar NA, & Lichter S (2008) Slip at high shear rates. *Phys Rev Lett* 100(20):206001-206001.

19.   Martini A, Roxin A, Snurr RQ, Wang Q, & Lichter S (2008) Molecular mechanisms of liquid slip. *Journal of Fluid Mechanics* 600(1):257.

20.   Zhu Y & Granick S (2001) Rate-dependent slip of Newtonian liquid at smooth surfaces. *Phys Rev Lett* 87(9):096105.

21.   Lauga E, MP B, & HA S (2007) *Handbook of Experimental Fluid Dynamics* (Springer, New York).

22.   Craig VSJ, Neto C, & Williams DRM (2001) Shear-dependent boundary slip in an aqueous Newtonian liquid. *Phys Rev Lett* 87(5):054504.

23.   Barrat JL & Bocquet L (1999) Large slip effect at a nonwetting fluid-solid interface. *Phys Rev Lett* 82(23):4671-4674.

24.   Kannam SK, Todd BD, Hansen JS, & Daivis PJ (2013) How fast does water flow in carbon nanotubes? *J Chem Phys* 138(9):094701.

25.   Whitby M, Cagnon L, Thanou M, & Quirke N (2008) Enhanced fluid flow through nanoscale carbon pipes. *Nano Letters* 8(9):2632-2637.

26.   Majumder M, Chopra N, Andrews R, & Hinds BJ (2005) Nanoscale hydrodynamics: Enhanced flow in carbon nanotubes *Nature* 438(7070):44.

27.   Holt JK*, et al.* (2006) Fast mass transport through sub-2-nanometer carbon nanotubes. *Science* 312(5776):1034-1037.

28.   Thomas JA, McGaughey AJH, & Kuter-Arnebeck O (2010) Pressure-driven water flow through carbon nanotubes: Insights from molecular dynamics simulation. *Int J Therm Sci* 49(2):281-289.

29.   Koumoutsakos P, Jaffe RL, Werder T, & Walther JH (2003) On the validity of the no-slip condition in nanofluidics. *Nanotech 2003, Vol 1*:148-151.

30.   Gu XK & Chen M (2011) Shape dependence of slip length on patterned hydrophobic surfaces. *Appl Phys Lett* 99(6):063101.

31.   Hummer G, Rasaiah JC, & Noworyta JP (2001) Water conduction through the hydrophobic channel of a carbon nanotube. *Nature* 414(6860):188-190.

32.   Suk ME & Aluru NR (2010) Water Transport through Ultrathin Graphene. *J Phys Chem Lett* 1(10):1590-1594.

33.   Fornasiero F*, et al.* (2008) Ion exclusion by sub-2-nm carbon nanotube pores. *P Natl Acad Sci USA* 105(45):17250-17255.

34.   Corry B (2008) Designing carbon nanotube membranes for efficient water desalination. *J Phys Chem B* 112(5):1427-1434.

35.   Cohen-Tanugi D & Grossman JC (2012) Water Desalination across Nanoporous Graphene. *Nano Letters* 12(7):3602-3608.

36.   Joly L, Ybert C, Trizac E, & Bocquet L (2004) Hydrodynamics within the electric double layer on slipping surfaces. *Phys Rev Lett* 93(25):257805.

37.   Castrillon SRV, Giovambattista N, Aksay IA, & Debenedetti PG (2009) Effect of Surface Polarity on the Structure and Dynamics of Water in Nanoscale Confinement. *J Phys Chem B* 113(5):1438-1446.

38.   Gordillo MC & Marti J (2008) Structure of water adsorbed on a single graphene sheet. *Phys Rev B* 78(7):075432.

39.   Argyris D, Tummala NR, Striolo A, & Cole DR (2008) Molecular structure and dynamics in thin water films at the silica and graphite surfaces. *J Phys Chem C* 112(35):13587-13599.

40.   Argyris D, Cole DR, & Striolo A (2009) Hydration Structure on Crystalline Silica Substrates. *Langmuir* 25(14):8025-8035.

41.   Wang JW, Kalinichev AG, & Kirkpatrick RJ (2009) Asymmetric Hydrogen Bonding and Orientational Ordering of Water at Hydrophobic and Hydrophilic Surfaces: A Comparison of Water/Vapor, Water/Talc, and Water/Mica Interfaces. *J Phys Chem C* 113(25):11077-11085.

42.   Van der Spoel D*, et al.* (2005) GROMACS: Fast, flexible, and free. *J Comput Chem* 26(16):1701-1718.

43.   Plimpton S (1995) Fast Parallel Algorithms for Short-Range Molecular-Dynamics. *J Comput Phys* 117(1):1-19.

44.   Berendsen HJC, Postma JPM, Van Gunsteren WF, & Hermans J (1981) *Intermolecular Forces* (Reidel, Dordrecht).

45.   Berendsen HJC, Grigera JR, & Straatsma TP (1987) The Missing Term in Effective Pair Potentials. *Journal of Physical Chemistry* 91(24):6269-6271.

46.   Abascal JLF & Vega C (2005) A general purpose model for the condensed phases of water: TIP4P/2005. *J Chem Phys* 123(23):234505-234016.

47.   Jorgensen WL, Chandrasekhar J, Madura JD, Impey RW, & Klein ML (1983) Comparison of Simple Potential Functions for Simulating Liquid Water. *J Chem Phys* 79(2):926-935.

48.   Mahoney MW & Jorgensen WL (2000) A five-site model for liquid water and the reproduction of the density anomaly by rigid, nonpolarizable potential functions. *J Chem Phys* 112(20):8910-8922.

49.   Gonzalez MA & Abascal JLF (2011) A flexible model for water based on TIP4P/2005. *J Chem Phys* 135(22):224516-224523.

50.   Lamoureux G, Harder E, Vorobyov IV, Roux B, & MacKerell AD (2006) A polarizable model of water for molecular dynamics simulations of biomolecules. *Chemical Physics Letters* 418(1-3):245-249.

51.   Ryckaert J-P, Ciccotti G, & Berendsen H (1977) Numerical integration of the cartesian equations of motion of a system with constraints: molecular dynamics of n-alkanes. *J Comput Phys* 23(3):327-341.

52.   Mark P & Nilsson L (2001) Structure and dynamics of the TIP3P, SPC, and SPC/E water models at 298 K. *J Phys Chem A* 105(43):9954-9960.

53.   Pusztai L, Pizio O, & Sokolowski S (2008) Comparison of interaction potentials of liquid water with respect to their consistency with neutron diffraction data of pure heavy water. *J Chem Phys* 129(18):184103.

54.   Krynicki K, Green CD, & Sawyer DW (1978) Pressure and Temperature-Dependence of Self-Diffusion in Water. *Faraday Discuss* 66:199-208.

55.   Mahoney MW & Jorgensen WL (2001) Diffusion constant of the TIP5P model of liquid water. *J Chem Phys* 114(1):363-366.

56.   Vega C & Abascal JLF (2011) Simulating water with rigid non-polarizable models: a general perspective. *Phys Chem Chem Phys* 13(44):19663-19688.

57.   Ho TA*, et al.* (2011) Interfacial water on crystalline silica: a comparative molecular dynamics simulation study. *Molecular Simulation* 37(3):172-195.

58.   Basconi JE & Shirts MR (2013) Effects of Temperature Control Algorithms on Transport Properties and Kinetics in Molecular Dynamics Simulations. *J Chem Theory Comput* 9(7):2887-2899.

59.   Thompson PA & Troian SM (1997) A general boundary condition for liquid flow at solid surfaces. *Nature* 389(6649):360.

60.   Whitby M & Quirke N (2007) Fluid flow in carbon nanotubes and nanopipes. *Nat Nanotechnol* 2(2):87-94.

61.   Toton D, Lorenz CD, Rompotis N, Martsinovich N, & Kantorovich L (2010) Temperature control in molecular dynamic simulations of non-equilibrium processes. *J Phys-Condens Mat* 22(7):074205.

62.   Zhu W, Singer SJ, Zheng Z, & Conlisk AT (2005) Electro-osmotic flow of a model electrolyte. *Phys Rev E* 71(4):041501.

63.   Freund JB (2002) Electro-osmosis in a nanometer-scale channel studied by atomistic simulation. *J Chem Phys* 116(5):2194-2200.

64.   Qiao R & Aluru NR (2003) Ion concentrations and velocity profiles in nanochannel electroosmotic flows. *J Chem Phys* 118(10):4692-4701.

65.   Khare R, de Pablo J, & Yethiraj A (1997) Molecular simulation and continuum mechanics study of simple fluids in non-isothermal planar couette flows. *The Journal of Chemical Physics* 107(7):2589-2596.

66.   Giovambattista N, Debenedetti PG, & Rossky PJ (2009) Enhanced surface hydrophobicity by coupling of surface polarity and topography. *P Natl Acad Sci USA* 106(36):15181-15185.

67.   Israelachvili JN (1991) *Intermolecular and Surface Forces* (Academic Press, London) 2 Ed.

68.   Striolo A (2006) The mechanism of water diffusion in narrow carbon nanotubes. *Nano Letters* 6(4):633-639.

69.   Kalra A, Garde S, & Hummer G (2003) Osmotic water transport through carbon nanotube membranes. *Proceedings of the National Academy of Sciences of the United States of America* 100(18):10175-10180.

70.   Holt JK*, et al.* (2006) Fast Mass Transport Through Sub-2-Nanometer Carbon Nanotubes. *Science* 312(5776):1034.

71.   Granick S & Bae SC (2008) Chemistry. A curious antipathy for water. *Science* 322(5907):1477-1478.

72.   Chandler D (2005) Interfaces and the driving force of hydrophobic assembly. *Nature* 437(7059):640.

73.   Castrillón SR-V, Giovambattista Ns, Aksay IA, & Debenedetti PG (2009) Effect of Surface Polarity on the Structure and Dynamics of Water in Nanoscale Confinement. *J Phys Chem B* 113(5):1438-1446.

74.   Jamadagni SN, Godawat R, & Garde S (2009) How Surface Wettability Affects the Binding, Folding, and Dynamics of Hydrophobic Polymers at Interfaces. *Langmuir* 25(22):13092-13099.

75.   Godawat R, Jamadagni SN, & Garde S (2009) Characterizing hydrophobicity of interfaces by using cavity formation, solute binding, and water correlations. *P Natl Acad Sci USA* 106(36):15119-15124.

76. Barrat J-L & Bocquet L (1999) Influence of wetting properties on hydrodynamic boundary conditions at a fluid/solid interface. *Faraday Discuss* 112:119-128.

77. Zhu Y & Granick S (2002) Limits of the hydrodynamic no-slip boundary condition. *Phys Rev Lett* 88(10):106102-106102.

78. Niavarani A & Priezjev NV (2010) Modeling the combined effect of surface roughness and shear rate on slip flow of simple fluids. *Phys Rev E* 81(1):011606.

79. Balasubramanian AK, Miller AC, & Rediniotis OK (2004) Microstructured hydrophobic skin for hydrodynamic drag reduction. *Aiaa J* 42(2):411-414.

80. Rothstein JP (2010) Slip on Superhydrophobic Surfaces. *Annu Rev Fluid Mech* 42:89-109.

81. Koishi T, Yasuoka K, Fujikawa S, Ebisuzaki T, & Zeng XC (2009) Coexistence and transition between Cassie and Wenzel state on pillared hydrophobic surface. *P Natl Acad Sci USA* 106(21):8435-8440.

82. Li XM, Reinhoudt D, & Crego-Calama M (2007) What do we need for a superhydrophobic surface? A review on the recent progress in the preparation of superhydrophobic surfaces. *Chem Soc Rev* 36(9):1529-1529.

83. Truesdell R, Mammoli A, Vorobieff P, van Swol F, & Brinker CJ (2006) Drag reduction on a patterned superhydrophobic surface. *Phys Rev Lett* 97(4):0044505.

84. Voronov RS, Papavassiliou DV, & Lee LL (2008) Review of Fluid Slip over Superhydrophobic Surfaces and Its Dependence on the Contact Angle. *Industrial & Engineering Chemistry Research* 47(8):2455-2477.

85. Argyris D, Rajesh Tummala N, R. Cole D, & Striolo A (2008) Molecular Structure and Dynamics in Thin Water Films at the Silica and Graphite Surfaces. *The Journal of Physical Chemistry C* 112(35):13587.

86. Kalra A, Garde S, & Hummer G (2010) Lubrication by molecularly thin water films confined between nanostructured membranes. *European Physical Journal Special Topics* 189:147-154.

87.   Pit R, Hervet H, & Léger L (2000) Direct Experimental Evidence of Slip in Hexadecane: Solid Interfaces. *Phys Rev Lett* 85(5):980.

88.   Gao L & McCarthy TJ (2008) Teflon is Hydrophilic. Comments on Definitions of Hydrophobic, Shear versus Tensile Hydrophobicity, and Wettability Characterization. *Langmuir* 24(17):9183-9188.

89.   Cygan RT, Liang JJ, & Kalinichev AG (2004) Molecular models of hydroxide, oxyhydroxide, and clay phases and the development of a general force field. *J Phys Chem B* 108(4):1255-1266.

90.   Peng XD & Barteau MA (1990) Characterization of oxide layers on Mg(0001) and comparison of H2O adsorption on surface and bulk oxides. *Surface Science* 233(3):283-292.

91.   Karolewski MA & Cavell RG (1992) Coadsorption of cesium and water on MgO(100). *Surface Science* 271(1–2):128-138.

92.   Wu MC, Estrada CA, Corneille JS, & Goodman DW (1992) Model surface studies of metal oxides: Adsorption of water and methanol on ultrathin MgO films on Mo(100). *The Journal of Chemical Physics* 96(5):3892-3900.

93.   Giovambattista N, Debenedetti PG, & Rossky PJ (2007) Effect of Surface Polarity on Water Contact Angle and Interfacial Hydration Structure. *J Phys Chem B* 111(32):9581-9587.

94.   Lee SH & Rossky PJ (1994) A comparison of the structure and dynamics of liquid water at hydrophobic and hydrophilic surfaces: a molecular dynamics simulation study. *The Journal of Chemical Physics* 100(4):3334-3345.

95.   Cieplak M, Koplik J, & Banavar JR (2001) Boundary Conditions at a Fluid-Solid Interface. *Phys Rev Lett* 86(5):803.

96.   Falk K, Sedlmeier F, Joly L, Netz RR, & Bocquet L (2010) Molecular Origin of Fast Water Transport in Carbon Nanotube Membranes: Superlubricity versus Curvature Dependent Friction. *Nano Letters* 10(10):4067-4073.

97.   Voronov RS, Papavassiliou DV, & Lee LL (2007) Slip length and contact angle over hydrophobic surfaces. *Chemical Physics Letters* 441(4-6):273-276.

98.   Priezjev NV (2007) Rate-dependent slip boundary conditions for simple fluids. *Phys Rev E* 75(5):051605.

99.   Ulmanella U & Ho CM (2008) Molecular effects on boundary condition in micro/nanoliquid flows. *Phys Fluids* 20(10):101512.

100.   Shannon MA*, et al.* (2008) Science and technology for water purification in the coming decades. *Nature* 452(7185):301-310.

101.   Tour JM, Kittrell C, & Colvin VL (2010) Green carbon as a bridge to renewable energy. *Nat Mater* 9(11):871-874.

102.   Anderson MA, Cudero AL, & Palma J (2010) Capacitive deionization as an electrochemical means of saving energy and delivering clean water. Comparison to present desalination practices: Will it compete? *Electrochim Acta* 55(12):3845-3856.

103.   Miller JR & Simon P (2008) Materials science - Electrochemical capacitors for energy management. *Science* 321(5889):651-652.

104.   Helmholtz H (1853) Ueber einige Gesetze der Vertheilung elektrischer Ströme in körperlichen Leitern mit Anwendung auf die thierisch-elektrischen Versuche. *Annalen der Physik* 165(6):211-233.

105.   Bard A & Fraulkner L (2001) *Electrochemical Methods: Fundamentals and Applications* (John Wiley & Son, New York).

106.   Butt HJ & Kappl M (2010) *Surface and Interfacial Forces* (Wiley-VCH: Weinheim, Germany).

107.   Huang JS, Qiao R, Sumpter BG, & Meunier V (2010) Effect of diffuse layer and pore shapes in mesoporous carbon supercapacitors. *J Mater Res* 25(8):1469-1475.

108.   Schmickler W (1996) Electronic effects in the electric double layer. *Chem Rev* 96(8):3177-3200.

109.   Gouy (1909) On the constitution of the electric charge at the surface of an electrolyte. *Cr Hebd Acad Sci* 149:654-657.

110.   Chapman DL (1913) A Contribution to the Theory of Electrocapillarity. *Philos Mag* 25(148):475-481.

111.   Israelachvili J (1991) *Intermolecular & Surface Forces* (Academic Press, New York) second Ed.

112.   Stern O (1924) The theory of the electrolytic double shift. *Z Elktrochem Angew P* 30:508-516.

113.   Wang HN & Pilon L (2011) Accurate Simulations of Electric Double Layer Capacitance of Ultramicroelectrodes. *J Phys Chem C* 115(33):16711-16719.

114.   Zhao R, Biesheuvel PM, Miedema H, Bruning H, & van der Wal A (2010) Charge Efficiency: A Functional Tool to Probe the Double-Layer Structure Inside of Porous Electrodes and Application in the Modeling of Capacitive Deionization. *J Phys Chem Lett* 1(1):205-210.

115.   Porada S, Zhao R, van der Wal A, Presser V, & Biesheuvel PM (2013) Review on the science and technology of water desalination by capacitive deionization. *Progress in Materials Science* 58(8):1388-1442.

116.   Chmiola J*, et al.* (2006) Anomalous increase in carbon capacitance at pore sizes less than 1 nanometer. *Science* 313(5794):1760-1763.

117.   Largeot C*, et al.* (2008) Relation between the ion size and pore size for an electric double-layer capacitor. *J Am Chem Soc* 130(9):2730-2731.

118.   Fedorov MV & Kornyshev AA (2008) Ionic liquid near a charged wall: structure and capacitance of electrical double layer. *J Phys Chem B* 112(38):11868-11872.

119.   Vatamanu J, Borodin O, & Smith GD (2010) Molecular Insights into the Potential and Temperature Dependences of the Differential Capacitance of a Room-Temperature Ionic Liquid at Graphite Electrodes. *J Am Chem Soc* 132(42):14825-14833.

120.   Shim Y, Kim HJ, & Jung Y (2012) Graphene-based supercapacitors in the parallel-plate electrode configuration: Ionic liquids versus organic electrolytes. *Faraday Discuss* 154:249-263.

121.   Konatham D, Yu J, Ho TA, & Striolo A (2013) Simulation Insights for Graphene-Based Water Desalination Membranes. *Langmuir* 29(38):11884-11897.

122.   O'Hern SC*, et al.* (2014) Selective Ionic Transport through Tunable Subnanometer Pores in Single-Layer Graphene Membranes. *Nano Letters*:234–1241.

123.   Garaj S, Liu S, Golovchenko JA, & Branton D (2013) Molecule-hugging graphene nanopores. *P Natl Acad Sci USA* 110(30):12192-12196.

124.   Koenig SP, Wang LD, Pellegrino J, & Bunch JS (2012) Selective molecular sieving through porous graphene. *Nat Nanotechnol* 7(11):728-732.

125.   Giovambattista N, Rossky PJ, & Debenedetti PG (2006) Effect of pressure on the phase behavior and structure of water confined between nanoscale hydrophobic and hydrophilic plates. *Phys Rev E* 73(4):041604.

126.   Huang HB*, et al.* (2013) Ultrafast viscous water flow through nanostrand-channelled graphene oxide membranes. *Nat Commun* 4:2979.

127.   Merlet C*, et al.* (2012) On the molecular origin of supercapacitance in nanoporous carbon electrodes. *Nat Mater* 11(4):306-310.

128.   Merlet C*, et al.* (2013) Simulating Supercapacitors: Can We Model Electrodes As Constant Charge Surfaces? *J Phys Chem Lett* 4(2):264-268.

129.   Ho TA & Striolo A (2013) Polarizability effects in molecular dynamics simulations of the graphene-water interface. *J Chem Phys* 138(5):054117.

130.   Cheng A & Steele WA (1990) Computer-Simulation of Ammonia on Graphite .1. Low-Temperature Structure of Monolayer and Bilayer Films. *J Chem Phys* 92(6):3858-3866.

131.   Ho TA & Striolo A (2014) Molecular dynamics simulation of the graphene-water interface: comparing water models. *Molecular Simulation* 40(14):1190-1200.

132.   Dang LX (1995) Mechanism and Thermodynamics of Ion Selectivity in Aqueous-Solutions of 18-Crown-6 Ether - a Molecular-Dynamics Study. *J Am Chem Soc* 117(26):6954-6960.

133.   Levin Y (2009) Polarizable Ions at Interfaces. *Phys Rev Lett* 102(14):147803.

134.   Huang JY*, et al.* (2013) Nanowire liquid pumps. *Nat Nanotechnol* 8(4):277-281.

135. Jungwirth P & Tobias DJ (2002) Ions at the air/water interface. *J Phys Chem B* 106(25):6361-6373.

136. Gong XJ*, et al.* (2008) Enhancement of Water Permeation across a Nanochannel by the Structure outside the Channel. *Phys Rev Lett* 101(25):257801.

137. Smith DE & Dang LX (1994) Computer-Simulations of Nacl Association in Polarizable Water. *J Chem Phys* 100(5):3757-3766.

138. Yang L, Fishbine BH, Migliori A, & Pratt LR (2009) Molecular Simulation of Electric Double-Layer Capacitors Based on Carbon Nanotube Forests. *J Am Chem Soc* 131(34):12373-12376.

139. Shim Y & Kim HJ (2010) Nanoporous Carbon Supercapacitors in an Ionic Liquid: A Computer Simulation Study. *Acs Nano* 4(4):2345-2355.

140. Suss ME*, et al.* (2012) Capacitive desalination with flow-through electrodes. *Energ Environ Sci* 5(11):9511-9519.

141. Porada S, Sales BB, Hamelers HVM, & Biesheuvel PM (2012) Water Desalination with Wires. *J Phys Chem Lett* 3(12):1613-1618.

142. Kalluri RK, Konatham D, & Striolo A (2011) Aqueous NaCl Solutions within Charged Carbon-Slit Pores: Partition Coefficients and Density Distributions from Molecular Dynamics Simulations. *J Phys Chem C* 115(28):13786-13795.

143. Pendergast MM & Hoek EMV (2011) A review of water treatment membrane nanotechnologies. *Energ Environ Sci* 4(6):1946-1971.

144. Christen K (2006) Desalination technology could clean up wastewater from coal-bed methane production. *Environmental Science & Technology* 40(3):639-639.

145. Welgemoed TJ & Schutte CF (2005) Capacitive Deionization Technology™: An alternative desalination solution. *Desalination* 183(1-3):327-340.

146. Hughes JD (2013) A reality check on the shale revolution. *Nature* 494(7437):307-308.

147. Cipolla CL, Lolon E, & Mayerhofer MJ (2009) *Reservoir Modeling and Production Evaluation in Shale-Gas Reservoirs* (International Petroleum Technology Conference).

148.   Yethiraj A & Striolo A (2013) Fracking: What Can Physical Chemistry Offer? *The Journal of Physical Chemistry Letters* 4(4):687-690.

149.   Wu QH*, et al.* (2014) Optic Imaging of Two-Phase-Flow Behavior in 1D Nanoscale Channels. *Spe J* 19(5):793-802.

150.   Silin D & Kneafsey TJ (2011) Gas Shale: From Nanometer-scale Observations to Well Modelling. *Canadian Society for Unconventional Gas* CSUG/SPE 149489.

151.   Joekar-Niasar V & Hassanizadeh SM (2012) Analysis of Fundamentals of Two-Phase Flow in Porous Media Using Dynamic Pore-Network Models: A Review. *Crit Rev Env Sci Tec* 42(18):1895-1976.

152.   Shao N, Gavriilidis A, & Angeli P (2009) Flow regimes for adiabatic gas–liquid flow in microchannels. *Chemical Engineering Science* 64(11):2749-2761.

153.   Wu Q*, et al.* (2013) Optic imaging of single and two-phase pressure-driven flows in nano-scale channels. *Lab on a Chip* 13(6):1165-1171.

154.   Tanikawa W & Shimamoto T (2009) Comparison of Klinkenberg-corrected gas permeability and water permeability in sedimentary rocks. *Int J Rock Mech Min* 46(2):229-238.

155.   Ahmadlouydarab M, Liu Z-S, & Feng JJ (2012) Relative permeability for two-phase flow through corrugated tubes as model porous media. *International Journal of Multiphase Flow* 47(0):85-93.

156.   Muskat M & Meres MW (1936) The Flow of Heterogeneous Fluids Through Porous Media. *Journal of Applied Physics* 7(9):346-363.

157.   Ahmadlouydarab M, Liu Z-S, & Feng JJ (2011) Interfacial flows in corrugated microchannels: Flow regimes, transitions and hysteresis. *International Journal of Multiphase Flow* 37(10):1266-1276.

158.   Niessner J, Berg S, & Hassanizadeh SM (2011) Comparison of Two-Phase Darcy's Law with a Thermodynamically Consistent Approach. *Transp Porous Med* 88(1):133-148.

159. Indraratna B & Ranjith P (2001) Laboratory Measurement of Two-Phase Flow Parameters in Rock Joints Based on High Pressure Triaxial Testing. *Journal of Geotechnical and Geoenvironmental Engineering* 127(6):530-542.

160. Ranjith PG, Choi SK, & Fourar M (2006) Characterization of two-phase flow in a single rock joint. *Int J Rock Mech Min* 43(2):216-223.

161. Wang J, Kalinichev AG, Kirkpatrick RJ, & Cygan RT (2005) Structure, Energetics, and Dynamics of Water Adsorbed on the Muscovite (001) Surface: A Molecular Dynamics Simulation. *The Journal of Physical Chemistry B* 109(33):15893-15905.

162. White WM (2013) *Geochemistry* (John Wiley $Sons, Oxford, UK).

163. Pevear DR (1999) Illite and hydrocarbon exploration. *P Natl Acad Sci USA* 96(7):3440-3446.

164. Tian Y & Ayers WB (2010) Barnett Shale (Mississippian), Fort Worth Basin, Texas: Regional Variations in Gas and Oil Production and Reservoir Properties. in *Society of Petroleum Engineers* (Society of Petroleum Engineers).

165. Blatt H, Tracy R, & Owens B (1996) *Petrology: Igneous, Sedimentary and Metamorphic* (Freeman).

166. Wang JW, Kalinichev AG, Kirkpatrick RJ, & Cygan RT (2005) Structure, energetics, and dynamics of water adsorbed on the muscovite (001) surface: A molecular dynamics simulation. *J Phys Chem B* 109(33):15893-15905.

167. Teich-McGoldrick SL, Greathouse JA, & Cygan RT (2012) Molecular Dynamics Simulations of Structural and Mechanical Properties of Muscovite: Pressure and Temperature Effects. *J Phys Chem C* 116(28):15099-15107.

168. Teich-McGoldrick SL, Greathouse JA, & Cygan RT (2012) Molecular Dynamics Simulations of Structural and Mechanical Properties of Muscovite: Pressure and Temperature Effects. *The Journal of Physical Chemistry C* 116(28):15099-15107.

169. Martin MG & Siepmann JI (1998) Transferable potentials for phase equilibria. 1. United-atom description of n-alkanes. *J Phys Chem B* 102(14):2569-2577.

170.   Nara Y, Meredith PG, Yoneda T, & Kaneko K (2011) Influence of macro-fractures and micro-fractures on permeability and elastic wave velocities in basalt at elevated pressure. *Tectonophysics* 503(1-2):52-59.

171.   Tanikawa W & Shimamoto T (2009) comparison of Klinkenberg-corrected gas permeability and water permeability in sedimentary rocks (vol 46, pg 229, 2009). *Int J Rock Mech Min* 46(8):1394-1395.

172.   Ho TA, Argyris D, Cole DR, & Striolo A (2012) Aqueous NaCl and CsCl Solutions Confined in Crystalline Slit-Shaped Silica Nanopores of Varying Degree of Protonation. *Langmuir* 28(2):1256-1266.

173.   Docherty SY, Nicholls WD, Borg MK, Lockerby DA, & Reese JM (2014) Boundary conditions for molecular dynamics simulations of water transport through nanotubes. *Proceedings of the Institution of Mechanical Engineers, Part C: Journal of Mechanical Engineering Science* 228(1):186-195.

174.   Joseph S & Aluru NR (2008) Why Are Carbon Nanotubes Fast Transporters of Water? *Nano Letters* 8(2):452-458.

175.   Koplik J, Banavar JR, & Willemsen JF (1988) Molecular dynamics of Poiseuille flow and moving contact lines. *Phys Rev Lett* 60(13):1282-1285.

176.   Wang L, Dumont RS, & Dickson JM (2013) Nonequilibrium molecular dynamics simulation of pressure-driven water transport through modified CNT membranes. *The Journal of Chemical Physics* 138(12):124701.

177.   Rebrov EV (2010) Two-phase flow regimes in microchannels. *Theor Found Chem En+* 44(4):355-367.

178.   Tambach TJ, Hensen EJM, & Smit B (2004) Molecular simulations of swelling clay minerals. *J Phys Chem B* 108(23):7586-7596.

179.   Rao Q, Xiang Y, & Leng YS (2013) Molecular Simulations on the Structure and Dynamics of Water-Methane Fluids between Na-Montmorillonite Clay Surfaces at Elevated Temperature and Pressure. *J Phys Chem C* 117(27):14061-14069.

180.   Rafiee J, *et al.* (2012) Wetting transparency of graphene. *Nat Mater* 11(3):217-222.

181. Geim AK & Novoselov KS (2007) The rise of graphene. *Nat Mater* 6(3):183-191.

182. Geim AK (2009) Graphene: Status and Prospects. *Science* 324(5934):1530-1534.

183. Rafiee J*, et al.* (2012) Wetting transparency of graphene. *Nat Mater* 11(3):217-222.

184. Topsakal M, Sahin H, & Ciraci S (2012) Graphene coatings: An efficient protection from oxidation. *Phys Rev B* 85(15):155455-155461.

185. Simon P & Gogotsi Y (2008) Materials for electrochemical capacitors. *Nat Mater* 7(11):845-854.

186. Gao W*, et al.* (2011) Direct laser writing of micro-supercapacitors on hydrated graphite oxide films. *Nat Nanotechnol* 6(8):496-500.

187. El-Kady MF, Strong V, Dubin S, & Kaner RB (2012) Laser Scribing of High-Performance and Flexible Graphene-Based Electrochemical Capacitors. *Science* 335(6074):1326-1330.

188. Liu CG, Yu ZN, Neff D, Zhamu A, & Jang BZ (2010) Graphene-Based Supercapacitor with an Ultrahigh Energy Density. *Nano Letters* 10(12):4863-4868.

189. Artiles MS, Rout CS, & Fisher TS (2011) Graphene-based hybrid materials and devices for biosensing. *Advanced Drug Delivery Reviews* 63(14–15):1352-1360.

190. Machado BF & Serp P (2012) Graphene-based materials for catalysis. *Catalysis Science & Technology* 2(1):54-75.

191. Marti J, Nagy G, Guardia E, & Gordillo MC (2006) Molecular dynamics simulation of liquid water confined inside graphite channels: Dielectric and dynamical properties. *J Phys Chem B* 110(47):23987-23994.

192. Sala J, Guardia E, & Marti J (2012) Specific ion effects in aqueous eletrolyte solutions confined within graphene sheets at the nanometric scale. *Phys Chem Chem Phys* 14(30):10799-10808.

193. Striolo A, Chialvo AA, Cummings PT, & Gubbins KE (2003) Water adsorption in carbon-slit nanopores. *Langmuir* 19(20):8583-8591.

194. Liu JC & Monson PA (2005) Does water condense in carbon pores? *Langmuir* 21(22):10219-10225.

195. Ulberg DE & Gubbins KE (1995) Water-Adsorption in Microporous Graphitic Carbons. *Mol Phys* 84(6):1139-1153.

196. Striolo A (2011) From Interfacial Water to Macroscopic Observables: A Review. *Adsorpt Sci Technol* 29(3):211-258.

197. Marti J, Nagy G, Gordillo MC, & Guardia E (2006) Molecular simulation of liquid water confined inside graphite channels: Thermodynamics and structural properties. *J Chem Phys* 124(9):94703-94709.

198. Dang LX (1992) The Nonadditive Intermolecular Potential for Water Revised. *J Chem Phys* 97(4):2659-2660.

199. Kalluri RK, Ho TA, Biener MM, Biener J, & Striolo A (2013) Partition and Structure of Aqueous NaCl and CaCl2 Electrolytes in Carbon-Slit Electrodes. *J. Phys. Chem. C* 17(26):13609–13619.

200. Taherian F, Marcon V, van der Vegt NFA, & Leroy F (2013) What Is the Contact Angle of Water on Graphene? *Langmuir* 29(5):1457-1465.

201. Rana MK & Chandra A (2013) Ab initio and classical molecular dynamics studies of the structural and dynamical behavior of water near a hydrophobic graphene sheet. *The Journal of Chemical Physics* 138(20):204702.

202. Tocci G, Joly L, & Michaelides A (2014) Friction of Water on Graphene and Hexagonal Boron Nitride from Ab Initio Methods: Very Different Slippage Despite Very Similar Interface Structures. *Nano Letters* 14(12):6872-6877.

203. Cicero G, Grossman JC, Schwegler E, Gygi F, & Galli G (2008) Water confined in nanotubes and between graphene sheets: A first principle study. *J Am Chem Soc* 130(6):1871-1878.

204. Wu YJ, Tepper HL, & Voth GA (2006) Flexible simple point-charge water model with improved liquid-state properties. *J Chem Phys* 124(2):24503-24514.

205. Lamoureux G, MacKerell AD, & Roux B (2003) A simple polarizable model of water based on classical Drude oscillators. *J Chem Phys* 119(10):5185-5197.

206.   Bucher D & Kuyucak S (2008) Polarization of water in the first hydration shell of K+ and Ca2+ ions. *J Phys Chem B* 112(35):10786-10790.

207.   Picalek J, Minofar B, Kolafa J, & Jungwirth P (2008) Aqueous solutions of ionic liquids: study of the solution/vapor interface using molecular dynamics simulations. *Phys Chem Chem Phys* 10(37):5765-5775.

208.   Dang LX & Chang TM (2002) Molecular mechanism of ion binding to the liquid/vapor interface of water. *J Phys Chem B* 106(2):235-238.

209.   Stuart SJ & Berne BJ (1999) Surface curvature effects in the aqueous ionic solvation of the chloride ion. *J Phys Chem A* 103(49):10300-10307.

210.   Jungwirth P & Tobias DJ (2002) Ions at the Air/Water Interface. *The Journal of Physical Chemistry B* 106(25):6361-6373.

211.   Caleman C, Hub JS, van Maaren PJ, & van der Spoel D (2011) Atomistic simulation of ion solvation in water explains surface preference of halides. *P Natl Acad Sci USA* 108(17):6838-6842.

212.   Baer MD*, et al.* (2011) Re-examining the properties of the aqueous vapor-liquid interface using dispersion corrected density functional theory. *J Chem Phys* 135(12):124712-124719.

213.   Wu YB & Aluru NR (2013) Graphitic Carbon-Water Nonbonded Interaction Parameters. *J Phys Chem B* 117(29):8802-8813.

214.   Pertsin A & Grunze M (2004) Water-graphite interaction and behavior of water near the graphite surface. *J Phys Chem B* 108(4):1357-1364.

215.   Werder T, Walther JH, Jaffe RL, Halicioglu T, & Koumoutsakos P (2003) On the Water−Carbon Interaction for Use in Molecular Dynamics Simulations of Graphite and Carbon Nanotubes. *The Journal of Physical Chemistry B* 107(6):1345-1352.

216.   Feller D & Jordan KD (2000) Estimating the strength of the water/single-layer graphite interaction. *J Phys Chem A* 104(44):9971-9975.

217.   Scocchi G, Sergi D, D'Angelo C, & Ortona A (2011) Wetting and contact-line effects for spherical and cylindrical droplets on graphene layers: A comparative molecular-dynamics investigation. *Phys Rev E* 84(6):061602.

218.   Won CY, Joseph S, & Aluru NR (2006) Effect of quantum partial charges on the structure and dynamics of water in single-walled carbon nanotubes. *J Chem Phys* 125(11):114701.

219.   Jenness GR, Karalti O, & Jordan KD (2010) Benchmark calculations of water-acene interaction energies: Extrapolation to the water-graphene limit and assessment of dispersion-corrected DFT methods. *Phys Chem Chem Phys* 12(24):6375-6381.

220.   Schrader ME (1979) Ultrahigh-Vacuum Techniques in the Measurement of Contact Angles .5. Leed Study of the Effect of Structure on the Wettability of Graphite. *Abstr Pap Am Chem S* (Apr):77-77.

221.   Wang SR, Zhang Y, Abidi N, & Cabrales L (2009) Wettability and Surface Free Energy of Graphene Films. *Langmuir* 25(18):11078-11081.

222.   Fowkes FM & Harkins WD (1940) The state of monolayers adsorbed at the interface solid-aqueous solution. *J Am Chem Soc* 62:3377-3386.

223.   Ho TA & Striolo A (2012) Interfacial Water on Charged Graphene: Structure and Dynamics Predicted by Equilibrium Molecular Dynamics Simulations. *(in preparation)*.

224.   Ho TA & Striolo A (2013) Polarizability effects in molecular dynamics simulations of the graphene-water interface. *The Journal of Chemical Physics* 138(5):054117-054125.

225.   Marti J (1999) Analysis of the hydrogen bonding and vibrational spectra of supercritical model water by molecular dynamics simulations. *J Chem Phys* 110(14):6876-6886.

226.   Zielkiewicz J (2005) Structural properties of water: Comparison of the SPC, SPCE, TIP4P, and TIP5P models of water. *J Chem Phys* 123(10):104501-104506.

227.   Xu HF, Stern HA, & Berne BJ (2002) Can water polarizability be ignored in hydrogen bond kinetics? *J Phys Chem B* 106(8):2054-2060.

228.   Han SH, Kumar P, & Stanley HE (2009) Hydrogen-bond dynamics of water in a quasi-two-dimensional hydrophobic nanopore slit. *Phys Rev E* 79(4):041202.

229. Smith JD, *et al.* (2004) Energetics of hydrogen bond network rearrangements in liquid water. *Science* 306(5697):851-853.

230. Liu LM, Zhang CJ, Thornton G, & Michaelides A (2010) Structure and dynamics of liquid water on rutile TiO2(110). *Phys Rev B* 82(16): 161415.

231. Villegas-Jimenez A, Mucci A, & Whitehead MA (2009) Theoretical Insights into the Hydrated (10.4) Calcite Surface: Structure, Energetics, and Bonding Relationships. *Langmuir* 25(12):6813-6824.

232. Allen MP & Tildesley DJ (2004) *Computer Simulation of Liquids* (Oxford University Press, Oxford).

233. Jungwirth P & Tobias DJ (2006) Specific ion effects at the air/water interface. *Chem Rev* 106(4):1259-1281.

234. Horinek D & Netz RR (2007) Specific Ion Adsorption at Hydrophobic Solid Surfaces. *Phys Rev Lett* 99(22):226104.

235. Brown MA, *et al.* (2008) Ion spatial distributions at the liquid-vapor interface of aqueous potassium fluoride solutions. *Phys Chem Chem Phys* 10(32):4778-4784.

236. Perera L & Berkowitz ML (1991) Many-Body Effects in Molecular-Dynamics Simulations of Na+(H2o)N and Cl-(H2o)N Clusters. *J Chem Phys* 95(3):1954-1963.

237. Dang LX & Smith DE (1993) Molecular-Dynamics Simulations of Aqueous Ionic Clusters Using Polarizable Water. *J Chem Phys* 99(9):6950-6956.

238. Topsakal M, Şahin H, & Ciraci S (2012) Graphene coatings: An efficient protection from oxidation. *Phys Rev B* 85(15):155445.

239. Lamoureux G & Roux B (2003) Modeling induced polarization with classical Drude oscillators: Theory and molecular dynamics simulation algorithm. *J Chem Phys* 119(6):3025-3039.

240. Drude P ((1902) *The Theory of Optics* (Longmans, Green, New York, translation by C. Riborg Mann and Robert A. Millikan).

241. Chang T-M & Dang LX (1996) Molecular dynamics simulations of CCl_4 - H_2O liquid - liquid interface with polarizable potential models. *The Journal of Chemical Physics* 104(17):6772-6783.

242.   Langlet R, Devel M, & Lambin P (2006) Computation of the static polarizabilities of multi-wall carbon nanotubes and fullerites using a Gaussian regularized point dipole interaction model. *Carbon* 44(14):2883-2895.

243.   Karapetian K & Jordan KD (2003) *Properties of water clusters on a graphite sheet*, (Springer), pp 139-150.

244.   IKalluri RK, *et al.* (2012) Unraveling the potential and pore-size dependent capacitance of slit-shaped graphitic carbon pores in aqueous electrolytes. *Phys. Chem. Chem. Phys.* 15(7):2309-2320.

245.   Essmann U, *et al.* (1995) A Smooth Particle Mesh Ewald Method. *J Chem Phys* 103(19):8577-8593.

246.   Yeh IC & Berkowitz ML (1999) Dielectric constant of water at high electric fields: Molecular dynamics study. *J Chem Phys* 110(16):7935-7942.

247.   Phan A, Ho TA, Cole DR, & Striolo A (2012) Molecular Structure and Dynamics in Thin Water Films at Metal Oxide Surfaces: Magnesium, Aluminum, and Silicon Oxide Surfaces. *The Journal of Physical Chemistry C* 116(30):15962-15973.

248.   Lee CY, Mccammon JA, & Rossky PJ (1984) The Structure of Liquid Water at an Extended Hydrophobic Surface. *J Chem Phys* 80(9):4448-4455.

249.   Du Q, Superfine R, Freysz E, & Shen YR (1993) Vibrational spectroscopy of water at the vapor/water interface. *Phys Rev Lett* 70(15):2313-2316.